The optical and thermal properties of quantum cascade lasers

Craig Anthony Evans

submitted in accordance with the requirements for the degree of Doctor of Philosophy

Institute of Microwaves and Photonics
School of Electronic & Electrical Engineering
The University of Leeds

January 2008

The candidate confirms that the work submitted is his own and that appropriate credit has been given where reference has been made to the work of others.

For my family.

"We have a habit in writing articles published in scientific journals to make the work as finished as possible, to cover up all the tracks, to not worry about the blind alleys or describe how you had the wrong idea first, and so on. So there isn't any place to publish, in a dignified manner, what you actually did in order to get to do the work."

Richard P. Feynmann

Nobel Lecture, 1966

Acknowledgments

I would firstly, and most importantly, like to thank my supervisor Prof. Paul Harrison for his guidance and encouragement throughout my doctoral studies. I would also like to thank him for giving me the confidence during my undergraduate studies that I had the ability to carry my education on to a postgraduate level. I would also like to thank Dr. Zoran Ikonić and Dr. Dragan Indjin for their almost encyclopedic knowledge of semiconductor physics and willingness to answer my every question. I would also like to acknowledge the fellow occupiers of Room 255 over the time I been here: Dr. Vladimir Jovanović, Dr. Marco Califano, Dr. Ivana Savić, Dr. Jim McTavish, Dr. Leon Lever, Dr. Nenad Vukmirović, Alex Valavanis, Goran Isić, Pairot Moontragoon, Theerapong Puangmali, and Reeno Reeder for the scientific and moral support which made coming into University a pleasure and not a chore.

Also deserving acknowledgment are the other members of the Quantum Electronics group in the Institute of Microwaves and Photonics: Dr. Robert Kelsall, Anil Asokan and Toufik Sadi for broadening my appreciation of Quantum Electronics.

I would also like to thank the members of the quantum cascade laser experimental group in the School of Electronic and Electrical Engineering, University of Leeds namely Prof. Edmund Linfield, Prof. Giles Davies, Dr. Paul Dean, Dr. Subhashish Chakraborty, Dr. Mohammed Lachab, Suraj Khanna, and Nick Hinchcliffe for the many fruitful discussions which has led me to have a deeper understanding of the experimental side of quantum cascade lasers.

During my studies I was lucky enough to spend several weeks at the CNR INFM Regional Laboratory LIT^3 in the Dipartimento Interateneo di Fisica at the Universitá degli Studi di Bari, Italy working in the group of Prof. Gaetano Scamarcio. I would

like to thank him and his colleagues; Dr. Miriam Vitiello, Dr. Vincenzo Spagnolo, and Dr. Antonia Lops for sharing their expert knowledge on the thermal properties of quantum cascade lasers.

On a personal note, I would also like to thank Dave Evans and Clive Vallance, my friends throughout both undergraduate and postgraduate studies, with whom I have had shared many interesting conversations about all aspects of science and engineering during my time in Leeds - although most of these conversation took place when we were drunk in the student union bar! I would finally like to express my regards to my friends from SOMS for keeping me company in the Eldon pub on Friday evenings after a hard weeks work.

I would also like to acknowledge the Engineering and Physical Sciences Research Council (EPSRC) for their generous financial support of my research in Leeds.

Abstract

The optical and thermal properties of quantum cascade lasers (QCLs) are investigated through the development of comprehensive theoretical models. The optical properties of various multilayer quantum cascade laser waveguides are investigated by solving Maxwell's equations using a transfer-matrix method. The complex material refractive indices are calculated using a Drude-Lorentz model which takes into account both phonon and plasma contributions to the material properties. A Caughey-Thomas-like mobility model is used to estimate the temperature dependence of the electron mobility which is found to have a significant effect on the optical waveguide properties. The incorporation of this effect leads to better agreement with experimentally measured threshold current densities.

In order to investigate the thermal properties of QCLs, a multi-dimensional anisotropic heat diffusion model is developed which includes temperature-dependent material parameters. The model is developed using finite-difference methods in such a way that is can be solved in both the time-domain and in the steady-state. Various heat management techniques were compared in the time-domain in order to extract the heat dissipation time constants. In the steady-state, the model is used to extract the temperature dependence of the cross-plane thermal conductivity of a GaAs-based THz QCL and compare the thermal properties of THz and InP-based mid-infrared QCL optical waveguides.

In addition, fully self-consistent scattering rate equation modelling of carrier transport in short-wavelength QCLs is carried out in order to understand the internal carrier dynamics. This knowledge is then used to optimise the device design and the model predicts significant improvements in the performance of the optimised device.

Publications

Below is a list of publications from the period in which the research presented in this thesis was carried out:

Journal papers

1. C. A. Evans, V. D. Jovanović, D. Indjin, Z. Ikonić, and P. Harrison, 'Design and simulation of InGaAs/AlAsSb quantum cascade lasers for short wavelength emission', *Applied Physics Letters*, **87**, 141109 (2005).

2. C. A. Evans, V. D. Jovanović, D. Indjin, Z. Ikonić, and P. Harrison, 'Investigation of thermal effects in quantum cascade lasers', *IEEE Journal of Quantum Electronics*, **42**, pp. 859–867 (2006).

3. C. A. Evans, V. D. Jovanović, D. Indjin, Z. Ikonić, and P. Harrison, 'Investigation into thermal effects in InGaAs/AlAsSb quantum cascade lasers', *IEE Proceedings of Optoelectronics*, **99**, pp. 111-222 (2006).

4. C. A. Evans, D. Indjin, Z. Ikonić, P. Harrison, M. S. Vitiello, V. Spagnolo, and G. Scamarcio, 'Thermal modeling of terahertz quantum-cascade lasers: comparison of optical waveguides', accepted for publication in *IEEE Journal of Quantum Electronics*.

5. J. Heinrich, R. Langhans, M. S. Vitiello, G. Scamarcio, D. Indjin, C. A. Evans, Z. Ikonić, P. Harrison, S. Höfling, and A. Forchel, 'Wide wavelength tuning of GaAs/Al_xGa_{1-x}As bound-to-continuum quantum cascade lasers by Aluminium content control', accepted for publication in *Applied Physics Letters*.

Conference papers

1. P. Harrison, V. D. Jovanović, N. Vukmirović, M. Erić, I. Savić, A. Mircetic, J. McTavish, C. A. Evans, Z. Ikonić, R. W. Kelsall, V. Milanović, D. Indjin, 'A physical model and scattering dynamics engineering for intersubband lasers and photodetectors', (invited), *Conference on Optoelectronic and Microelectronic Materials and Devices – COMMAD-2004*, Brisbane, Australia, 8–10 December 2004, Proceedings (IEEE, 0-7803-8820-9/05), p. 351–355 (2005).

2. C. A. Evans, V. D. Jovanović, D. Indjin, Z. Ikonić, P. Harrison, 'Design and simulation of InGaAs/AlAsSb quantum cascade lasers for short wavelength operation', *8th International Conference on Intersubband Transitions in Quantum Wells - ITQW2005*, Cape Cod, Massachussetts, USA, 11–16 September 2005, Program and Abstracts, paper 43P.

3. C. A. Evans, V. D. Jovanović, D. Indjin, Z. Ikonić, P. Harrison, 'Design and simulation of InGaAs/AlAsSb quantum cascade lasers for short wavelength operation', *7th International Conference on Mid Infrared Optoelectronic Materials and Devices, MIOMD-VII*, Lancaster, UK, 12–14 September 2005, Abstract Book, p. 49.

4. P. Harrison, D. Indjin, V. D. Jovanović, Z. Ikonić, R.W. Kelsall, I. Savić, J. McTavish, C. A. Evans, N. Vukmirović, V. Milanović, 'Theoretical modelling and design of mid-infrared and terahertz quantum cascade lasers and quantum well infrared photodetectors', (invited), *XVI Ural Winter School on the Physics of Semiconductors*, Ekaterinburg, Russia, 28 February 2006.

5. C. A. Evans, V. D. Jovanović, D. Indjin, Z. Ikonić, P. Harrison, 'Investigation into thermal effects in InGaAs/AlAsSb quantum cascade lasers', *Semiconductor and Integrated Optoelectronics - SIOE-2006*, Cardiff, Wales, 10–12 April 2006, *IEE Proceedings of Optoelectronics*, **99**, pp. 111–222 (2006).

6. C. A. Evans, V. D. Jovanović, D. Indjin, Z. Ikonić, P. Harrison, 'Modelling of active region heating in quantum cascade lasers', *Summer School on Physics of Intersubband Semiconductor Emitters - POISE*, Cortona, Italy, 25–30 June 2006.

7. C. A. Evans, V. D. Jovanović, D. Indjin, Z. Ikonić, P. Harrison, 'Thermal effects in quantum cascade lasers', *14th International Symposium on Nanostructures: Physics and Technology*, St. Petersburg, Russia, June 2006.

8. C. A. Evans, V. D. Jovanović, D. Indjin, Z. Ikonić, P. Harrison, 'Thermal modelling of antimonide-based quantum cascade lasers', *28th International Conference on the Physics of Semiconductors - ICPS-28*, Vienna, Austria, 24–28 July 2006, *AIP Conference Proceedings*, **893**, pp. 1441–1442 (2007).

9. I. Savić, C. A. Evans, N. Vukmirović, D. Indjin, Z. Ikonić, and P. Harrison, 'Magnetic field and electro thermal modelling of quantum cascade lasers and electron transport calculations in quantum dot cascade lasers', (invited), *2nd International Workshop on Quantum Cascade Lasers*, Brindisi, Italy, 6–9 September 2006.

10. P. Harrison, D. Indjin, Z. Ikonić, I. Savić, C. A. Evans, N. Vukmirović, J. McTavish, 'On the incoherence of quantum transport in semiconductor heterostructure optoelectronic devices', (invited), *6^{th} International Conference on Low Dimensional Structures and Devices - LDSD2007*, The Caribbean Archipelago of San Andres, Colombia, 15–20 Apr 2007.

11. P. Harrison, D. Indjin, I. Savić, Z. Ikonić, C. A. Evans, N. Vukmirović, R. W. Kelsall, J. McTavish, V. Milanović, 'Transport in quantum cascade lasers', (invited, plenary), *International School and Conference on Optics and Optical Materials - ISCOM07*, Belgrade, Serbia, 3–7 Sept 2007.

12. C. A. Evans, D. Indjin, Z. Ikonić, P. Harrison, M. S. Vitiello, V. Spagnolo, and G. Scamarcio, 'Thermal modeling of THz quantum-cascade lasers', *9th International Conference on Intersubband Transitions in Quantum Wells - ITQW2007*, Ambleside, Lake District, UK, 9–14 September 2007, Program and Abstracts, paper P1.

13. P. Harrison, D. Indjin, Z. Ikonić, R. W. Kelsall, C. A. Evans and J. McTavish, 'Physical modelling of mid-infrared quantum cascade lasers', *Physics and Simulation of Optoelectronic Devices XVI - part of Photonics West*, (invited), San Jose, California, USA, 19–24 January 2008.

14. P. Harrison, D. Indjin, I. Savić, Z. Ikonić, C. A. Evans, N. Vukmirović, R. W. Kelsall, J. McTavish, V. Milanović, 'On the coherence/incoherence of electron transport in semiconductor heterostructure optoelectronic devices', (invited), *Novel in-plane semiconductor lasers VII- part of Photonics West*, (invited), San Jose, California, USA, 19–24 January 2008.

Contents

List of Abbreviations

2DEG	two-dimensional electron gas
3QW	three-quantum-well
BH	buried heterostructure
BTC	bound-to-continuum
CW	continuous-wave
DMM	diffuse mismatch model
EM	electronmagnetic
FIR	far-infrared
FWHM	full width at half maximum
IR	infrared
LO	longitudinal-optical
MBE	molecular beam epitaxy
MIR	mid-infrared
MOCVD	metal organic chemical vapour deposition
MQW	multi-quantum-well
NIR	near-infrared
QCL	quantum cascade laser
QW	quantum well
SI	semi-insulating

SL	superlattice
RT	room-temperature
TBR	thermal boundary resistance
TE	transverse electric
TM	transverse magnetic
TO	transverse-optical

List of Commonly Used Symbols

c	speed of light *in vacuo*
c_p	specific heat capacity
$\overline{D}$	displacement field
d	layer thickness
e	electronic charge ($1.60217646 \times 10^{-19}$ C)
E	electric field
E_c	conduction band offset
f	frequency
G	source power density
G_{th}	thermal conductance per unit area
g	gain coefficient
h	Planck's constant (6.626068×10^{-34} m^{2}kg/s)
H	magnetic field
i	integer counter
J	current density
$\jmath$	complex number ($\sqrt{-1}$)
k	extinction coefficient

L	cavity length
l_d	length of doped region
l_p	period length
m	mass
m_0	electron rest mass
m_*	electron effective mass
N	effective mode index
N_d	doping density
n	ordinary refractive index/subband number/integer
n'	complex refractive index
P	electrical power
$\mathcal{Q}_i$	transfer matrix of layer i
q	transfer matrix elements
R	reflectivity
R_{th}	thermal resistance
t	time
T	temperature
T_0	characteristic temperature
V	voltage
x	alloy fraction
x, y, z	cartesian coordinates
z_{ij}	dipole matrix element
α	attenuation constant
α_{fc}	free-carrier absorption loss
α_{m}	waveguide mirror loss
α_{wg}	waveguide absorption loss
β	phase propagation constant
Γ	waveguide mode confinement factor

γ	propagation constant/nonparabolicty parameter
γ_{ph}	phonon damping angular frequency
γ_{pl}	plasmon damping angular frequency
$2\gamma_{\mathrm{ul}}$	full with at half maximum of electroluminescence spectrum
ϵ	dielectric constant
ϵ_0	dielectric constant of free space
ϵ_∞	high-frequency (optical) dielectric constant
η	injection efficiency
κ	thermal conductivity/complex transverse wavevectors
λ	wavelength
λ_p	plasma wavelength
μ	permeability/electron mobility
τ	electron/transition lifetime
υ	phase velocity
Φ	waveguide figure of merit
ρ	density/resistivity
σ	conductivity
ω	angular frequency
ω_{LO}	LO-phonon angular frequency
ω_{TO}	TO-phonon angular frequency
ω_p	plasma angular frequency

Chapter 1

Introduction

1.1 Introduction to quantum cascade lasers

Quantum cascade lasers (QCLs) are semiconductor lasers that emit in the mid- to far-infrared portion of the electromagnetic (EM) spectrum and were first demonstrated by Faist *et al.* at Bell Laboratories in 1994 [1]. Unlike typical interband semiconductor lasers that emit electromagnetic radiation through the recombination of electron–hole pairs across the material bandgap (Fig. 1.1a), QCLs are unipolar (typically electrons) and laser emission is achieved through the use of intersubband transitions in a repeated stack of semiconductor superlattices, an idea first proposed in 1971 by Kazarinov and Suris [2]. Once an electron has undergone a radiative transition in one period of the superlattice, it is recycled into the next period where another radiative transition can take place (Fig. 1.1b). This means that many photons can be generated for each electron and hence QCLs have intrinsically higher powers than interband semiconductor lasers.

In the case of interband semiconductor lasers, the emission wavelength is essentially fixed by the bandgap of the particular material system used, however QCLs free us of this so called 'bandgap slavery' as the emission wavelength can be tuned over a wide range in the same material system by suitable design of the layer thicknesses in the semiconductor superlattice.

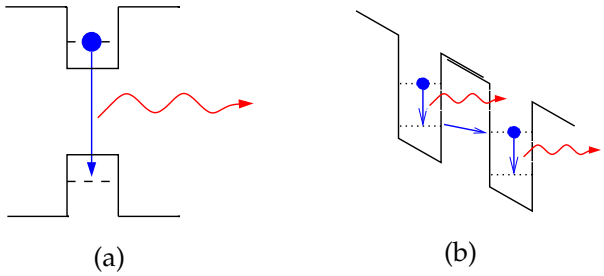

Figure 1.1: (a) Electron–hole recombination in a typical interband quantum well laser (b) Photon generation through repeated intersubband transitions.

1.2 QCL output parameters

1.2.1 Scattering rates and subband populations

As with all lasers, to achieve laser emission a population inversion must be engineered between two energy levels in the system. In QCLs, careful design of the layer thicknesses of the quantum wells (QWs) and barriers that make up the superlattice allow the electron wavefunctions and scattering rates between laser levels to be tailored in order to achieve a population inversion between two of the subbands. A population inversion is typically achieved in a QCL using a three-level system (other schemes are also used and these will be discussed later in the chapter) which is outlined in Fig. 1.2 and shows the relevant scattering processes. Each level contains a number of electrons

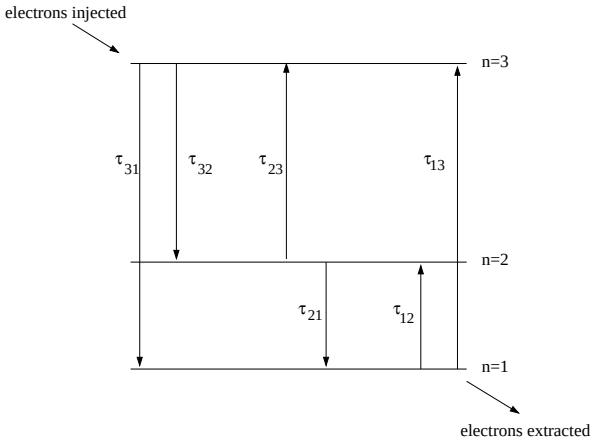

Figure 1.2: Schematic diagram showing the relevant levels and transitions in a QCL active region.

per unit area (n_i where i is the level number) which scatter between levels through various mechanisms. The main scattering mechanism in QCLs is through interactions with longitudinal-optical (LO) phonons, especially so for QCLs in the mid-infrared (MIR). In the far-infrared (FIR) region of the spectrum which is commonly known as the terahertz (THz) region then other scattering mechanisms such as electron-electron and electron-impurity interactions become important [3, 4]. The scattering rates are defined as $W_{if} = 1/\tau_{if}$, where τ_{if} is the lifetime of the transition and i and f are the initial and final subband indices.

The rate equations of the three level system in the unity injection approximation (i.e. all electrons are injected into the upper laser level) are written as

$$\frac{dn_3}{dt} = \frac{J_{in}}{e} + \frac{n_1}{\tau_{13}} + \frac{n_2}{\tau_{23}} - \frac{n_3}{\tau_{31}} - \frac{n_3}{\tau_{32}} \tag{1.1}$$

$$\frac{dn_2}{dt} = \frac{n_3}{\tau_{32}} + \frac{n_1}{\tau_{12}} - \frac{n_2}{\tau_{21}} - \frac{n_2}{\tau_{23}} \tag{1.2}$$

$$\frac{dn_1}{dt} = \frac{n_2}{\tau_{23}} + \frac{n_1}{\tau_{13}} - \frac{n_3}{\tau_{31}} - \frac{n_3}{\tau_{32}} - \frac{J_{out}}{e} \tag{1.3}$$

where J is the current density and e the fundamental charge of an electron.

In equilibrium (steady-state) $d/dt = 0$ and assuming that absorption process can be ignored (which is the case when the temperature is low) Eqn. 1.2 gives

$$\frac{n_3}{\tau_{32}} = \frac{n_2}{\tau_{21}} \tag{1.4}$$

from which it is apparent that if $\tau_{32} > \tau_{21}$ then $n_3 > n_2$ and a population inversion will exist between the $n = 3$ and $n = 2$ levels and laser action will be possible. The electron wavefunctions therefore have to be tailored such that the scattering rate W_{32} is smaller than W_{21}.

1.2.2 Current density

Also in the steady-state, $J_{in} = J_{out} = J$ and from Eqns. 1.1 and 1.3 we have

$$\frac{n_3}{\tau_{32}} + \frac{n_3}{\tau_{31}} = \frac{J}{e}. \tag{1.5}$$

The total lifetime of the upper laser level is given by

$$\frac{1}{\tau_3} = \frac{1}{\tau_{32}} + \frac{1}{\tau_{31}} \tag{1.6}$$

and hence

$$J = \frac{n_3 e}{\tau_3}. \tag{1.7}$$

1.2.3 Modal gain

The optical gain in a QW system is given by (see Appendix A for the derivation)

$$G_{32} = \left[\frac{4\pi e^2}{\epsilon_0 n}\frac{|\langle 3|z|2\rangle|^2}{2\gamma_{32} L_p \lambda}\right]\Delta n_{32} \tag{1.8}$$

where n is the refractive index, $|\langle 3|z|2\rangle|$ is the dipole matrix element between the upper and lower laser levels, $2\gamma_{32}$ is the full-width at half-maximum (FWHM), L_p is the period length and λ the free-space wavelength.

From Eqn. 1.4 and the fact that $\tau_2 = \tau_{21}$, under the auspices of the unity injection approximation, we can write the population inversion as

$$\Delta n_{32} = n_3 - n_2 = n_3\left(1 - \frac{\tau_{21}}{\tau_{32}}\right). \tag{1.9}$$

Re-arranging Eqn. 1.7 in terms of n_3 and inserting into the above equation we find

$$\Delta n_{32} = \frac{\tau_3}{q}\left(1 - \frac{\tau_2}{\tau_{32}}\right) J. \tag{1.10}$$

Inserting this into Eqn. 1.8 we arrive at the well-known equation for gain in a QCL

$$G = \left[\frac{4\pi e}{\epsilon_0 n}\frac{(z_{32})^2}{2\gamma_{32} L_p \lambda}\right]\tau_3\left(1 - \frac{\tau_2}{\tau_{32}}\right) J = gJ \tag{1.11}$$

where z_{32} is short-hand for the bra-ket notation of the dipole matrix element and g is defined as the gain coefficient

$$g = \left[\frac{4\pi e}{\epsilon_0 n}\frac{(z_{32})^2}{2\gamma_{32} L_p \lambda}\right]\tau_3\left(1 - \frac{\tau_2}{\tau_{32}}\right). \tag{1.12}$$

If we now move away from the unity injection approximation and recast the above equations allowing a fraction $(1-\eta)$ of the current to be injected directly into the lower laser level we find that the rate equations of the laser levels are now given by

$$\frac{dn_3}{dt} = \frac{\eta J_{in}}{e} + \frac{n_1}{\tau_{13}} + \frac{n_2}{\tau_{23}} - \frac{n_3}{\tau_{31}} - \frac{n_3}{\tau_{32}} \tag{1.13}$$

$$\frac{dn_2}{dt} = \frac{(1-\eta) J_{in}}{e} + \frac{n_3}{\tau_{32}} + \frac{n_1}{\tau_{12}} - \frac{n_2}{\tau_{21}} - \frac{n_2}{\tau_{23}}. \tag{1.14}$$

From these equations in the steady-state we obtain

$$n_3 = \frac{\eta\tau_3 J}{e} \tag{1.15}$$

and

$$n_2 = \frac{n_3\tau_2}{\tau_{32}} + \frac{(1-\eta)\tau_2 J}{e}. \tag{1.16}$$

We then find the population inversion is given by

$$\Delta n_{32} = \frac{J}{e}\left(\eta\tau_3 - \tau_2\left[1-\eta\left(1-\frac{\tau_3}{\tau_{32}}\right)\right]\right) \tag{1.17}$$

and the gain coefficient is modified to

$$g = \frac{4\pi e z_{32}^2}{\epsilon_0 N l_p \lambda(2\gamma_{32})}\left(\eta\tau_3 - \tau_2\left[1-\eta\left(1-\frac{\tau_3}{\tau_{32}}\right)\right]\right). \tag{1.18}$$

The modal gain is proportional to the fraction of the optical field that overlaps with the gain media and is given by

$$G_M(J) = g\Gamma J \tag{1.19}$$

where Γ is the overlap of the optical mode with the active region.

To achieve a large amount of modal gain, we require a large upper laser level lifetime (τ_3) and a short lower laser level lifetime (τ_2) together with a high injection efficiency η. A small FWHM and short period length also help to attain large values of gain, and it is easier to achieve at shorter wavelengths. A large fraction of the optical mode must also overlap with the gain media. The above equations suggest that a large dipole matrix element is required, and this is true in some sense, although τ_{32} is inversely proportional to the matrix element. Therefore a larger z_{32} reduces the population inversion and so a trade-off is required.

1.2.4 Threshold current density

A QCL will begin to lase when the modal gain is equal to the round-trip cavity losses i.e. when

$$G_M = \alpha_{\mathrm{M}} + \alpha_{\mathrm{W}} \tag{1.20}$$

where α_{M} is the mirror loss (loss from the ends of the laser cavity) and α_{W} is the waveguide loss (primarily due to free-carrier absorption). The above equation can be

re-written as

$$g\Gamma J = \alpha_{\mathrm{M}} + \alpha_{\mathrm{W}} \tag{1.21}$$

and hence we can estimate the current that is required to reach the lasing threshold to be

$$J_{\mathrm{th}} = \frac{\alpha_{\mathrm{M}} + \alpha_{\mathrm{W}}}{g\Gamma}. \tag{1.22}$$

It will be shown later in Chapter 3 why it is beneficial to reduce J_{th} as much as possible.

1.3 QCL device designs

This section describes the various design schemes of QCLs and how each one attains enough gain for lasing to take place.

1.3.1 Three quantum well active region

In the first QCL [1] and subsequent designs, a population inversion was engineered utilising a three quantum well (3QW) active region, with each QW contributing one subband. Fig. 1.3 shows a schematic conduction band diagram of a $\lambda \sim 8.4\mu$m QCL with a 3QW active region and a diagonal transition. In order to minimise τ_2, the energy

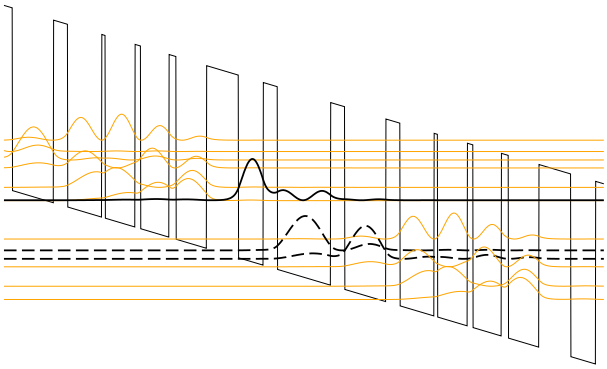

Figure 1.3: Schematic conduction band diagram of a 3QW diagonal transition active region QCL at a bias of 60 kV/cm emitting at $\lambda \sim 8.4\mu$m. The upper laser level is shown in bold and the lower laser level and ground levels are shown as a bold dashed lines.

gap between the $n = 2$ and $n = 1$ (ground level) states is designed such that they are separated in energy by the LO phonon energy of the quantum well material (~ 36 meV

in GaAs) and hence resonant LO-phonon scattering can then efficiently depopulate the lower laser level. In order to ensure τ_{32} is greater than τ_2, a diagonal transition is used. This means that the $n = 3$ wavefunction is mostly confined within the first quantum well of the active region, reducing the overlap between the laser levels and hence increasing τ_{32} but also reducing z_{32}.

In this type of design, a large value of η is obtained by the penetration of the $n = 3$ wavefunction into the injection barrier and so electrons are injected from the injector states into the $n = 3$ state through resonant tunnelling. Injection of electrons from the injector directly into the $n = 2$ state (i.e. non-unity injection) is minimised by careful design of the injection barrier thickness. If it is too thin, the selectivity of the injection from the injector is reduced and current channels are opened up directly into the $n = 2$ state. Care must also be made to ensure that the injection barrier is not too thick or else η will be reduced. It is also important to choose the right thickness of extraction barrier. If the barrier is too thick, the escape time of the electrons from the $n = 1$ is increased, which creates an electron 'bottleneck' and reduces the performance.

There is another class of 3QW active region utilising a 'vertical transition' . In this scheme, the $n = 3$ state is more spread out over the 3QW active region, increasing the overlap between the laser levels (z_{32}) but also reducing the injection efficiency i.e. η, as well as decreasing the value of τ_{32}. Fig. 1.4 shows a schematic conduction band diagram of a $\lambda \sim 5\mu$m QCL with a 3QW active region and a vertical transition.

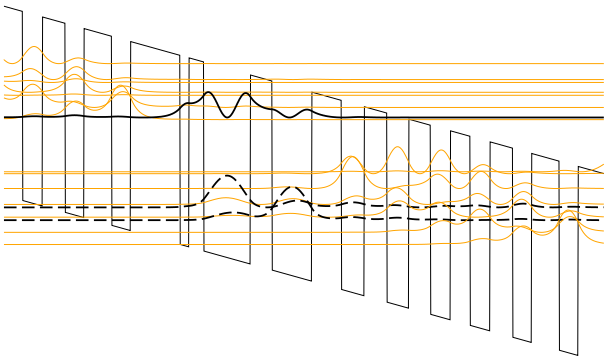

Figure 1.4: Schematic conduction band diagram of a 3QW vertical transition active region QCL at a bias of 76 kV/cm emitting at $\lambda \sim 5\mu$m

1.3.2 Double LO-phonon resonance

It is possible to improve the performance of 3QW QCLs by adding a further quantum well to the active region. The lasing transition takes place between the $n = 4$ and $n = 3$ states with the $n = 2$ state being one LO-phonon energy below the $n = 3$ state as with the 3QW case. The extra subband ($n = 1$) added to the active region by the additional well is designed such that it is one LO-phonon energy below the $n = 2$ state. This active region configuration maintains the good injection efficiency at the same time as reducing the lifetime of the lower laser level, τ_3 leading to a concomitant increase in the population inversion. A schematic conduction band diagram of the first room temperature continuous wave (cw) QCL by Beck *et al.* [5] which utilised a double LO-phonon depopulation scheme is shown in Fig. 1.5. The addition of the extra subband

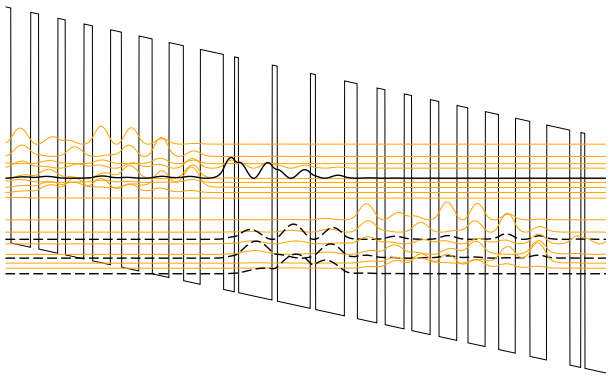

Figure 1.5: Schematic conduction band diagram of a double LO-phonon resonance QCL at a bias of 28 kV/cm emitting at $\lambda \sim 9.1\mu$m. The upper laser level is shown in bold and the lower laser level and ground levels are shown as a bold dashed lines and are designed to be separated by the LO-phonon energy

also increases the energy gap between the highly populated injector miniband and the lower laser level. This reduces an effect known as 'thermal backfilling' of the lower laser level and allows the QCL to operate at higher temperatures. At high temperatures in a standard 3QW active region, electrons in the injector states can have enough thermal energy to be activated back into the lower laser level reducing the population inversion and limiting the device performance.

1.3.3 Interminiband/Chirped superlattice

QCLs have also been reported in which the radiative transition is not intersubband, but rather an interminiband one in a superlattice active region. In this QCL design scheme, there are only two main states involved in the laser transition; the upper laser level is the lowest state in the upper miniband and the lower laser level is the uppermost state of the lower miniband. This breed of QCL has an intrinsic population inversion due to the very fast intraminiband scattering between the miniband states which efficiently depopulates the lower laser level (i.e. a small τ_2 following the notation in Fig. 1.2). This type of scattering is much quicker than the interminiband scattering between the minibands themselves and also helps to avoid any electron bottleneck problems that are found with 3QW active regions (i.e. the escape time of electrons from the active region is negligible). However, the injection into the upper laser level (η) is not as great as in 3QW active regions but both the laser level wavefunctions are localised across the entire active region leading to a larger dipole matrix element.

Due to the wide energy minibands in the SLs, these QCLs have a higher current carrying capability compared to QCLs with 3QW active regions which leads to higher output powers. In the first interminiband QCL [6], the active region superlattice had to be doped to compensate for the applied bias and so the minibands remained flat. This led to high optical losses, broadened emission and increased threshold currents compared to 3QW QCLs preventing room temperature emission being achieved. In the next generation of interminiband QCLs, only the injector regions were doped [7] which lead to room temperature emission. In this design, the field generated by the doped injector region exactly compensated the applied field and by suitable design of the layer thicknesses, the minibands in the active and injector regions could be aligned ensuring efficient injection into the upper state of the lasing transition. However, the best performance was obtained by removing the dopants altogether and 'chirping' the superlattice. By changing the period of the superlattice, the actual electronic potential is modified and under the applied bias, quasi-flat minibands can be obtained without the need for dopants [8]. This type of QCL design is known as a 'chirped superlattice'

and led to record room temperature peak powers and record low threshold current densities for QCLs at the time. A schematic conduction band diagram of the first terahertz (THz) QCL emitting at 4.4 THz ($\lambda \sim 67\mu$m) based upon a chirped superlattice design [9] is shown in Fig. 1.6.

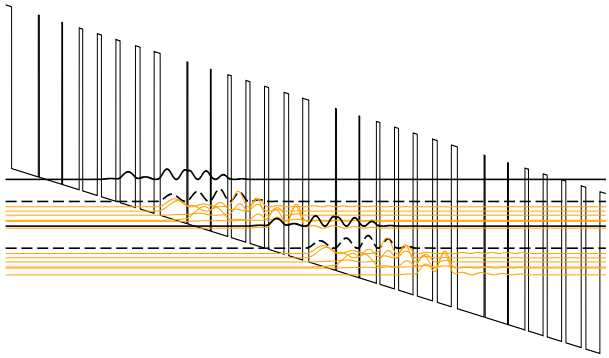

Figure 1.6: Schematic conduction band diagram of two periods of the first THz QCL based upon a chirped superlattice design. The upper laser levels are shown in bold and the lower laser levels are shown as bold dashed lines.

1.3.4 Bound-to-continuum

In 2001, a new class of QCLs combining the advantages of the 3QW and chirped superlattice designs was developed by Faist *et al.* [10]. The design takes advantage of the good injection efficiency in 3QW active regions achieved through resonant tunnelling and the good extraction efficiency of the chirped superlattice design (i.e. small τ_2). The lasing transition takes place between a bound state localised close to the injection barrier and a miniband; hence the name 'bound-to-continuum'. A schematic conduction band diagram of the first bound-to-continuum QCL emitting at $\lambda \sim 9.1\mu$m is shown in Fig. 1.7. The design is based upon a chirped SL with the active region spanning the whole period. The upper laser level is created in the minigap between the minibands by a thin well next to the injection barrier. Bound-to-continuum QCLS have proven particularly successful in the both the mid-infrared (MIR) and THz frequency range, with cw operation above room temperature and pulsed mode operation up to 425 K reported in the MIR [11] and cw emission up to 70 K in the THz [12].

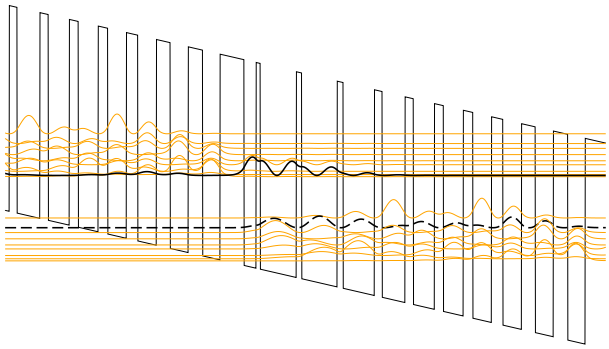

Figure 1.7: Schematic conduction band diagram of the first bound-to-continuum QCL under a bias of 35 kV/cm. The bound state (upper laser level) is shown in bold and the continuum state (lower laser level) is shown as a bold dashed line.

1.3.5 Direct LO-phonon depopulation

Another successful active region design in the THz frequency range is based on direct LO-phonon depopulation of the lower laser level, directly into the upper laser level of the next period. The QCL period consists of a two well active region and a two well injector. Fig. 1.8 shows a schematic conduction band diagram of a 3.4 THz direct LO-phonon depopulation QCL designed by Willams *et al* [13]. The lasing transition takes

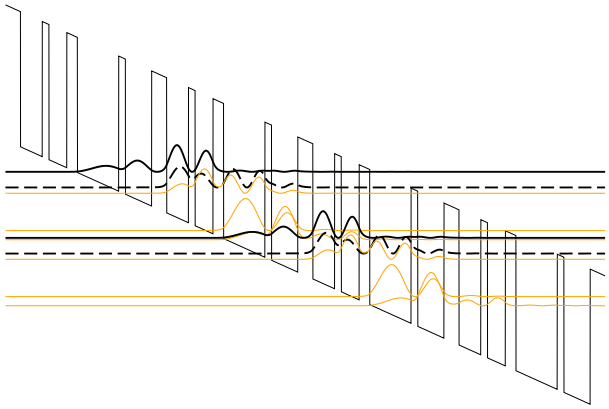

Figure 1.8: Schematic conduction band diagram of 3.4 THz QCL utilising direct LO-phonon depopulation under a bias of 12.2 kV/cm. The upper laser level is shown in bold and the lower laser level is shown as a bold dashed line

place between the laser levels denoted in the figure and at the design bias, the lower laser level is approximately one LO-phonon energy above the injector states which are

aligned with the upper laser level of the next period. Therefore resonant LO-phonon depopulation of the lower laser level takes place and injects the electrons directly into the upper laser level of the next period. A significant advantage of this design is the narrow period of the active region L_p, which as well as resulting in a larger gain coefficient g, also means that the overlap of the active region with the optical mode in the waveguide is increased. This direct-LO depopulation scheme has led to the THz QCLs operating at high temperatures, emitting at approximately 3.0 THz up to 164 K in pulsed mode and 117 K in cw [14].

1.3.6 One-well injector

A further THz active region design which is similar to the direct LO-phonon depopulation design is the one-well injector scheme. In this design, there is a three quantum well active region and a single injector well. A schematic conduction band diagram of a 1.9 THz QCL with a one-well injector [15] is shown in Fig. 1.9. The radiative

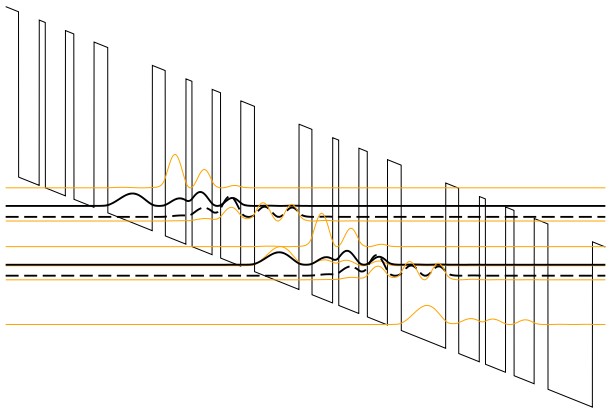

Figure 1.9: Schematic conduction band diagram of 1.9 THz QCL with a one-well injector under a bias of 8.4 kV/cm. The upper laser level is shown in bold and the lower laser level is shown as a bold dashed line.

transition takes place between the laser levels denoted in the figure. The electrons are extracted from the lower level into the single injector subband by resonant LO-phonon scattering from which they are injected into the upper laser level of the next period by sequential tunnelling. Since most of the carriers reside in the injector region which has only one subband, the lack of additional injector states prevents reabsorption of the

THz radiation and significantly reduces the waveguide loss which is a limiting factor for long wavelength emission. This fact, coupled with the short QCL period, enabled the one-well injector QCL denoted in Fig. 1.9 to achieve the longest wavelength QCL emission ($\lambda \sim 161\mu$m) without the assistance of a magnetic field [15].

1.4 QCL material systems

Due to the fact that the radiative emission process in QCLs arises from intersubband transitions, the quantum cascade principle should be equally applicable to any semiconductor heterostructure. This sections details the various material systems that have been used to produce QCLs.

1.4.1 InP-based

The first reported QCL was fabricated in the $In_{0.53}Ga_{0.47}As/In_{0.52}Al_{0.48}As$ material system [1]. This particular material composition is lattice-matched to InP, which is used as the device substrate. The band offset of this particular composition is $\Delta E_c = 0.52$ eV. There are several advantages to this material system; namely the availability of the InP substrate, the fact that the binary InP has a higher thermal conductivity than ternary semiconductors and the low refractive index of InP. The fact that InP has a low refractive index means that the substrate acts as a natural waveguide and also opens up the possibility of lateral regrowth of InP upper cladding layers which results in a large overlap of the active region with the optical mode and low losses. The high thermal conductivity allows heat to be efficiently extracted from the active region and increases the operating temperatures of the QCLs. The inherent advantages of the InP-based material system means these QCLs have achieved high levels of performance in the MIR, including room temperature cw emission [5]. The performance level of the InP-based QCLs can be further increased by utilising strain-balanced active regions. In these QCLs, the composition of the material system is altered to introduce strain into the system which increases the conduction band offset. An increased conduction band offset is beneficial for high temperature operation as it reduces electron leakage (also known as thermionic emission) from the upper laser level into higher

energy continuum-like states and helps to conserve a population inversion at raised temperatures. An increased conduction band offset also allows higher photon energies and the use of strain-balanced active regions has led to the short wavelength emission at $\lambda \sim 3.05\mu$m [16]. At the present time, GaAs-based QCLs have dominated the THz frequency range (see next section) although there has been one report of an InP-based THz QCL [17] which operated up to 45 K.

In 2001, an InP-based QCL was reported in which the $In_{0.52}Al_{0.48}As$ barriers were replaced by $AlAs_{0.56}Sb_{0.44}$ [18]. This heterostructure is lattice matched to InP and increases the conduction band offset to 1.6 eV. This high value of conduction band offset makes this material system inherently less sensitive to temperature and suitable for short wavelength emission. To date, InGaAs/AlAsSb QCLs have been reported working in pulsed mode above room temperature in the wavelength range $\lambda \sim 3.7$–4.5μm [19, 20], with emission at wavelengths as low as $\lambda \sim 3.05\mu$m reported [21].

This material system is the focus of Chapter 6.

1.4.2 GaAs-based

In 1998, the first GaAs-based QCL was reported [22] with a 3QW active region emitting in the MIR. The $GaAs/Al_{0.33}Ga_{0.67}As$ material system has a conduction band offset of 295 meV and this relatively small value led to a maximum operating temperature of 140 K. The GaAs-based material system has several disadvantages compared to InP-based material systems. Together with the smaller conduction band offset which increases the electron leakage, the GaAs substrate has a larger refractive index than the QCL active region and so cannot be used as a waveguide cladding layer as in InP-based QCLs. This means specially designed plasmon-enhanced waveguides must be used [23]. Another disadvantage is the fact that GaAs has a lower thermal conductivity than InP and so GaAs-based lasers have less ability to dissipate heat away from the active region. Despite these disadvantages, room temperature pulsed mode emission has been achieved in MIR GaAs-based 3QW QCLs with $Al_{0.45}Ga_{0.55}As$ barriers. The larger Al content increases the band offset to 390 meV and hence reduces the electron leakage at higher temperatures [24]. To further increase the conduction band offset,

AlAs barriers have also been used. This increases the band offset to ~ 1 eV, although it also introduces indirect states in the barrier material as the conduction band minimum is at the X point of the Brillouin zone and the resulting intervalley scattering is thought to be detrimental to device performance. Even so, QCLs with AlAs barriers have been realised emitting at 11.4 and 11.8 μm [25, 26]. These lasers exhibit better thermal properties than GaAs-based QCLs with AlGaAs barriers, in particular threshold currents which are less sensitive to temperature [25].

Although it is very unlikely that GaAs-based QCLs will ever match the performance levels InP-based QCLs in the MIR, GaAs-based QCLs have proven extremely successful in the THz frequency range. The first THz QCL was in the GaAs/$Al_{0.15}Ga_{0.85}$As material system [9] and since then THz QCLs in this material system have reported in the frequency range 1.2 – 4.9 THz [27, 28] (and down to 830 GHz with the assistance of a magnetic field [29]).

1.4.3 InAs/AlSb QCLs

Another material system that has attracted large amounts of interest for the development of short wavelength QCLs is InAs/AlSb grown on InAs substrates. This material system has a very large conduction band offset of 2.1 eV which lends itself to short wavelength emission. However there are some difficulties with this material system. The large band offset neccesitates the use of very thin barriers but the lack of a common atom at the interfaces makes growth difficult. This material system is also not as well studied as InP- and GaAs-based technologies and so there is some uncertainty about the material parameters which makes the design and modelling more difficult. Early devices suffered from very large threshold current densities and the lack of a suitable waveguide. Recently, the development of an optical waveguide utilising InAs/AlSb spacer layers together with InAs plasmon layers has led to the realisation of $\lambda \sim 3.3\mu$m devices working up to 400 K in pulsed mode [30] and devices operating at wavelengths as short as 2.75μm at 80 K [31] (the current quantum cascade laser 'world record' shortest wavelength). The potential for even shorter wavelength emission has also been confirmed by the observation of room temperature intersubband

emission at $\lambda \sim 2.5\mu$m [32].

1.5 Fabrication

1.5.1 Molecular beam expitaxy

The main growth technique of QCLs is molecular beam epitaxy (MBE) which was developed in the early 1970s [33] and can produce high-quality layers with abrupt interfaces and tight control of the layer thickness, doping level and concentration. In order to obtain high-purity layers, the whole process takes place in an ultra-high vacuum environment. In solid source MBE, ultra high purity elements (such as gallium, arsenic and aluminium) are heated in cells separated from the main growth chamber until they sublime. Inside the main growth chamber, the target substrate wafer is heated and rotated. Opening the shutters between the cells and growth chamber allows the gaseous elements to condense onto the substrate, where, in the case of gallium and arsenic, they will react to form GaAs [34].

An important point is the slow growth rates which allow the films to grow epitaxially and follow the crystal structure of the substrate. Since the shutters can be controlled in a fraction of a second, the slow growth rates mean that atomically abrupt interfaces between layers of different materials (e.g. GaAs and AlGaAs) can be produced. This fact is what allows the complex alternating layered structure of QCLs to be grown using MBE.

1.5.2 Metal-organic vapour phase epitaxy

An alternative growth technique is metal-organic vapour phase epitaxy (MOVPE) which is also know as metal-organic chemical vapour deposition (MOCVD) [35]. Similarly to MBE, it allows the epitaxial growth of high-quality layers with precise control of the thickness and composition. In contrast to MBE, which is a physical deposition method, in MOVPE layers are deposited through chemical reactions on the surface of the heated substrate. This does not take place in a vacuum, but in a gaseous environment at moderate pressures [34].

1.6 Potential applications of QCLs

The fact that QCLs emit from the near- to the far-infrared makes them ideal candidates as radiation sources in a wealth of applications in this wavelength range. The majority of chemical compounds have fundamental vibrational modes in the wavelength range from 3 to 15 μm. This means the detection of various chemicals such as CO_2, CH_4, NH_3, N_2O, SO_2 and HNO_3 is possible which has many important applications in the detection of pollutants, the monitoring of industrial processes, chemical forensics, the detection of chemical and biological warfare agents and non-invasive medical diagnostics. There are also two 'atmospheric windows' between 3 and 5 μm and 8 and 12 μm offering the possibility of remote sensing and detection as well as wireless optical communication links. There is also a possibility that in the future, QCLs may be developed which are compatible with the optical fibre wavelengths 1.3 and 1.55 μm.

There are a wealth of possible applications in the THz region. Before the advent of THz QCLs, there was a distinct lack of compact, low-consumption, solid-state THz sources and led to a 'terahertz gap' in the EM spectrum, between microwave and millimetre wave technologies and optical systems. THz applications are based around imaging which have the possibility of replacing harmful X-rays with harmless T-rays. These THz imaging applications include medical imaging (particularly in the field of oncology), dental imaging (i.e. detection of cavities and tooth decay) and security (i.e. airport scanners). For more details, see for example [36].

1.7 Thesis structure

Following this introductory chapter which has introduced the fundamental concepts of QCLs to give the reader a solid platform from which to understand the remainder of the thesis, Chapter 2 focusses on the types of optical waveguides that are used in QCLs. After outlining the development of a one-dimensional optical waveguide solver based on a transfer matrix technique, the optical properties of semiconductors are discussed before analysing the various optical waveguiding schemes that are used in the MIR and THz.

Chapter 3 explains the importance of the device temperature and how it affects performance. The thermal properties of semiconductors are discussed and then the development of a multi-dimensional thermal model of heat diffusion in QCLs based on finite-differences is outlined. This thermal model is then used in Chapter 4 to study the transient thermal behaviour of InP-based MIR QCLs, and in Chapter 5, the model is used to investigate the thermal properties of both MIR and THz QCLs under cw operation. In Chapter 6, the self-consistent scattering rate model developed in Leeds is outlined and adapted in order to investigate the carrier dynamics in short-wavelength InGaAs/AlAsSb QCLs.

Finally, conclusions are drawn and possible avenues for further work are discussed in Chapter 7.

References

[1] J. Faist, F. Capasso, D. L. Sivco, C. Sirtori, A. L. Hutchinson, and A. Y. Cho, "Quantum cascade laser," *Science*, vol. 264, p. 553, 1994.

[2] R. F. Kazarinov and R. A. Suris, "Possibility of the amplification of electromagnetic waves in a semiconductor with a superlattice," *Soviet Physics - Semiconductors*, vol. 5, pp. 707–709, 1971.

[3] H. Callebaut, S. Kumar, B. S. Williams, Q. Hu, and J. L. Reno, "Importance of electron-impurity scattering for electron transport in terahertz quantum-cascade lasers," *Appl. Phys. Lett.*, vol. 84, p. 645, 2004.

[4] D. Indjin, P. Harrison, R. W. Kelsall, and Z. Ikonić, "Self-consistent scattering model of carrier dynamics in GaAs-AlGaAs terahertz quantum-cascade lasers," *IEEE Photon. Technol. Lett.*, vol. 15, pp. 15–17, 2003.

[5] M. Beck, D. Hofstetter, T. Aellen, J. Faist, U. Oesterle, M. Ilegems, E. Gini, and H. Melchior, "Continuous wave operation of a mid-infrared semiconductor laser at room temperature," *Science*, vol. 295, p. 301, 2002.

[6] G. Scamarcio, F. Capasso, C. Sirtori, J. Faist, A. L. Hutchinson, D. L. Sivco, and A. Y. Cho, "High-power infrared (8-micrometer wavelength) superlattice lasers," *Science*, vol. 276, p. 773, 1997.

[7] A. Tredicucci, F. Capasso, C. Gmachl, D. L. Sivco, A. L. Hutchinson, A. Y. Cho, J. Faist, and G. Scamarcio, "High-power inter-miniband lasing in intrinsic superlattices," *Appl. Phys. Lett.*, vol. 72, no. 19, p. 2388, 1998.

[8] A. Tredicucci, F. Capasso, C. Gmachl, D. L. Sivco, A. L. Hutchinson, and A. Y.

Cho, "High performance interminiband quantum cascade lasers with graded superlattices," *Appl. Phys. Lett.*, vol. 73, no. 15, p. 2101, 1998.

[9] R. Köhler, A. Tredicucci, F. Beltram, H. E. Beere, E. H. Linfield, A. G. Davies, D. A. Ritchie, R. C. Iotti, and F. Rossi, "Terahertz semiconductor heterostructure laser," *Nature*, vol. 417, no. 156, pp. 156–159, 2002.

[10] J. Faist, M. Beck, T. Aellen, and E. Gini, "Quantum-cascade lasers based on a bound-to-continuum transition," *Appl. Phys. Lett.*, vol. 78, no. 2, p. 147, 2001.

[11] J. Faist, D. Hofstetter, M. Beck, T. Aellen, M. Rochat, and S. Blaser, "Bound-to-continuum and two-phonon resonance quantum cascade lasers for high duty cycle, high-temperature operation," *IEEE J. Quantum. Electron*, vol. 38, no. 6, pp. 533–546, 2002.

[12] S. Barbieri, J. Alton, H. E. Beere, J. Fowler, E. H. Linfield, and D. A. Ritchie, "2.9 THz quantum cascade lasers operating up to 70 K in continuous wave," *Appl. Phys. Lett.*, vol. 85, no. 10, p. 1674, 2004.

[13] B. S. Williams, H. Callebaut, S. Kumar, Q. Hu, and J. L. Reno, "3.4-THz quantum cascade laser based on longitudinal-optical-phonon scattering for depopulation," *Appl. Phys. Lett.*, vol. 82, no. 7, p. 1015, 2003.

[14] B. S. Williams, S. Kumar, Q. Hu, and J. L. Reno, "Operation of terahertz quantum-cascade lasers at 164 K in pulsed mode and at 117 K in continuous-wave mode," *Opt. Express*, vol. 13, no. 9, p. 3331, 2005.

[15] S. Kumar, B. S. Williams, Q. Hu, and J. L. Reno, "1.9 THz quantum-cascade lasers with one-well injector," *Appl. Phys. Lett.*, vol. 88, no. 121123, pp. 1–3, 2006.

[16] M. P. Semtsiv, M. Wienold, S. Dressler, and W. T. Masselink, "Short-wavelength ($\lambda \approx 3.05\mu$m) InP-based strain-compensated quantum-cascade laser," *Appl. Phys. Lett.*, vol. 90, no. 051111, pp. 1–3, 2007.

[17] L. Ajili, G. Scalari, N. Hoyler, M. Giovannini, and J. Faist, "InGaAs–AlInAs/InP terahertz quantum cascade laser," *Appl. Phys. Lett.*, vol. 87, no. 141107, pp. 1–3, 2005.

[18] D. G. Revin, L. R. Wilson, E. A. Zibnik, R. P. Green, and J. W. Cockburn, "InGaAs/AlAsSb quantum cascade lasers," *Appl. Phys. Lett.*, vol. 85, no. 18, p. 3992, 2004.

[19] Q. Yang, C. Manz, W. Bronner, K. Köhler, and J. Wagner, "Room-temperature short-wavelength ($\lambda \sim 3.7$–3.9μm) GaInAs-AlAsSb quantum cascade lasers," *Appl. Phys. Lett.*, vol. 88, no. 121127, 2006.

[20] Q. Yang, C. Manz, W. Bronner, C. Mann, L. Kirste, K. Köhler, and J. Wagner, "GaInAs/ AlAsSb quantum-cascade lasers operating up to 400 K," *Appl. Phys. Lett.*, vol. 86, no. 131107, 2005.

[21] D. G. Revin, J. W. Cockburn, M. J. Steer, R. J. Airey, M. Hopkinson, A. B. Krysa, L. R. Wilson, and S. Menzel, "InGaAs/AlAsSb/InP quantum cascade lasers operating at wavelengths close to 3 μm," *Appl. Phys. Lett.*, vol. 90, no. 021108, pp. 1–3, 2007.

[22] C. Sirtori, P. Kruck, S. Barbieri, P. Collot, J. Nagle, M. Beck, J. Faist, and U. Oesterle, "GaAs/$Al_xGa_{1-x}As$ quantum cascade lasers," *Appl. Phys. Lett.*, 1998.

[23] C. Sirtori, P. Kruck, S. Barbieri, H. Page, and J. Nagle, "Low-loss Al-free waveguides for unipolar semiconductor lasers," *Appl. Phys. Lett.*, vol. 75, no. 25, pp. 3911–3913, 1999.

[24] H. Page, C. Becker, A. Robertson, G. Glastre, V. Ortiz, and C. Sirtori, "300 K operation of a GaAs-based quantum-cascade laser at $\lambda \approx 9\mu$m," *Appl. Phys. Lett.*, vol. 78, no. 22, p. 3529, 2001.

[25] C. Becker, C. Sirtori, H. Page, G. Glastre, V. Ortiz, X. Marcadet, M. Stellmacher, and J. Nagle, "AlAs/GaAs quantum cascade lasers based on large direct conduction band discontinuity," *Appl. Phys. Lett.*, vol. 77, no. 4, p. 463, 2000.

[26] W. Schrenk, N. Finger, S. Gianordoli, E. Gornik, and G. Strasser, "Continuous wave operation of distributed feedback AlAs/GaAs superlattice quantum cascade lasers," *Appl. Phys. Lett.*, vol. 77, no. 21, p. 3328, 2000.

[27] C. Walther, M. Fischer, G. Scalari, R. Terazzi, N. Hoyler, and J. Faist, "Quantum cascade lasers operating from 1.2 to 1.6 THz," *Appl. Phys. Lett.*, vol. 91, no. 131122, pp. 1–3, 2007.

[28] A. W. M. Lee, Q. Qin, S. Kumar, B. S. Williams, Q. Hu, and J. L. Reno, "Real-time terahertz imaging over a standoff distance (>25 meters)," *Appl. Phys. Lett.*, vol. 89, no. 141125, pp. 1–3, 2006.

[29] G. Scalari, C. Walther, J. Faist, H. E. Beere, and D. A. Ritchie, "Laser emission at 830 and 960 GHz from quantum cascade structures." presented at ITQW2007, Ambleside, U.K., Sept 10–14, 2007.

[30] J. Devenson, O. Cathabard, R. Teissier, and A. N. Baranov, "High temperature operation of $\lambda \approx 3.3\mu$m quantum cascade lasers," *Appl. Phys. Lett.*, vol. 91, no. 251102, pp. 1–3, 2007.

[31] J. Devenson, O. Cathabard, R. Teissier, and A. N. Baranov, "InAs/AlSb quantum cascade lasers emitting at 2.75– 2.97 μm," *Appl. Phys. Lett.*, vol. 91, no. 251102, pp. 1–3, 2007.

[32] D. Barate, R. Teissier, Y. Wang, and A. N. Baranov, "Short wavelength intersubband emission from InAs/AlSb quantum cascade structures," *Appl. Phys. Lett.*, vol. 87, no. 051103, 2005.

[33] A. Y. Cho, "Film deposition by molecular beam techniques," *J. Vac. Sci. Tech.*, vol. 8, pp. S31–S38, 1971.

[34] J. H. Davies, *The physics of low-dimensional semiconductors: an introduction*. Cambridge, 1998.

[35] G. B. Stringfellow, *Organometallic Vapor-Phase Epitaxy: Theory and Practice*. Academic Press, second ed., 1999.

[36] R. E. Miles, P. Harrison, and D. Lippens, eds., *Terahertz sources and systems Vol. 27*. NATO Science Series II, Kluwer, Dordrecht, 2001.

Chapter 2

Quantum cascade laser optical waveguide analysis

2.1 Introduction to optical waveguides

The optical waveguide is an integral aspect of a semiconductor laser and serves the purpose of confining as much of the optical mode as possible inside the active region in order to increase the photon density and promote stimulated emission. In typical interband semiconductor laser diodes which emit from the blue to near-infrared areas of the EM spectrum, optical confinement is provided through standard dielectric slab waveguides with refractive index mismatches and the light is contained in the layer with the highest refractive index through total internal reflection (TIR). In longer wavelength QCLs this approach is not viable since the large thicknesses of waveguide layers that are required in order to confine a sufficient amount of the optical mode inside the active region are not readily achievable through current growth techniques. Therefore several QCL waveguiding schemes have been developed for use at different wavelengths.

The optical waveguide described above provides optical confinement in the growth direction and typically lateral confinement is provided through the use of ridge structures. As well as providing optical confinement, a ridge structure also confines the electrical current. Although in principle a planarised structure could be used in collaboration with a gain-guiding approach to confine the optical mode, this is not

favoured due to the strong anisotropy of the active region electrical conductivity [1]. Typically the facets of the laser cavity are formed by simply cleaving the semiconductor crystal and, as in all lasers, (Fresnel) reflections between the facets allows the radiation to make multiple passes of the gain medium until it is amplified enough to balance the waveguide losses. When this condition is satisfied, laser action can commence.

To achieve laser action, the modal gain G_M must therefore be larger than the total losses and from Eqn. 1.19 it can be seen that G_M can be increased by having a large overlap factor Γ. Any optical waveguide must therefore confine as much of the optical mode inside the gain medium as possible while minimising the losses. As already shown in Eqn. 1.22, the laser threshold current density can be calculated using

$$J_{\text{th}} = \frac{\alpha_{\text{M}} + \alpha_{\text{W}}}{g\Gamma}. \tag{2.1}$$

By inspecting the above equation it is also apparent that a 'good' waveguide design (i.e. large Γ, small α) will also bring about a smaller threshold current density for a given gain coefficient g. This is not only useful from a power consumption standpoint, but as will be discussed in further detail in Chapter 3, it will also cause a lowering of the active region temperature and therefore an improvement in device performance.

This chapter first outlines the development of a QCL optical waveguide solver. Fig. 2.1 shows a typical cross section of a QCL ridge waveguide. It is apparent from the

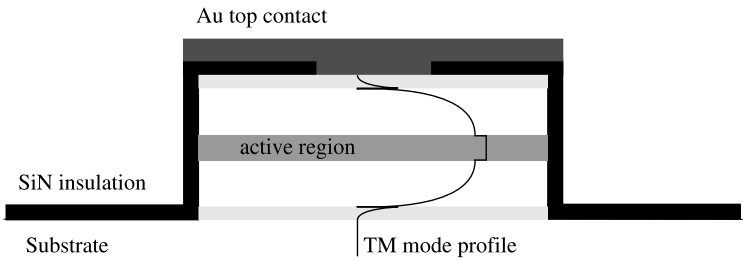

Figure 2.1: Schematic cross section of a typical QCL ridge waveguide showing a one-dimensional TM mode profile.

figure that a QCL waveguide is a two-dimensional structure, in this work however, a one-dimensional approximation is used. This approximation is valid when the ridge

width is much larger than the emission wavelength, as generally is the case with QCLs [2].

2.2 One-dimensional optical waveguide solver

2.2.1 Transfer matrix method

The geometry of a one-dimensional multilayer dielectric waveguide is shown in Fig. 2.2. For a transverse electric (TE) mode propagating in the $+z$ direction in the i^{th} layer

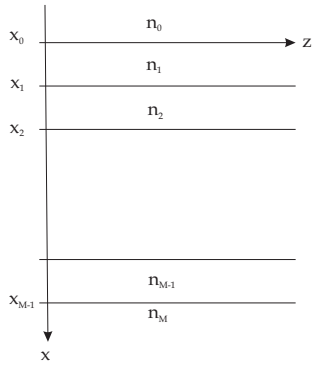

Figure 2.2: Geometry of a multilayer dielectric waveguide

$(x_{i-1} \leq x \leq x_i)$ of thickness d_i which has a constant refractive index n_i and permeability $\mu_r = 1$, the electric field is given by the product of a plane wave propagating in the $+z$ direction with a propagation constant γ ($\gamma = \beta + j\alpha$, where β and α are the phase and attenuation propagation constants respectively) modulated by an amplitude $E_{yi}(x)$. The electric field distribution has the form

$$E_{yi}(x) = A_i \exp[-\kappa_i(x - x_{i-1})] + B_i \exp[\kappa_i(x - x_{i-1})] \tag{2.2}$$

where $\kappa_i = \sqrt{\gamma^2 - k_0^2 n_i^2}$ are the complex transverse wavevectors, $k_0 = 2\pi/\lambda_0$ and λ_0 is the free-space wavelength. In order to calculate the waveguide parameters, a transfer-matrix method (TMM) has been adopted. This method is relatively easy to implement and allows one to calculate the waveguide parameters for a waveguide with a arbitrary number of layers, each with different material parameters. The transfer matrix of the i^{th} layer is given by (see Appendix B for a full derivation):

$$\mathcal{Q}_i = \frac{\epsilon_i}{2\epsilon_{i+1}} \begin{pmatrix} \left[1 + f_i \frac{\kappa_i}{\kappa_{i+1}}\right] \exp[-\kappa_i d_i] & \left[1 - f_i \frac{\kappa_i}{\kappa_{i+1}}\right] \exp[\kappa_i d_i] \\ \left[1 - f_i \frac{\kappa_i}{\kappa_{i+1}}\right] \exp[-\kappa_i d_i] & \left[1 + f_i \frac{\kappa_i}{\kappa_{i+1}}\right] \exp[\kappa_i d_i] \end{pmatrix}$$

For a TE mode, $f_i = 1$ and for a Transverse Magnetic (TM) mode, $f_i = \epsilon_{i+1}/\epsilon_i$ [3]. Following the intersubband selection rules, QCLs emit radiation in a TM mode and therefore this chapter will concentrate on the fundamental TM mode. The transfer matrix of the entire waveguide is from

$$\mathcal{Q}_{wg} = \prod_{i=M-1}^{0} \mathcal{Q}_i. \tag{2.3}$$

The field coefficients of the first and last layer can then be related using $\mathcal{Q}_{wg}$.

$$\begin{pmatrix} A_M \\ B_M \end{pmatrix} = \mathcal{Q}_{wg} \begin{pmatrix} A_0 \\ B_0 \end{pmatrix}$$

$$\begin{pmatrix} A_M \\ B_M \end{pmatrix} = \begin{pmatrix} q_{11} & q_{12} \\ q_{21} & q_{22} \end{pmatrix} \begin{pmatrix} A_0 \\ B_0 \end{pmatrix}$$

where q_{ij} are the elements of the waveguide transfer matrix $\mathcal{Q}_{wg}$. For guided modes, the fields must be evanescent and therefore A_0 and B_M must be zero. All the coefficients are proportional to B_0 and it is set to unity to normalise the field distribution. From the above equations it can be seen that a guided mode solution exists when $q_{22} = 0$. This leads to the dispersion equation for the waveguide which is solved numerically to determine the propagation constant γ

$$q_{22}(\gamma) = 0. \tag{2.4}$$

2.2.2 Steepest descent method

Finding the value of γ that makes $q_{22} = 0$ involves finding the roots of a complex function. Fig. 2.3 shows the complex plane of q_{22} for a MIR GaAs-based QCL waveguide[1]. Generally, a QCL waveguide supports more than one mode and each of these is represented by a root (i.e. the bottom of the one of the 'valleys') in Fig. 2.3. After inspecting Fig. 2.3 it becomes clear that finding the roots of a complex function is more difficult

[1]The complex plane of all QCL waveguides has the same general shape.

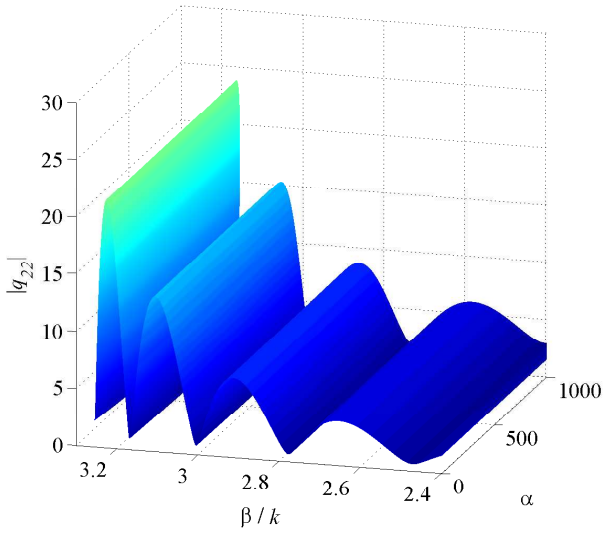

Figure 2.3: Complex plane of q_{22} for a QCL waveguide. Each of the waveguide modes is found at the bottom of each 'valley'.

than finding the roots of a standard purely-real function. This problem can be thought of as finding the lowest point on hilly terrain, where the terrain is analogous to the complex plane. The fundamental mode is generally the one of interest and this is the one with the highest value of β/k_0 (which is the effective mode index n). In order to find these complex roots, a 'steepest descent' method is used. Fig. 2.4 outlines this method. Following an initial guess, the values of q_{22} are found at the surrounding

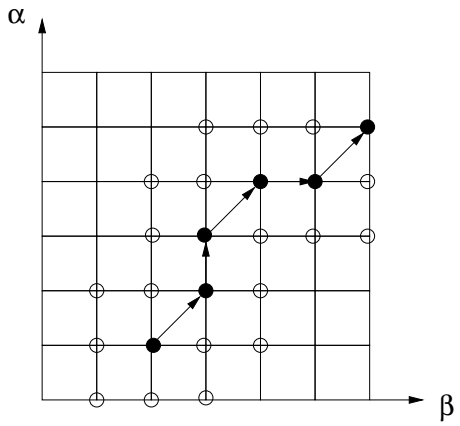

Figure 2.4: The 'steepest descent' method. The solid circles represent the lowest values and the open circles represent the surrounding points.

points in the complex plane. Whichever is the lowest point becomes the next central point and the process is repeated until the central point is the lowest value. Once the root has been found, the step length is reduced until the lowest point is found once again. This is repeated until the root, and hence γ, is found to the required degree of accuracy. In order to find the correct root, i.e. the fundamental waveguide mode, an appropriate initial guess must be made. This is achieved by suggesting a suitable value of n. It will be shown in later sections that n can be thought of as an 'average' refractive index of the waveguide and due to the III-V semiconductors having refractive indexes in the range ∼3–3.8, any value in this range will converge to the fundamental waveguide mode. Higher-order modes have smaller effective mode indexes and so if one is interested in a higher-order waveguide mode, reducing the value of the initial guess of n will result in one of the higher-order modes being found.

2.2.3 Calculation of waveguide parameters

Once γ ($= \beta + j\alpha$) has been determined, the waveguide parameters can be determined. The effective mode index of the waveguide mode is given determined by the the phase propagation constant β

$$n = \frac{\beta}{k_0}. \tag{2.5}$$

The waveguide loss α_{W} is given by

$$\alpha_{\mathrm{W}} = 2\alpha \tag{2.6}$$

and the waveguide mirror losses can be calculated from

$$\alpha_{\mathrm{M}} = \frac{1}{L}\ln(R) \tag{2.7}$$

where L is the cavity length and R is the Fresnel reflection coefficient at the semiconductor/air interface

$$R = \left(\frac{n-1}{n+1}\right)^2. \tag{2.8}$$

In order to find the mode overlap factor Γ, $E_y(x)$ must be plotted using Eqn. B.3. Up to this point, all the individual values of A_i and B_i have not needed to be known, however to plot the mode profile, these values must be known and can be found using the relation

$$\begin{pmatrix} A_i \\ B_i \end{pmatrix} = \prod_{j=i-1}^{0} \mathcal{Q}_j \begin{pmatrix} 0 \\ 1 \end{pmatrix}$$

Once the A and B coefficients have been found, $E_y(x)$ can be plotted and Γ found using

$$\Gamma = \frac{\int_0^d |E_y(x)|^2 dx}{\int_{-\infty}^{+\infty} |E_y(x)|^2 dx} \tag{2.9}$$

where d is the width of the waveguide active region.

2.3 Optical properties of materials

2.3.1 Complex dielectric constant

Semi-insulating semiconductors

It is clear from the previous section that the waveguide properties are primarily determined by the individual layer thicknesses d_i and the refractive indices n_i (and hence the dielectric constants, $\epsilon = n^2$) of the layers. In general, the dielectric function of a semiconductor is dispersive and complex.

$$\epsilon(\omega) = \epsilon_r(\omega) + i\epsilon_i(\omega) \tag{2.10}$$

where $\omega = 2\pi f = 2\pi c/\lambda$, f is the frequency, λ is the wavelength and c is the speed of light in a vacuum. Therefore the refractive index is also complex and frequency dependent

$$n'(\omega) = n(\omega) + ik(\omega) = \sqrt{\epsilon(\omega)} \tag{2.11}$$

where n is the ordinary (real) refractive index and k is known as the extinction coefficient. The real and imaginary parts of the dielectric constant can be described in terms of the real and imaginary parts of the refractive index

$$\epsilon_r = n^2 - k^2 \tag{2.12}$$

and

$$\epsilon_i = 2nk. \tag{2.13}$$

Similarly, the real and imaginary parts of the refractive index can be described in terms of the real and imaginary parts of the dielectric constant

$$n = \sqrt{\frac{\sqrt{\epsilon_r^2 + \epsilon_i^2} + \epsilon_r}{2}} \tag{2.14}$$

and

$$k = \sqrt{\frac{\sqrt{\epsilon_r^2 + \epsilon_i^2} - \epsilon_r}{2}}. \tag{2.15}$$

The absorption coefficient of the semiconductor is intrinsically linked to the extinction coefficient and is calculated from [4]

$$\alpha = \frac{4\pi}{\lambda} k. \tag{2.16}$$

In the infrared region of the EM spectrum, the complex dielectric constant of semiconductors can be explained by a damped harmonic oscillator model [4]

$$\epsilon(\omega) = \epsilon_\infty \left(1 + \frac{\omega_{\text{LO}}^2 - \omega_{\text{TO}}^2}{\omega_{\text{TO}}^2 - \omega^2 - i\omega\gamma}\right) \tag{2.17}$$

where ϵ_∞ is the high frequency dielectric constant, ω_{LO}^2 and ω_{TO}^2 are the long-wavelength LO and transverse-optical (TO) phonon frequencies respectively and γ is the phonon damping constant. Table 2.1 lists the values used in Eqn. 2.17 for the important III-V semiconductor binaries [4, 5]. The dispersion relations for the material

Material	ϵ_∞	ω_{LO} (cm^{-1})	ω_{TO} (cm^{-1})	γ (cm^{-1})
GaAs	10.89	292.1	268.7	2.4
AlAs	8.48	401.5	361.8	8
InAs	12.25	240	218	4
InP	9.61	345.0	303.7	3.5

Table 2.1: Binary material parameters used in the damped single harmonic oscillator model

in Table 2.1 are shown in Fig. 2.5

The dispersion that can be seen in the figures is caused by the EM field at these frequencies (called the Reststrahlen region) interacting with fundamental lattice vi-

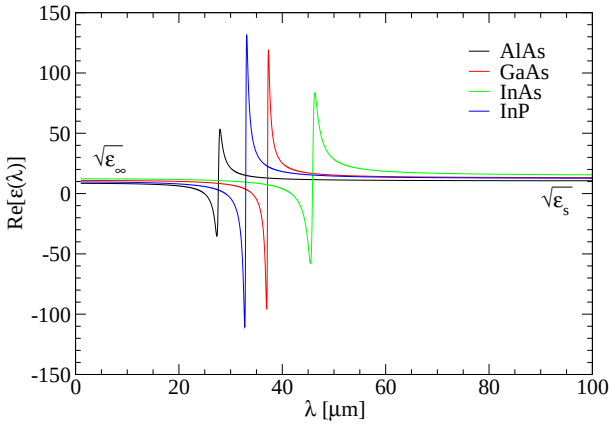

(a) $\Re\epsilon(\lambda)$

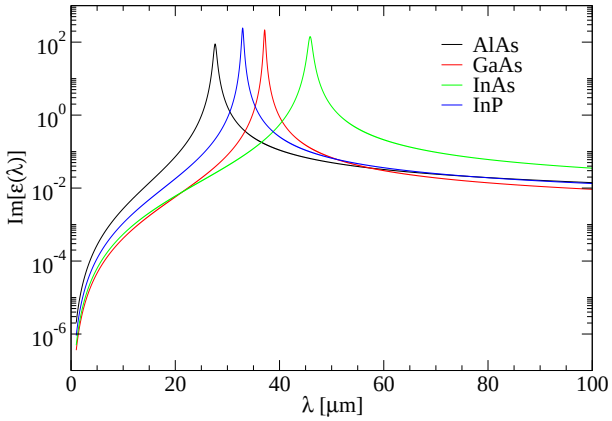

(b) $\Im\epsilon(\lambda)$

Figure 2.5: Dispersion relations of important III-V binaries showing the (a) real and (b) imaginary parts of the complex dielectric constant.

brations. This results in the absorption or emission of EM waves due to lattice vibrations being annihilated or created and also scattering of the EM wave due to the lattice vibrations. It is important to see the difference in the refractive index above and below the Reststrahlen region. On the long wavelength side of the Reststrahlen region (lower frequency) the refractive index is higher and tends towards the root of the static dielectric constant (ϵ_s) while on the shorter wavelength side (higher frequency) the refractive index is lower and tends towards the root of the high frequency dielectric constant (ϵ_∞). The difference in the dielectric constants is due to different polarisation mechanisms that come into play at different frequencies. At frequencies below the Reststrahlen band (far-infrared) the phase velocity is determined by both electronic and ionic polarisation, however, above the Reststrahlen band at optical frequencies,

ionic polarisation is too slow to respond to the EM field and hence the phase velocity is determined by only electronic polarisation and is therefore larger. Given that the refractive index can be defined as $n = c/v$ (where v is the phase velocity), a larger phase velocity results in a lower refractive index.

Fig. 2.6 shows the absorption coefficient of the important III-V binaries calculated using the values in Table 2.1 and Eqn. 2.16. It can be seen that the absorption is

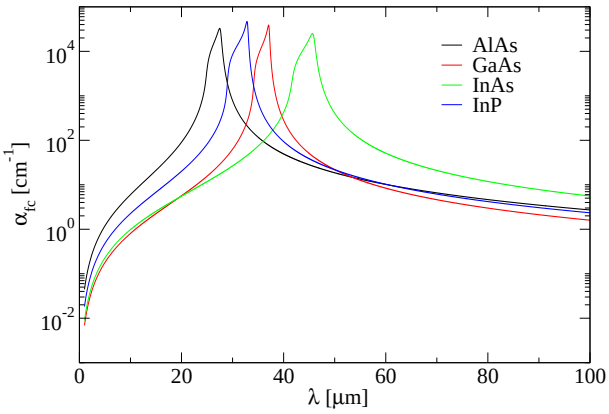

Figure 2.6: Absorption coefficient of the important III-V binaries in the vicinity of the Reststrahlen region.

very strong around the Reststrahlen region due to interaction of the EM wave with fundamental lattice vibrations and prevents laser emission at wavelengths around the phonon energies in the semiconductor.

The dielectric constants of the III-V ternary alloys display two-mode behaviour associated with the constituent binary materials. This two-mode behaviour is calculated by linearly interpolating between dielectric constants of the relevant binaries (i.e. Abele's interpolation (Appendix C) with the bowing parameter equal to zero). The dispersion relations of the important III-V ternaries ($In_{0.53}Ga_{0.47}As$, $In_{0.52}Al_{0.48}As$ and $Al_{0.45}Ga_{0.55}As$) are shown in Fig. 2.7. The GaAs-, InAs- and AlAs-like phonon like modes are highlighted on the figures. The absorption coefficient for the ternaries as a function of wavelength is shown in Fig. 2.8.

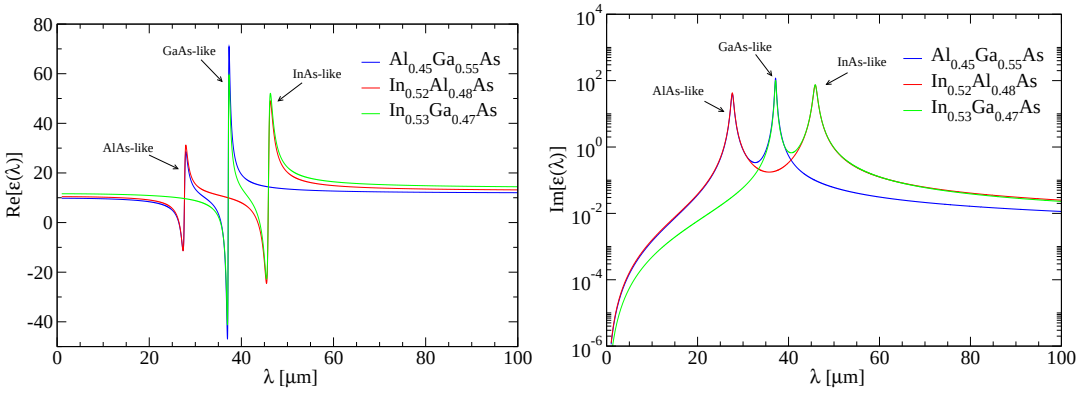

(a) $\Re\epsilon(\lambda)$ (b) $\Im\epsilon(\lambda)$

Figure 2.7: Dispersion relations of important III-V ternaries showing the (a) real and (b) imaginary parts of the complex dielectric constant.

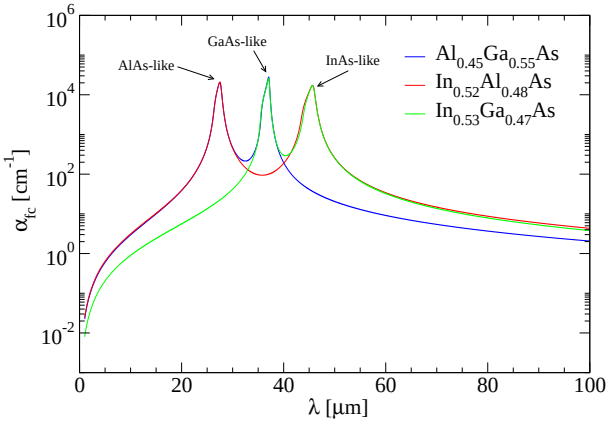

Figure 2.8: Absorption coefficient of the important III-V ternaries in the vicinity of the Reststrahlen region.

Doped semiconductors

Eqn. 2.17 is valid for semi-insulating semiconductors, but if the semiconductor is doped, the equation must be modified to take into account plasma contributions to the dielectric constant from the free carriers

$$\epsilon(\omega) = \epsilon_\infty \left(1 + \epsilon_{\text{phonon}} - \epsilon_{\text{plasma}}\right). \tag{2.18}$$

The total relation for the dielectric constant then reads

$$\epsilon(\omega) = \epsilon_\infty \left(1 + \frac{\omega_{\text{LO}}^2 - \omega_{\text{TO}}^2}{\omega_{\text{TO}}^2 - \omega^2 - \jmath\omega\gamma} - \frac{\omega_p^2}{\omega(\omega + \jmath\omega_a)}\right) \tag{2.19}$$

and is known as the Drude-Lorentz model. ω_p is the plasma frequency and ω_a is the plasma damping constant[2]. The plasma frequency is calculated by

$$\omega_p = \sqrt{\frac{N_d q^2}{\epsilon_0 \epsilon_\infty m}} \tag{2.20}$$

where N_d is the concentration of the free carriers, q is the charge of an electron, ϵ_0 is the permittivity of free space and m is the mass of an electron in the semiconductor ($m = m^* m_0$, where m^* is the effective mass and m_0 is the electron rest mass). The plasmon damping constant is calculated using [3]

$$\omega_a = \frac{q}{m\mu} \tag{2.21}$$

where μ is the electron mobility. The effective masses of the important semiconductors used in QCLs are listed in Table C.1.

A resonant semiconductor plasma can be defined as a material with Re[$\epsilon(\omega)$]=0. Considering just the plasma contributions to the dielectric constant

$$\epsilon_r(\omega) = \epsilon_\infty \left(1 - \frac{\omega_p^2}{\omega^2 + \omega_a^2}\right) \tag{2.22}$$

and

$$\epsilon_i(\omega) = -\frac{\epsilon_\infty \omega_a \omega_p^2}{\omega(\omega^2 + \omega_a^2)}. \tag{2.23}$$

For the case when $\omega \gg \omega_a$,

$$\epsilon_r(\omega) = \epsilon_\infty \left(1 - \frac{\omega_p^2}{\omega^2}\right) \tag{2.24}$$

and the semiconductor is a resonant plasma (i.e. Re[$\epsilon(\omega)$]=0) when $\omega = \omega_p$. If the effect of ω_a is taken into account, Eqn. 2.22 equals zero when

$$\omega = \sqrt{\omega_p^2 - \omega_a^2}. \tag{2.25}$$

Defining $\sqrt{\omega_p^2 - \omega_a^2}$ as ω_0, when $\omega < \omega_0$, Re[$\epsilon(\omega)$]< 0 and the electron gas in the plasma exhibits metallic behaviour. When $\omega > \omega_0$, Re[$\epsilon(\omega)$]> 0 and the electron gas in the plasma exhibits dielectric behaviour.

[2]It should be noted that ω_a is the inverse of the electron momentum relaxation time τ.

Free-carrier absorption

Free-carrier absorption in semiconductors is caused by electrons undergoing transitions in any one energy band and is the primary loss mechanism in QCLs waveguides (i.e. electrons in the conduction band). Free carrier absorption is calculated using Eqns. 2.16 and 2.13

$$\alpha_{fc} = \frac{4\pi}{\lambda}k = \frac{\omega\epsilon_i}{cn}. \tag{2.26}$$

When $\omega > \omega_p$, the Drude scattering time is generally long enough such that $\omega \gg \omega_a$ and Eqn. 2.23 reduces to

$$\epsilon_i(\omega) = -\frac{\epsilon_\infty \omega_a \omega_p^2}{\omega^3}. \tag{2.27}$$

Inserting this into Eqn. 2.26 and remembering $n = \sqrt{\epsilon}$ gives

$$\alpha_{fc} = \frac{\epsilon\omega_a\omega_p^2}{\omega^2 c\sqrt{\epsilon}}. \tag{2.28}$$

Substituting in Eqns. 2.20 and 2.21 and converting to wavelength using $\omega = 2\pi f$ gives

$$\alpha_{fc} = \frac{N_d q^3 \sqrt{\epsilon}\lambda^2}{4\pi^2 c^3 m^2 \epsilon_0 \mu}. \tag{2.29}$$

It can be seen that in the first approximation, the free carrier losses (and hence the waveguide losses) are proportional to λ^2. However, this relationship breaks down as the emission wavelength approaches the plasma wavelength and/or when ω_a is comparable in magnitude to ω. It is also apparent that the losses are directly proportional to the doping density and inversely proportional to the electron mobility. To complicate matters further, the electron mobility is a function of both doping density and temperature.

2.3.2 Electron mobility

In this work, a Caughey–Thomas-like mobility model is used [6]. This is an empirical model in which parameters for a variety of III-V semiconductors have been fitted to a wide range of experimental data over a range of doping concentrations and temperatures. The mobility in this model is expressed as

$$\mu(N_d, T) = \mu_{min} + \frac{\mu_L - \mu_{min}}{1 + \left(\frac{N_d}{N_{ref}}\right)^{\gamma_3}} \tag{2.30}$$

where μ_{min} is the value that the mobility saturates to at very high doping which is temperature independent and μ_L is the contribution to the mobility from lattice scattering and is given by

$$\mu_L = \mu_L^{300} \left(\frac{T}{300} \right)^{\gamma_1} \tag{2.31}$$

and N_{ref} is given by

$$N_{ref} = N_{ref}^{300} \left(\frac{T}{300} \right)^{\gamma_2}. \tag{2.32}$$

Table 2.2 lists the fitting parameters for the main semiconductor materials used in QCLs. To test the validity of the model, it was used to calculate the effect of doping on

Material	μ_L^{300} [cm^2/Vs]	γ_1	μ_{min}	N_{ref}^{300} [cm^{-3}]	γ_2	γ_3
GaAs	9400	-2.2	950	1×10^{17}	5.5	0.5
AlAs	410	-2.1	10	5.5×10^{17}	3	1
InP	5800	-1.9	400	4×10^{17}	5.4	0.5
$In_{0.53}Ga_{0.47}As$	14000	-1.59	300	1.3×10^{17}	3.68	0.48
$In_{0.52}Al_{0.48}As$	4800	-1.46	800	3×10^{16}	3	1.10

Table 2.2: Fitting parameters for the mobility model

the mobility for multiple GaAs samples at 77 and 300 K. The results of the simulation and the experimentally measured values[3] are displayed in Fig. 2.9. The good fit between the simulated and experimentally measured mobility values is clearly shown in the figure. The mobility reduces as the doping density increases due to the increased influence of ionised impurity scattering at higher doping levels. At very low doping concentrations, the mobility saturates at μ_L, which is the lattice-limited mobility which is shown in figure 2.10 along with the effect of temperature on the mobility of GaAs for a series of doping concentrations. At low temperatures the mobility is primarily determined by ionised impurity scattering, whilst at high temperatures, the mobility is determined by phonon scattering and saturates at the lattice-limited mobility regardless of the doping density. Fig. 2.11 shows the variation of electron mobility with

[3]Thanks to Prof. Edmund Linfield and Suraj P. Khanna for supplying the experimentally measured values for the GaAs samples.

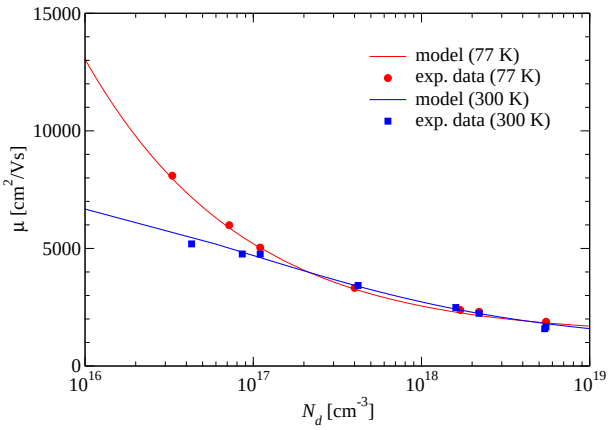

Figure 2.9: GaAs electron mobility as a function of doping density. The solid symbols are experimentally measured values and the lines are the result of the model.

doping density at $T = 300$ K for the QCL materials listed in Table 2.2.

2.3.3 Complex refractive index

By following the previous sections it should be apparent that the complex refractive index is determined by the EM field interacting with both phonons and the free carriers (plasma). The interaction with phonons is inherent to the material system whilst interaction with the free carriers is determined by the plasma frequency (which is dependent upon the doping density) and the plasma damping frequency (which is dependent upon the electron mobility). It has been discussed how the mobility is also dependent upon doping density so it follows that for a particular material, the complex refractive index at a particular wavelength is dependent upon only the doping density and temperature (through the mobility).

To calculate the complex refractive index for a given doping density in a particular material, the plasma frequency is first calculated using Eqn. 2.20. The mobility is then estimated using the Caughey–Thomas-like mobility model in Sec. 2.3.2 (for a given temperature). The plasmon damping constant can then be calculated using Eqn. 2.21 and the complex dielectric constant obtained from the Drude–Lorentz model (Eqn. 2.19) from which the complex refractive index is simply the root of this.

The complex refractive index of GaAs was calculated using the above procedure at 300 K as a function of wavelength for various doping densities. The real part of

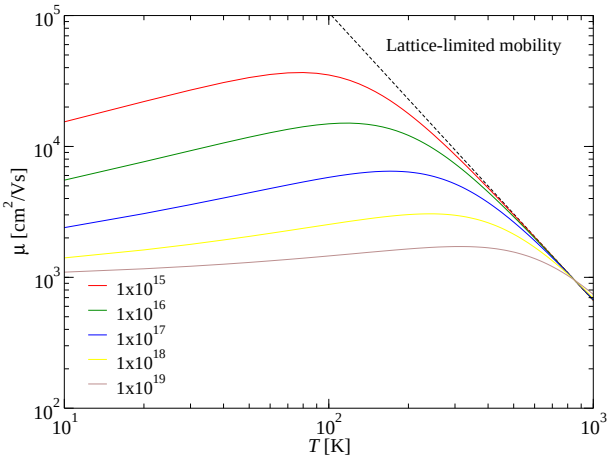

Figure 2.10: GaAs electron mobility as a function of temperature for a range of doping densities (cm^{-3}). The lattice-limited mobility is shown as a dashed line.

the refractive index and the free carrier losses are plotted in figure 2.12. It can be seen from Fig. 2.12(a) that strong dispersion occurs around the Reststrahlen region due to interaction with phonons for all values of doping density. There is also additional dispersion which occurs at different wavelengths depending upon the doping density. The wavelength at which this occurs is actually the plasma wavelength. The plasma wavelength for GaAs as a function of doping density is plotted in Fig. 2.13. Each of the dispersions in Fig. 2.12(a) can be explained by finding the corresponding plasma wavelength for each doping density in Fig. 2.13. As discussed in Sec. 2.3.1, when the wavelength is equal to the plasma wavelength, the real part of the complex dielectric constant is approximately equal to zero which strongly reduces the real part of the refractive index[4].

Fig. 2.12(b) shows that in general, the free carrier losses increase with doping density and also with wavelength. Eqn. 2.29 predicts that the loss increases with λ^2 and Fig. 2.12(b) confirms this is true up to $\sim 20\mu$m (i.e. the straight lines on the figure). It can be seen that close to and above the Reststrahlen region, this relation breaks down, especially at higher doping densities. The reason for this is two-fold. Firstly, (as shown by the dashed line in Fig. 2.12(b)) it breaks down when the wavelength is longer than

[4] As seen in Fig. 2.12(a), the real part of the refractive index does not actually go to zero. This is due to the real part of the refractive index also having a contribution from the imaginary part of the dielectric constant (Eqn. 2.14) which is non-zero at the plasma wavelength.

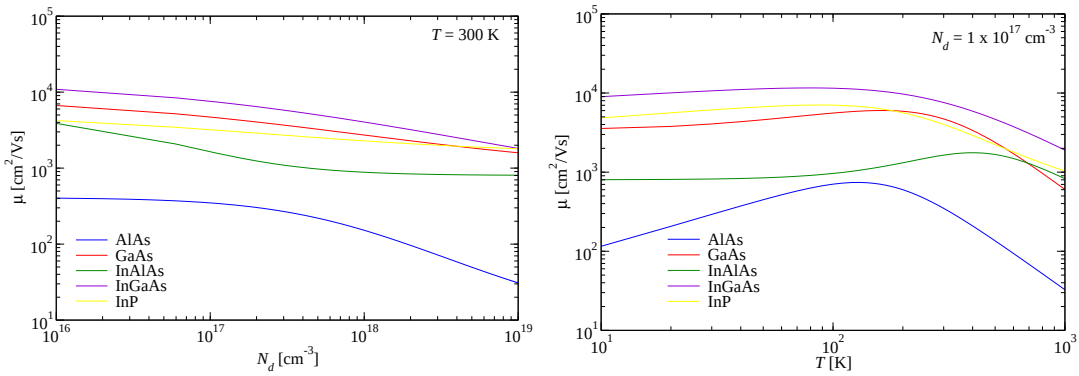

(a) Doping variation

(b) Temperature variation

Figure 2.11: Electron mobility as a function of (a) doping density at $T = 300$ K and (b) temperature at $N_d = 1 \times 10^{17}$ cm^{-3} for the important QCL III-V semiconductors at $T = 300$ K.

the plasma wavelength invalidating the approximation $\omega > \omega_p$ used in the derivation of Eqn. 2.29. Secondly, the mobility decreases as the doping density increases leading to an increase in ω_a. This causes the approximation $\omega \gg \omega_a$ used in the derivation of Eqn. 2.29 to become less valid especially when ω is smaller i.e. when λ is larger.

Fig. 2.14(a) shows the real part of the refractive index of GaAs doped to 1×10^{17} cm^{-3} as a function of wavelength at different temperatures. It can be seen that for wavelengths less than $\sim 50\mu$m, the real part of the refractive index is independent of temperature. For these wavelengths $\omega \gg \omega_a$ and therefore Eqn. 2.19 is less sensitive to changes in temperature (which changes the mobility and hence ω_a). As the wavelength increases (and hence ω decreases), Eqn. 2.19 becomes more sensitive to changes in ω_a. From Figs. 2.14(a) and 2.10 it can be seen that the change in refractive index is larger for temperatures where the mobility is large.

Fig. 2.14(b) shows that the free carrier losses are larger for temperature with smaller mobilites, which is also shown in Eqn. 2.29. However, as before this relationship breaks down when the wavelength becomes larger than the plasma wavelength ($\sim 90\mu$m at a doping density of 1×10^{17} cm^{-3}).

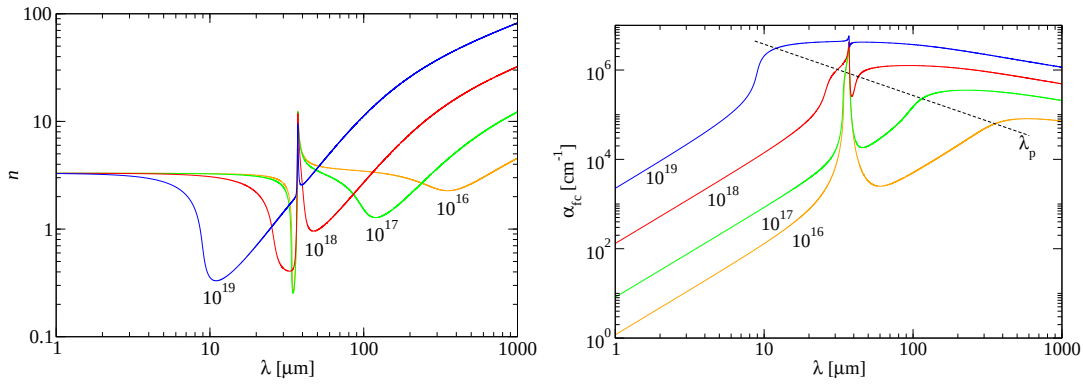

(a) n (b) $\alpha_{fc} = \frac{4\pi k}{\lambda}$

Figure 2.12: (a) Real part of the refractive index and (b) free carrier losses in GaAs as a function of wavelength $T = 300$ K for various doping densities (cm^{-3}).

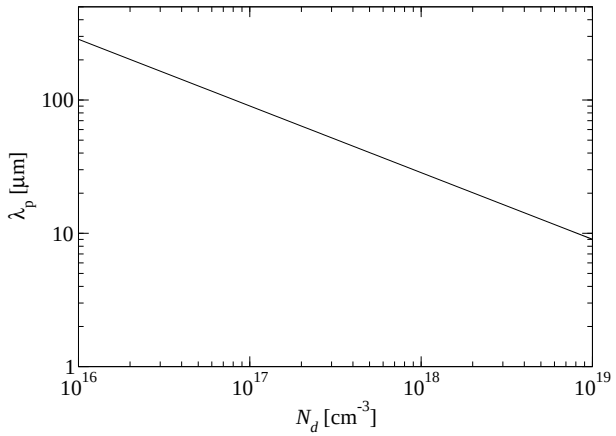

Figure 2.13: Plasma wavelength in GaAs as a function of doping density.

Active region refractive index

The model presented in the previous sections is valid for bulk semiconductors. However, as discussed in Chapter 1, the active region and injector stack of a QCL are made up of semiconductor superlattices. The quantum confinement properties that arise from the superlattice affect the mobility of the two-dimensional electron gas (2DEG) in the QCL. This effect would be very difficult to model and therefore for simplicity, the refractive index of the QCL-active region/injector stack is modelled as a linear interpolation between the refractive indices of the constituent alloys according to their

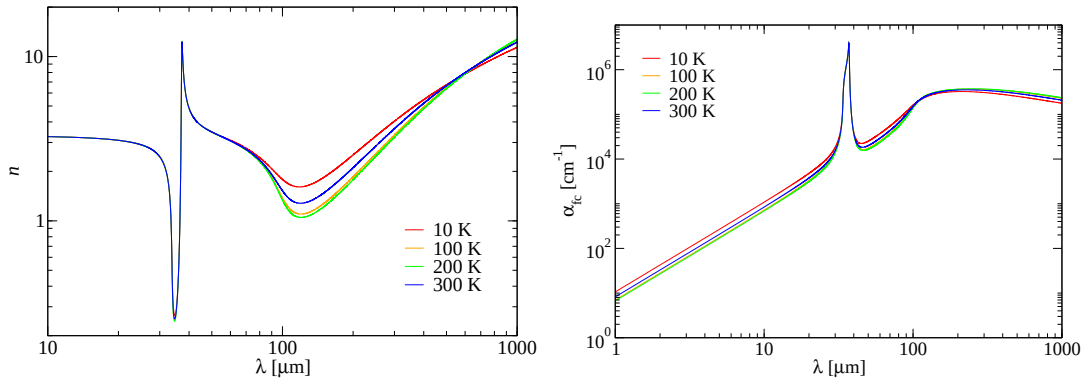

(a) n (b) $\alpha_{fc} = \frac{4\pi k}{\lambda}$

Figure 2.14: (a) Real part of refractive index and (b) free carrier losses as a function of wavelength at different temperatures at a doping density of 1×10^{17} cm^{-3}.

respective fractions.

$$n_{AR} = x n_{\text{well}} + (1 - x) n_{\text{barrier}} \tag{2.33}$$

where x is the fraction of the well material with refractive index n_{well} and n_{barrier} is the refractive index of the barrier material [5].

With regards to the active region/injector region doping density, in general only a few wells/barriers in the injector region are doped. To model this, the doping density is averaged out across the entire active region stack. The active region doping density is calculated from the sheet doping density (N_s) by

$$N_d = \frac{N_s}{L_d} \tag{2.34}$$

where L_d is the length of the doped regions. It follows that the effective doping density ($\overline{N_d}$) is given by

$$\overline{N_d} = \frac{N_d L_d}{L_p} = \frac{N_s}{L_p} \tag{2.35}$$

where L_p is the length of the period.

[5] In the case of GaAs-based QCLs with GaAs wells and $Al_xGa_{1-x}As$ barriers it follows that the active region is considered as purely $Al_xGa_{1-x}As$ with an effective value of x determined by the Al content of the barrier and the ratio of the total length of the barriers to the period length

2.3.4 Dielectric constant of metallic layers

As well as semiconductor layers, QCL waveguides also contain metallic layers, generally used as electrical contact layers. The complex dielectric constant of a metal is described by the plasma contribution in the Drude model. Table 2.3 lists the values of ω_p and ω_a for various metals [5, 7, 8].

Metal	Au	Pd	Ag	Cu
ω_p (eV)	9.03	9.72	9.01	10.83
ω_a (meV)	53.0	8.0	48.0	30.0

Table 2.3: Values of ω_p and ω_a for various metals

Unfortunately, due to a lack of data in the literature, the effect of temperature on the optical properties of metals is ignored in this work and room temperature values are used in all cases.

2.4 Mid-infrared QCL optical waveguide analysis

This section combines the theory set out in Secs. 2.2 and 2.3 to analyse the different QCL waveguiding schemes that are used in the MIR. Generally, the particular scheme that is employed is determined by the material system that is being used and the wavelength of interest.

2.4.1 Plasmon-enhanced waveguides

Dielectric waveguides are obvious choices if the particular material system provides a sufficiently large refractive index mismatch between the high refractive index waveguide core containing the QCL-active region and injector stack and the lower refractive index waveguide cladding layers. InP has a refractive of ~ 3.1 and hence provides natural cladding layers for the InGaAs/InAlAs QCL-active region/injector stack ($n \sim 3.3$, depending upon the respective fractions). Since the InP substrate can provide lower cladding, the time for the MBE growth can be significantly reduced. The upper

cladding can either be formed by InP or by low-refractive index InAlAs ($n \sim 3.2$).

On top of the QCL waveguide, a metal layer is deposited to form the top electrical contact. If the optical mode couples to the surface-plasmon at the metal–semiconductor interface (see next section for more details) additional waveguides losses are introduced. It would be possible just to increase the thickness of the upper cladding layer to reduce this coupling but this would also increase the MBE growth time. To alleviate this problem, 'plasmon-enhanced' waveguides were developed [9]. A schematic diagram of a plasmon-enhanced waveguide is shown in Fig. 2.15. In this

InGaAs	$7x10^{18}$	600 nm
InAlAs	$3x10^{17}$	1200 nm
InAlAs	$1.2x10^{17}$	1200 nm
InGaAs	$6x10^{16}$	500 nm
Active region	$2.6x10^{16}$	1732 nm
InGaAs	$6x10^{16}$	700 nm
InP	$4x10^{17}$ (n^{+} substrate)	

Figure 2.15: Schematic diagram of a plasmon-enhanced waveguide.

type of waveguide, a highly doped (n^{++}) semiconductor layer (InGaAs) is grown on top of the upper InAlAs cladding layers. As discussed previously, when the doping is high enough, the plasma wavelength of the n^{++} layer approaches the wavelength of the waveguide mode and there is a resulting strong decrease in the refractive index of the layer, increasing the optical confinement and reducing the overlap with the lossy metal contact layer.

Waveguide parameters

Fig. 2.16 shows the profile of the fundamental TM mode in a $\lambda \sim 8.4\mu$m InP-based QCL with a plasmon-enhanced waveguide [9]. The figure shows the calculated overlap of the the optical mode with the active region to be $\Gamma = 0.41$ and an effective mode index of $N = 3.22$. These are in excellent agreement with the values of $\Gamma = 0.41$ and $N = 3.25$ in Ref. [9]. Fig. 2.17 shows the refractive index profile and the waveguide

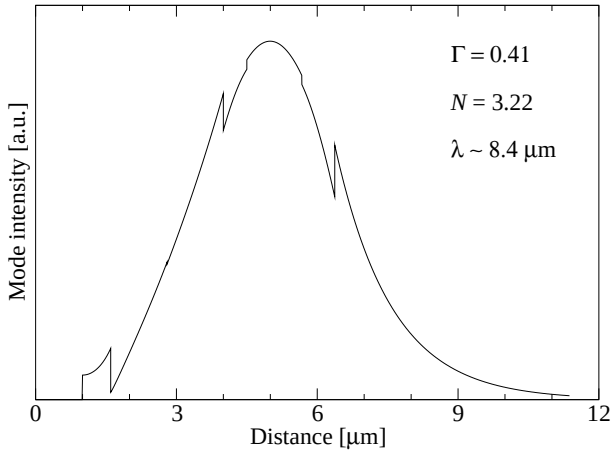

Figure 2.16: TM mode profile in a $\lambda \sim 8.4\mu$m InP-based QCL with a plasmon-enhanced waveguide.

structure and the free-carrier losses associated with the waveguide layers. It can be

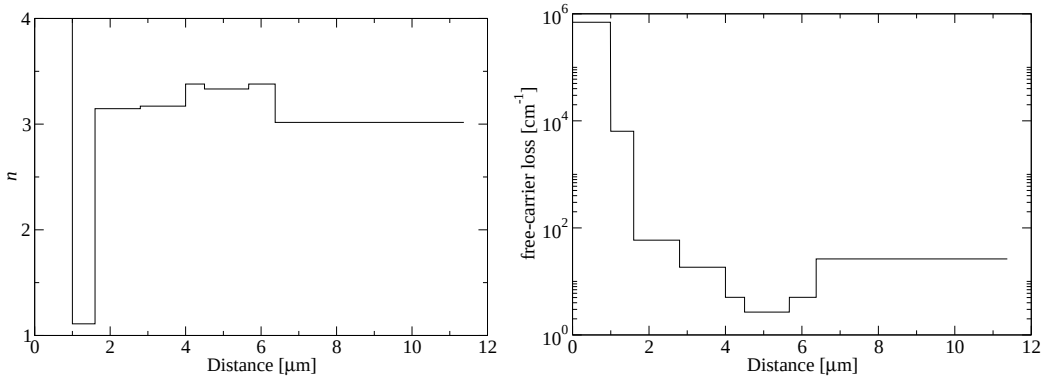

(a) n (b) α_{fc}

Figure 2.17: (a) Refractive index profile of the structure and (b) free carrier losses in each of the waveguide layers.

seen from Fig. 2.17(a) that the refractive index of the n^{++} layer is strongly reduced which enhances the optical confinement and keeps the optical mode away from the highly-lossy top metal layer (Fig. 2.17(b)). At 300 K, the waveguide loss α_W is calculated to be 16.5 cm^{-1}, of which 13.1 cm^{-1} is associated with the n^{++} layer (the layer has a loss of ~ 6400 cm^{-1} and an overlap of 0.002 with the optical mode). Even though the metal layer has a loss of 7×10^5 cm^{-1} at this wavelength, the reduced refractive index of the n^{++} layer prevents any of the mode overlapping with the metal, eliminating

the losses.

Estimation of the threshold current density

When the waveguide parameters have been calculated it is possible to estimate the threshold current density J_{th} from Eqn. 1.22. In Ref. [9], g was calculated to be 5.7×10^{-2} cm/A at 10 K and 2.4×10^{-2} cm/A at 100 K. J_{th} was then estimated (with $\alpha_m = 7.8$ cm^{-1} and $\alpha_m = 9.8$ cm^{-1} for 1.3 mm long cavity) to be 0.7 kA/cm^2 at 10 K and 1.7 kA/cm^2 at 100 K. These are not in good agreement with the measured values of 2.1 and 2.8 kA/cm^2 at 10 and 100 K respectively. An underestimation of the waveguide losses was given as a possible reason for the discrepancy. Table 2.4 outlines the calculated waveguide parameters in Ref. [9] and this work and the corresponding estimated values of J_{th}. High resolution spectra of the QCL at 10 K and 100 K reveal the waveguide modes are at $\sim 8.3\mu$m and $\sim 8.4\mu$m respectively. The results displayed

Parameter	Ref. [9]		This work		Measured	
T [K]	10	100	10	100	10	100
Γ	0.41	0.41	0.41	0.41	-	-
α_{W} [cm^{-1}]	7.8	7.8	29.0	18.8	'39.2'	'17.8'
α_{M} [cm^{-1}]	9.8	9.8	9.9	9.9	-	-
g [cm/A]	5.7×10^{-2}	2.4×10^{-2}	-	-	-	-
J_{th} [kA/cm^2]	0.7	1.7	1.7	2.9	2.1	2.8

Table 2.4: Calculated and experimental results of J_{th} in a $\lambda \sim 8.4\mu$m InP-based QCL.

in Table 2.4 show that it is necessary to include the effect of temperature when calculating the waveguide parameters in order to obtain good agreement with experiment [6].

[6] The 'measured' waveguide losses are obtained using the measured values of J_{th} and Eqn. 1.22.

Exclusively InP waveguides

The plasmon-enhanced waveguide presented here utilises InAlAs upper cladding layers with a highly-doped InGaAs plasma layer to complete the optical confinement, but it is also possible to replace these layers with lower refractive index InP to improve performance[7]. Once the QCL-active region/injector has been grown on the InP substrate using MBE, the wafer is transfered to a MOCVD chamber to overgrow with InP.

When designing and optimising QCL waveguides, it is useful to define a figure of merit to compare different structures.

$$\Phi = \frac{\Gamma}{\alpha_W}. \tag{2.36}$$

This figure of merit should then be maximised to obtain optimum performance and can be used to compare different waveguide designs. The figure of merit was calculated as a function of temperature for the same layer structure as in Fig. 2.15 but with the upper cladding layers replaced by InP. The results are displayed in Fig. 2.18 together with the figure of merit for the same structure as in Fig. 2.15 for comparison. It can be seen from the figure that exclusively InP-based waveguides display far

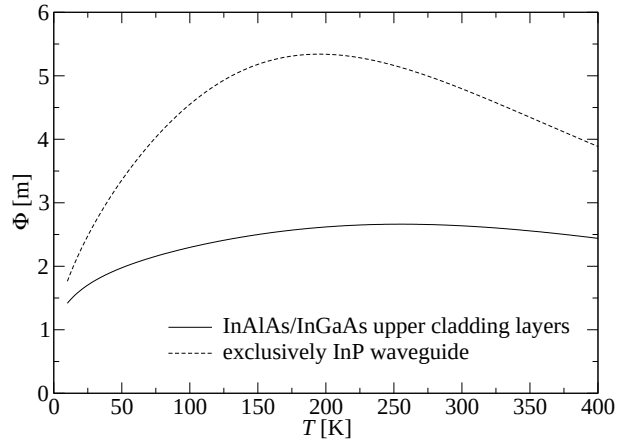

Figure 2.18: Waveguide figure of merit as a function of temperature for InP-based waveguide with upper InAlAs/InGaAs cladding layers (solid line) and exclusively InP-based waveguide (dashed line).

[7] Also, as mentioned earlier binary semiconductors have superior thermal properties compared to ternary materials

greater optical properties than equivalent InAlAs/InGaAs waveguides. The overlap factors are approximately the same in both structures (41–43 %) so the increase in performance is due to reduced waveguide losses. It should be noted that the exclusive InP-based waveguide was not optimised, the InAlAs and InGaAs layers were simply replaced by InP keeping the same thickness and doping density. If the layer structure was optimised, even greater levels of performance could be expected. This result clearly shows that exclusive InP-based waveguides are far better than waveguides with InAlAs/InGaAs upper cladding layers in terms of their optical performance, and will also have intrinsically better thermal properties. These advantages are however weighed against increased complexities in the fabrication process.

2.4.2 Double plasmon-enhanced waveguides

As discussed previously, InP-based QCLs have the natural advantage of low refractive index cladding layers. However, in the case of GaAs-based QCLs, the GaAs substrate has a higher refractive index than the QCL-active region/injector stack and therefore cannot be used as a natural cladding layer. The first GaAs-based QCL [10] utilised short AlGaAs cladding layers to act as cladding layers on both sides of the active region/injector stack together with a n^{++} GaAs upper cladding layer to complete the optical confinement. However, as well as being lossy, AlGaAs, like all ternary materials has poorer thermal properties than binary materials. Therefore a new type of GaAs-based waveguide was developed; the 'double plasmon-enhanced' waveguide[11]. A schematic diagram of a double plasmon-enhanced waveguide is shown in Fig. 2.19.

In these waveguides, both the upper and lower cladding layers are formed from n^{++} GaAs layers in which the doping has been carefully chosen so that the plasma wavelength approaches the wavelength of the waveguide mode as in the case of 'single' plasmon-enhanced waveguides used in InP-based QCLs. In order to reduce the waveguide loss, the bulk of the optical mode is separated from the lossy highly-doped layers by thick low-doped spacer layers. In this particular QCL, the barriers in the QC-active region/injector stack are made up of $Al_{0.33}Ga_{0.67}As$ and the particular ratio of

n^{++} GaAs	$6x10^{18}$	1 μm
GaAs	$4x10^{16}$	3.5 μm
Active region ($Al_{0.16}Ga_{0.84}As$)	$8.6x10^{16}$	1631 nm
GaAs	$4x10^{16}$	3.5 μm
n^{++} GaAs	$6x10^{18}$	1 μm
n^{++} GaAs substrate	$3x10^{18}$	

Figure 2.19: Schematic diagram of a double plasmon-enhanced waveguide.

well to barrier widths gives an effective $Al_{0.16}Ga_{0.84}As$ active region.

Waveguide parameters

Fig. 2.20 shows the profile of the fundamental TM mode in a $\lambda \sim 9\mu$m GaAs-based QCL with a double plasmon-enhanced waveguide [10, 11]. The figure shows the cal-

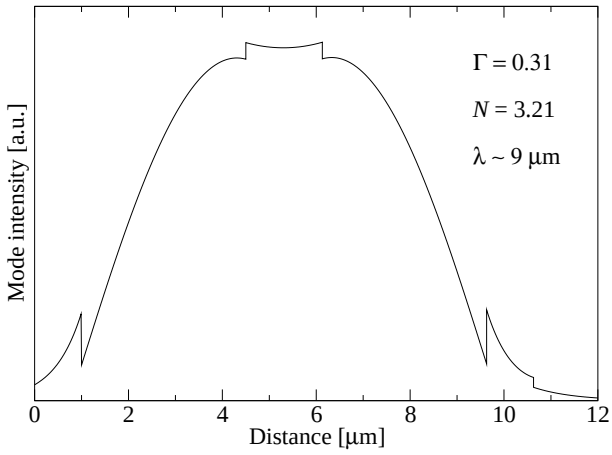

Figure 2.20: TM mode profile in a $\lambda \sim 9\mu$m GaAs-based QCL with a double plasmon-enhanced waveguide.

culated overlap of the the optical mode with the active region to be $\Gamma = 0.31$ and an effective mode index of $n = 3.21$, in perfect agreement with those in Ref. [11]. The losses at 300 K are calculated to be 16.75 cm^{-1}, in good agreement with the losses of 16 cm^{-1} in Ref. [11]. Fig. 2.21 shows the refractive index profile and the waveguide structure and the free-carrier losses associated with the waveguide layers. The doping

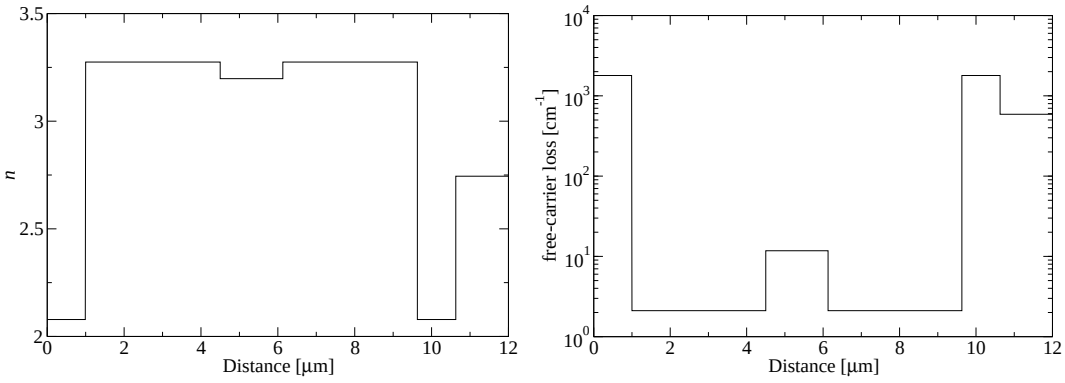

(a) n (b) α_{fc}

Figure 2.21: (a) Refractive index profile of the structure and (b) free carrier losses in each of the waveguide layers.

in the n^{++} layer is 6×10^{18} cm^{-3} which results in a plasma wavelength of $\sim 11.5\mu$m (Fig. 2.13) which is close to the waveguide mode (9.5μm) resulting in a strong decrease in the refractive index which is evident in Fig. 2.21(a). Fig. 2.21(b) shows that these layers have free-carrier losses of ~ 1750 cm^{-1} but they only have a total overlap of 0.007 with the optical mode resulting in them contributing losses of 12.30 cm^{-1} to the overall 16.75 cm^{-1} (73 %).

Waveguide losses

In Ref. [11], the waveguide loss is measured at both 10 K and 77 K and values of 21 cm^{-1} and 19 cm^{-1} are obtained respectively. The laser emission wavelength at 77 K is measured as 8.9 μm, and using the methods outlined in this chapter gives estimated waveguide losses of 16.9 cm^{-1} in reasonably good agreement with the experimentally measured ones. There is no experimental data on the emission wavelength at 10 K, but as generally the case with QCLs, there is a red-shift of the wavelength as the temperature increases. It could therefore be expected that the emission wavelength decreases from 77 K to 10 K. Fig. 2.22(a) shows the calculated waveguide loss as a function of emission wavelength. It can be seen from the figure that over this small wavelegnth range there is a linear relationship between the loss and emission wavelength as opposed to the λ^2 dependency which is predicted by Eqn. 2.29. It can be seen that

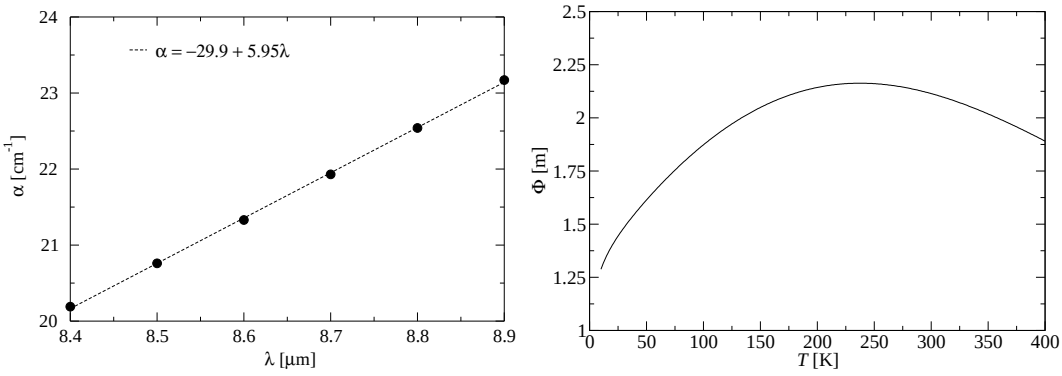

(a) n (b) α_{fc}

Figure 2.22: (a) Waveguide loss as a function of emission wavelength for the $\lambda \sim 9\mu$m GaAs-based QCL. The dashed line is a linear fit to the data. (b) Waveguide figure of merit as a function of temperature for the $\lambda \sim 9\mu$m GaAs-based QCL.

whatever the emission wavelength, the losses are in reasonable agreement with the experimentally measure ones and are in excellent agreement when $\lambda \sim 8.55\mu$m.

Waveguide figure of merit

Fig. 2.22 shows the figure of merit for the $\lambda \sim 9\mu$m GaAs-based QCL with a double plasmon-enhanced waveguide as a function of temperature. Comparing the data in Fig. 2.22 with the data for the InP-based waveguide with upper InAlAs and InGaAs layers in Fig. 2.18 it can be seen that the GaAs-based double plasmon-enhanced waveguide has poorer performance compared to its InP-based counterpart ($\sim 20\%$ lower Φ_{max}). Its maximum value also occurs at a different temperature than the InP-based waveguides due to the different mobility functions for these materials as shown in Fig. 2.11. As discussed previously, the confinement factor is found to be constant with respect to temperature and so the change in the figure of merit is purely down to the waveguide losses changing with temperature through the mobility.

2.4.3 Surface-plasmon waveguides

InP-based waveguides

As the emission wavelength increases above $\lambda \sim 15\mu$m, the required thickness of the cladding layers in plasmon-enhanced waveguides are at the limits of MBE growth techniques. Also, since free carrier absorption scales in the first approximation as λ^2 (Eqn. 2.29) optical losses are much larger at longer wavelengths. In order to circumvent these two issues, waveguides based on surface-plasmons have been developed [12, 13]. Surface-plasmons are TM EM modes confined to the interface between materials with opposite signs of dielectric constants. This is typical of a metal–semiconductor interface below the plasma frequency. As mentioned earlier, surface-plasmons had earlier been a hindrance to QCL operation in the MIR due to the increased losses associated with the surface-plasmon at the boundary between the upper cladding and top metal contact layers, this is not true however at longer wavelengths since the loss associated to the surface-plasmon is given as [14]

$$\alpha = \frac{4\pi n n_s^3}{k^3 \lambda} \tag{2.37}$$

where n and k are the real and imaginary parts of the complex refractive index of the metal and n_s is the refractive idnex of the semiconductor.

Fig. 2.23 shows a schematic diagram of the first QCL ($\lambda \sim 19\mu$m) to utilise a surface-plasmon waveguide [12]. In surface-plasmon waveguides, thin (~ 50

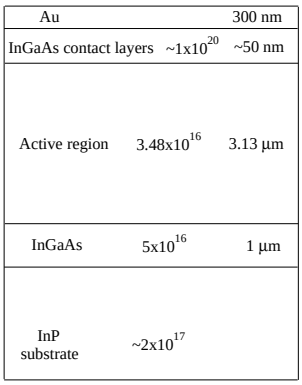

Figure 2.23: Schematic diagram of an InP-based surface-plasmon waveguide.

nm) highly doped semiconductor contact layers are grown on top of the active re-

gion/injector stack followed by a metal (usually gold) surface-plasmon carrying layer. The active region is preceded by a low-doped InGaAs layer on the low-doped InP substrate which acts a natural lower cladding layer.

Waveguide parameters

Fig. 2.23 shows the calculated fundamental TM mode profile of the first surface-plasmon QCL [12]. The loss and overlap are are calculated to be 85.3 cm^{-1} and 0.75

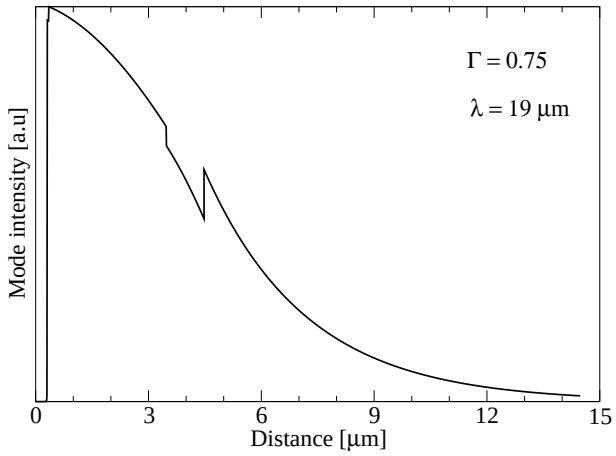

Figure 2.24: Mode profile of the fundamental TM mode of a $\lambda \sim 19\mu$m InP-based QCL with surface-plasmon waveguide showing the calculated confinement factor.

at 10 K respectively. These values are in comparison to the published values of 62 cm^{-1} and 0.81. In the literature, J_{th} is estimated to be 1.3 kA/cm^2 which is considerably smaller than the measured value of 4.5 kA/cm^2 with an underestimation of the waveguide losses a likely cause. It can be seen that by including the effect of temperature on the waveguide properties, the estimated waveguide parameters can be moved closer to what is measured experimentally.

As with all of the waveguides that include a metallic layer, there is uncertainty over the complex dielectric constant of the layer. In reality, if the dielectric constant is slightly different and the mode penetrates into this metal layer more than the calculations suggest, the waveguide losses will increase resulting in a higher value of J_{th}.

Waveguide figure-of-merit

Fig. 2.25 shows Φ for the surface-plasmon waveguide as a function of temperature. The maximum value of 1.6 occurs at 225 K, slightly less than that of the GaAs-based

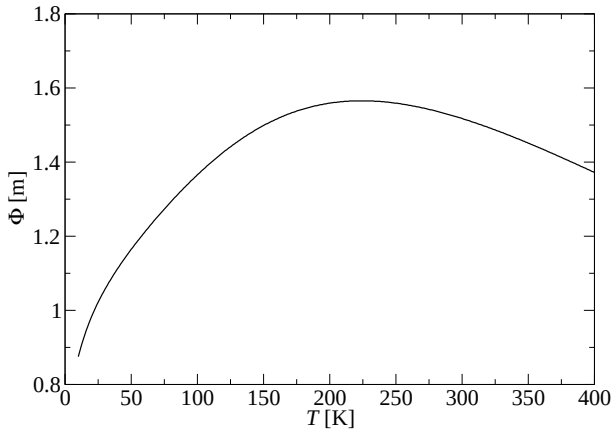

Figure 2.25: $\lambda \sim 19\mu$m InP-based surface-plasmon QCL waveguide figure of merit as a function of temperature.

double plasmon-enhanced waveguide at 9.4μm and the InP-based plasmon-enhanced waveguide at 8.4μm, even though the wavelength in this case is approximately double and therefore the losses can be expected to be of the order of four times larger. This fact highlights the usefulness of surface-plasmons for providing long wavelength optical confinement.

GaAs-based waveguides

Since the first surface-plasmon waveguides were reported in the InP-based material system, the low refractive index InP substrate is used for the lower cladding. However, as is the case with GaAs-based double plasmon-enhanced waveguides, the GaAs substrate has a higher refractive index than the core and cannot be used as lower cladding without being highly doped to reduce the refractive index of the layer. In order to prevent unacceptably high waveguide losses due to free-carrier absorption, especially at these longer wavelengths, the active region is separated from the highly doped substrate by a thick low-doped spacer layer. Fig. 2.26 shows a schematic diagram of a GaAs-based QCL with a surface-plasmon waveguide.

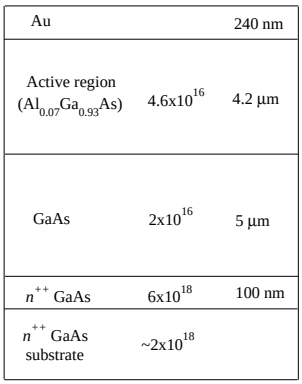

Figure 2.26: Schematic diagram of a GaAs-based surface-plasmon waveguide.

Waveguide parameters

Due to the close proximity of the emission wavelength to the Reststrahlen region of GaAs, the Drude-Lorentz model is used to calculate the the dielectric constant. Fig. 2.27 shows the calculated mode profile in the QCL with an effective aluminium fraction of $x = 0.07$ in the active region/injector stack[8] (in this particular QCL, the barriers were comprised of $Al_{0.35}Ga_{0.65}As$). The averaged value of doping density is 4.6×10^{16} cm^{-3}. Γ is calculated to be 0.78, in good agreement with the value of 0.80 in Ref. [15].

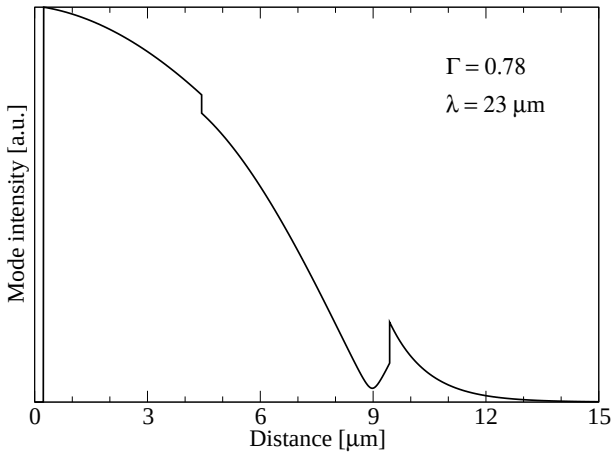

Figure 2.27: Mode profile of the fundamental TM mode of a $\lambda \sim 23\mu$m GaAs-based QCL with surface-plasmon waveguide showing the calculated confinement factor.

[8]It should be noted that at longer wavelengths, the active region of choice is either a chirped superlattice or bound-to-continuum design, which typically have thinner barriers and wider wells than 3QW active regions used in mid-infrared QCLs and hence a smaller effective Al fraction in the active region.

It is worth pointing out that n at this wavelength is 2.95, which is less than the values at shorter mid-infrared wavelengths (~ 3.2) and can be explained by the reduction of the $\epsilon(\omega)$ close to the Reststrahlen region (Fig. 2.12(a)) and results in larger mirror losses.

Waveguide figure-of-merit

Fig. 2.28 shows the figure-of-merit as a function of temperature. The figure of merit

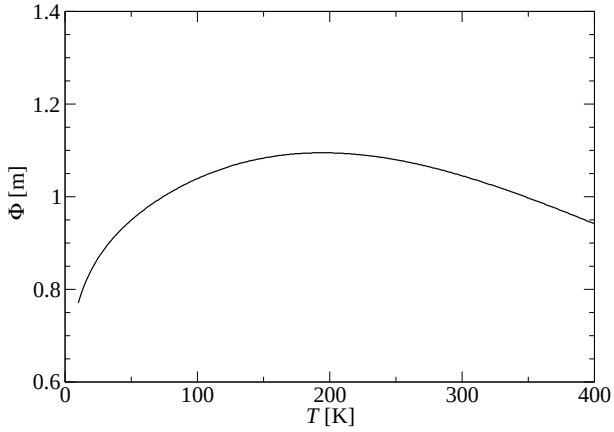

Figure 2.28: $\lambda \sim 23\mu$m GaAs-based surface-plasmon QCL waveguide figure of merit as a function of temperature.

is slightly lower than that of the InP-based waveguide. Since both optical waveguides have similar overlaps, the difference in figure of merit is due to the losses. As mentioned in previous cases, the increased losses in the GaAs-based devices can be associated with its longer wavelength.

2.5 THz QCL optical waveguide analysis

This section presents an investigation into the optical properties of the two types of THz QCL waveguides that are used.

2.5.1 Semi-insulating (double) surface-plasmon waveguides

The first THz QCL which had an emission frequency of 4.4 THz was reported in 2002 [16] and used a new type of optical waveguide. The much larger wavelength of the

THz QCL ($\lambda \sim 67\mu$m) compared to the previous largest ($\lambda \sim 23\mu$m) meant that a surface-plasmon waveguide would result in a unfeasibly small overlap of the optical mode with the device active region. The overlap could be increased by using a thicker action region but THz QCLs tend to have active region thicknesses of the order of 10 μm which is already a very demanding task in terms of growth. Therefore a semi-insulating (or double) surface-plasmon waveguide (SISP) was used. A schematic diagram is shown in Fig. 2.29. Optical confinement is achieved in SISP waveguides

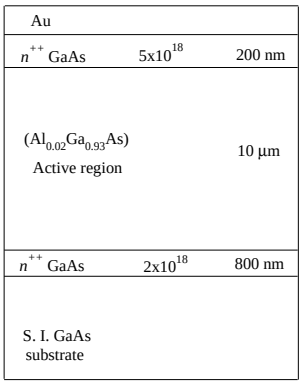

Figure 2.29: Schematic diagram of a semi-insulating surface-plasmon waveguide.

through surface-plasmons on each side of the active region merging to form a single mode. On the upper side, a surface-plasmon is formed in the same way as for the single surface-plasmon waveguides in the MIR, between the semiconductor active region and metallic top contact. The lower surface plasmon is pinned to the interface between the thin highly-doped layer (which has shifted it's plasma wavelength close to that of the mode) and the active region. The calculated mode profile of the first THz QCL is shown below. The confinement factor is found to be 0.48, in excellent agreement with the published value [16], although the calculated losses of 25 cm^{-1} are slightly higher than the reported value of 16 cm^{-1}. This is likely due to proximity of the Reststrahlen region and the uncertainty over the optical properties of the gold layer. It can be seen that a significant portion of the optical mode resides within the substrate and therefore the semi-insulating substrate is used to minimise free-carrier losses. This means that in the ridge waveguide structure, the thin highly-doped layer is used for electrical contacting. The optical mode also overlaps with this highly-doped layer and this

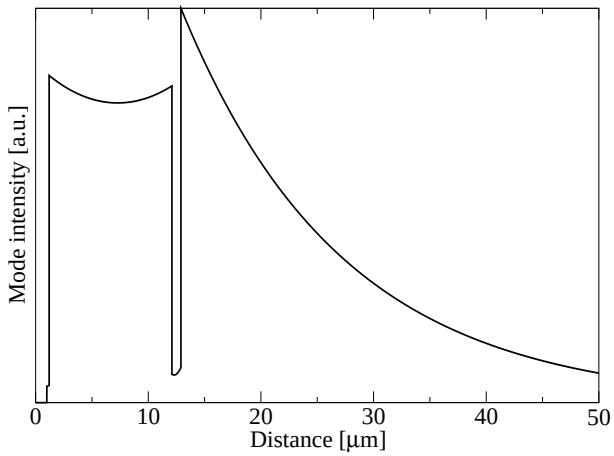

Figure 2.30: Mode profile of the fundamental TM mode of a 4.4 THz QCL with surface-plasmon waveguide showing the calculated confinement factor and effective refractive index of the mode.

is the reason why it is made thin; again to reduce the free-carrier losses.

Fig. 2.31 shows the overlap factor and waveguide loss as a function of frequency for a SISP waveguide. It can be seen that at low frequencies, Γ decreases to very small

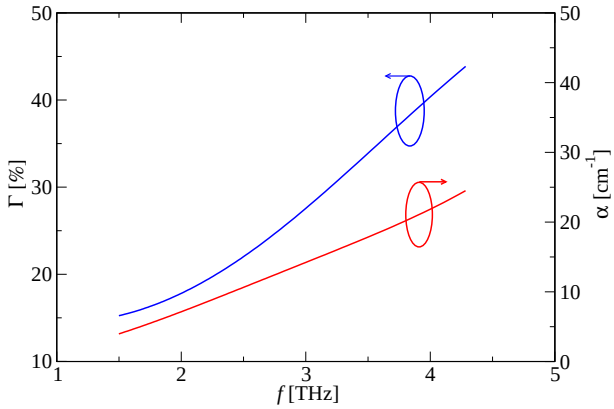

Figure 2.31: Overlap factor and waveguide loss as a function of frequency in a semi-insulating surface-plasmon THz optical waveguide.

values ($< 20\%$ at 2 THz). This will have serious implications on the modal gain, even though there is a concomitant decrease in the waveguide losses (since the mirror loss will remain largely unchanged).

2.5.2 Double-metal waveguides

Double-metal (or metal-metal) waveguides are the other type of optical waveguide that is used in THz QCLs [17]. In principle they are basically the same as microstrip transmission lines that are commonly used for waveguiding purposes in microwave and millimetre-wave circuits. A schematic diagram is shown in Fig. 2.32. The semi-

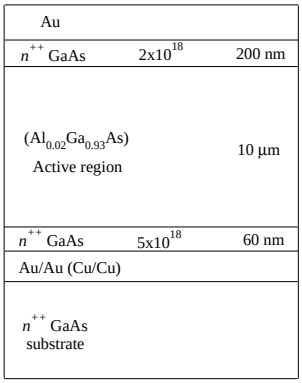

Figure 2.32: Schematic diagram of a double-metal waveguide.

conductor active region is surrounded on both sides by metallic layers which completely confine the optical mode between them, achieving overlap factors close to unity. The fundamental TM mode of a metal-metal (MM) waveguide used for a 3 THz QCL ($\lambda \sim 100\mu$m) is shown in Fig. 2.33. As with THz QCLs with SISP waveg-

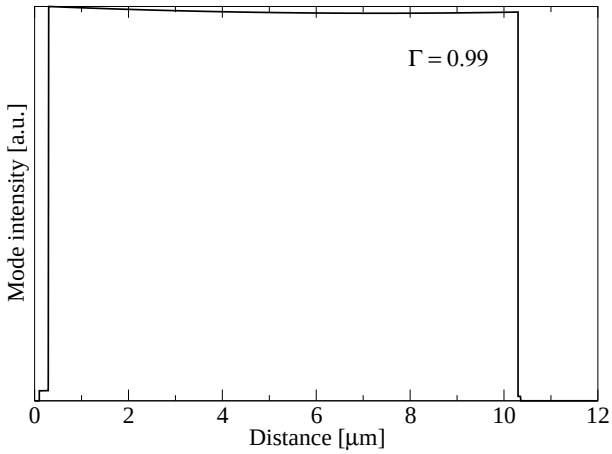

Figure 2.33: Mode profile of the fundamental TM mode of a 3 THz ($\lambda \sim 100\mu$m) QCL with double metal waveguide.

uides, the active region tends to be of the order of 10 μm thick in QCLs with MM

waveguides and losses of the same order meaning the figure of merit of MM waveguides is inherently better due to $\Gamma \approx 1$. However, this does come at the disadvantage of a much more complex fabrication process. The QCL active region is grown on a substrate and capped with a metal layer, which is then bonded upside down onto the n^+ substrate (which is also covered in metal) using a thermo-compression technique [17]. The metal that is commonly used for the bonding layer is gold, although it has been shown that the QCL temperature performance can be improved through the use of a copper-copper bonding layer due to its higher thermal conductivity [18]. This will be discussed in more detail in Chapter 5.

Gold is the standard metal layer that is used on top of the active region, although it is possible to use other metals such as silver and copper to improve performance [19, 20]. Fig. 2.34 shows the optical losses in a MM waveguide as a function of frequency for different top contact metals. The waveguide is assumed to be 'empty' i.e. the active region is assumed to be undoped. The optical properties of each metal are listed in Table 2.3. In all cases $\Gamma \approx 1$ and the bonding layer is assumed to be gold. It can

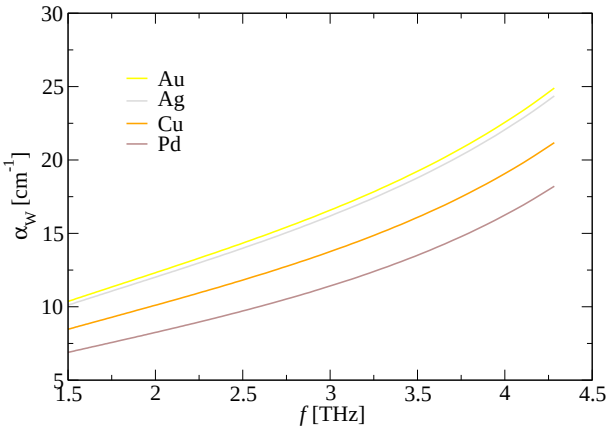

Figure 2.34: Optical losses in a MM waveguide as a function of frequency for different metals; gold, silver, copper and palladium.

be seen that in all cases, the losses of the empty waveguide increase with increasing frequency (i.e. decreasing wavelength) in contrast to what is predicted by Eqn. 2.29 for wavelengths below the Reststrahlen region. For all frequencies, gold has the highest losses with palladium having the lowest. From Table 2.3 it can be seen that all metals have similar plasma frequencies and the reason for the different losses is due to the

plasma damping frequency ω_a through Eqn. 2.28 which shows that the free-carrier loss is proportional to ω_a and this is lowest in palladium. These results suggest that by using palladium as the top contact metal will result in lower waveguide losses and hence lower threshold current densities leading to increased operating temperatures. Indeed, there has been recent reports of a THz QCLs utilising a copper MM waveguide operating up to 178 K in pulsed mode, a record for THz QCLs [20].

2.6 Conclusions

The development of a one-dimensional optical waveguide solver has been presented. The wave equation has been solved for an arbitrary multilayer structure using a transfer-matrix method in order to obtain the complex propagation constant and waveguide parameters. The complex refractive indexes were calculated using a Drude-Lorentz model. This model takes into account both plasma and phonon contributions to the semiconductor refractive indices. It was shown how the extinction coefficient is strongly dependent upon the electron mobility and a Caughey-Thomas-like mobility model was introduced and used to calculate the temperature dependence of the semiconductor optical properties

Optical waveguide analysis was then performed on the different waveguide schemes that have been adopted for different wavelength ranges. In particular, it was shown that by including the temperature dependent material properties, better agreement with experimentally measured values of threshold current density can be achieved. For the case of THz QCLs, metal–metal optical waveguides were found to offer the best performance as the emission wavelength increases due to the near unity mode overlap factor. It was also found that the use of palladium as the plasmon-carrying layer could offer the possibility of lower waveguide losses and lead to higher maximum operating temperatures.

References

[1] C. Becker and C. Sirtori, "Lateral current spreading in unipolar semiconductor lasers," *J. Appl. Phys.*, vol. 90, p. 1688, 2001.

[2] S. Kohen, B. S. Williams, and Q. Hu, "Electromagnetic modeling of terahertz quantum cascade laser waveguides and resonators," *J. Appl. Phys.*, vol. 97, no. 053106, 2005.

[3] E. Anemogiannis, E. N. Glytsis, and T. K. Gaylord, "Determination of guided and leaky modes in lossless and lossy planar multilayer optical waveguides: Reflection pole method and wavevector density method," *IEEE J. Light. Technol.*, vol. 17, pp. 929–941, May 1999.

[4] S. Adachi, *GaAs and Related Materials: Bulk Semiconducting and Superlattice Properties*. World Scientific, 1994.

[5] E. D. Palik, ed., *Handbook of Optical Constants of Solids*, vol. 1/2. New York: Academic, 1985/1991.

[6] M. Sotoodeh, A. Khalid, and A. Rezazadeh, "Empirical low-field mobility model for III-V compounds applicable in device simulation codes," *J. Appl. Phys.*, vol. 87, no. 6, p. 2890, 2000.

[7] M. A. Ordal, R. J. Bell, R. W. Alexander Jr., L. L. Long, and M. R. Querry, "Optical properties of fourteen metals in the infrared and far infrared: Al, Co, Cu, Au, Fe, Pb, Mo, Ni, Pd, Pt, Ag, Ti, V, and W," *Appl. Opt.*, vol. 24, p. 4493, December 1985.

[8] A. D. Rakic, A. B. Djurisic, J. M. Elazar, and M. L. Majewski, "Optical properties

of metallic films for vertical-cavity optoelectronic devices," *Appl. Opt.*, vol. 37, no. 22, pp. 5271–5283, 1998.

[9] C. Sirtori, J. Faist, F. Capasso, A. L. Hutchinson, D. L. Sivco, and A. Y. Cho, "Quantum cascade laser with plasmon-enhanced waveguide operating at 8.4μm wavelength," *Appl. Phys. Lett.*, vol. 66, pp. 3242–3244, June 1995.

[10] C. Sirtori, P. Kruck, S. Barbieri, P. Collot, J. Nagle, M. Beck, J. Faist, and U. Oesterle, "GaAs/Al_xGa_{1-x}As quantum cascade lasers," *Appl. Phys. Lett.*, 1998.

[11] C. Sirtori, P. Kruck, S. Barbieri, H. Page, and J. Nagle, "Low-loss Al-free waveguides for unipolar semiconductor lasers," *Appl. Phys. Lett.*, vol. 75, no. 25, pp. 3911–3913, 1999.

[12] A. Tredicucci, F. Capasso, C. Gmachl, M. C. Wanke, D. L. Sivco, A. L. Hutchinson, S. G. Chu, and A. Y. Cho, "Surface plasmon quantum cascade lasers at $\lambda \sim 19\mu$m," *Appl. Phys. Lett.*, vol. 77, no. 15, p. 2286, 2000.

[13] R. Colombelli, F. Capasso, C. Gmachl, A. Tredicucci, A. L. Hutchinson, D. L. Sivco, M. C. Wanke, A. M. Sergent, and A. Y. Cho, "Far infrared surface plasmon quantum cascade lasers at 21.5 μm and 24 μm wavelengths," *Appl. Phys. Lett.*, vol. 78, no. 18, p. 2620, 2001.

[14] C. Sirtori, C. Gmachl, F. Capasso, J. Faist, D. L. Sivco, A. L. Hutchinson, and A. Y. Cho, "Long-wavelength ($\lambda \approx 8-11.5\mu$m) semiconductor lasers with waveguides based on surface plasmons," *Opt. Lett.*, vol. 23, no. 17, pp. 1366–1368, 1998.

[15] J. Ulrich, J. Kreutter, W. Schrenk, G. Strasser, and K. Unterrainer, "Long wavelength (15 and 23μm) GaAs/AlGaAs quantum cascade lasers," *Appl. Phys. Lett.*, vol. 80, pp. 3691–3693, May 2002.

[16] R. Köhler, A. Tredicucci, F. Beltram, H. E. Beere, E. H. Linfield, A. G. Davies, D. A. Ritchie, R. C. Iotti, and F. Rossi, "Terahertz semiconductor heterostructure laser," *Nature*, vol. 417, no. 156, pp. 156–159, 2002.

[17] B. S. Williams, S. Kumar, H. Callebaut, and Q. Hu, "Terahertz quantum-cascade

laser at $\lambda \approx 100\mu$m using metal waveguide for mode confinement," *Appl. Phys. Lett.*, vol. 83, no. 11, pp. 2124–2126, 2003.

[18] M. S. Vitiello, V. Spagnolo, G. Scamarcio, J. Alton, S. Barbieri, C. Worrall, H. E. Beere, D. A. Ritchie, and C. Sirtori, "Thermal properties of THz quantum cascade lasers based on different optical waveguide configurations," *Appl. Phys. Lett.*, vol. 89, no. 021111, pp. 1–3, 2006.

[19] M. Bahriz, V. Moreau, J. Palomo, R. Colombelli, D. A. Austin, J. W. Cockburn, L. R. Wilson, A. B. Krysa, and J. S. Roberts, "Room-temperature operation of $\lambda \approx 7.5\mu$m surface-plasmon quantum cascade lasers," *Appl. Phys. Lett.*, vol. 88, no. 181103, pp. 1–3, 2006.

[20] S. P. Khanna, M. A. Belkin, J. A. Fan, S. Harmoz, M. Lachab, F. Capasso, A. G. Davies, and E. H. Linfield, "Terahertz quantum cascade lasers operating up to 178 K with copper metal-metal waveguides." accepted for publication in Optics Express.

Chapter 3

Thermal properties of quantum cascade lasers

3.1 Introduction

QCLs generally suffer from high threshold currents and voltages [1] and therefore require large amounts of input electrical power. Due to the relatively low wall-plug efficiencies, the vast majority of the input power is dissipated in the device active region as heat, causing its temperature to rise considerably. The active region temperature is a critical parameter which strongly affects the operation of QCLs through the temperature dependence of the scattering rates. It is known that there are two main mechanisms which affect temperature performance which were discussed briefly in Chapter 1: thermal backfilling and electron leakage. Thermal backfilling is the phenomenon where electrons in the injector gain sufficient thermal energy to 'climb back up the energy ladder' and re-populate the lower laser level. Electron leakage is a mechanism which affects the upper laser level; at sufficiently high temperatures, electrons gain enough energy to escape from the upper laser level into the continuum-like states. So, following the same nomenclature as in Sec. 1.2.1, thermal backfilling increases the population of the $n = 2$ state (lower laser level) and electron leakage reduces the population of the $n = 3$ state (upper laser level) resulting in a decrease of the population inversion ($n_3 - n_2$) and hence the modal gain. These effects are most strongly felt under cw operation, since there is a constant supply of power (and therefore heat) to

the active region. Therefore QCLs operate at much higher temperatures under pulsed mode operation, where the input power is supplied in short bursts and therefore the active region has a chance to cool in between pulses.

In order to improve the performance of QCLs and achieve high temperature operation, knowledge of the thermal dynamics inside the device are mandatory. The temperature of the active region (T_{AR}) can be estimated through the simple relation

$$T_{\mathrm{AR}} = T_{\mathrm{H}} + PR_{\mathrm{TH}} = T_{\mathrm{H}} + VIR_{\mathrm{TH}} \tag{3.1}$$

where T_{H} is the heat sink temperature, P is the input electrical power at threshold, V and I are the voltage and current at threshold respectively and R_{TH} is defined as the device thermal resistance. Assuming J_{th} ($= I/A$ where A is the device area) can be expressed as the phenomenological relation

$$J_{\mathrm{th}} = J_0 \exp(T_{\mathrm{AR}}/T_0) \tag{3.2}$$

where T_0 is the characteristic temperature, the active region temperature can be recast into the form

$$T_{\mathrm{AR}} = T_0 \ln(J_{\mathrm{th}}/J_0). \tag{3.3}$$

Inserting this into Eqn. 3.1 and re-arranging gives

$$T_{\mathrm{H}} = T_0 \ln(J_{\mathrm{th}}/J_0) - VJ_{\mathrm{th}}R_{\mathrm{TH}}A. \tag{3.4}$$

Differentiating with respect to J_{th} and setting the result equal to zero gives an expression for J_{th} at the maximum heat sink temperature $T_{\mathrm{H,max}}$

$$\frac{dT_{\mathrm{H}}}{dJ_{\mathrm{th}}} = \frac{T_0}{J_{\mathrm{th}}} - VJ_{\mathrm{th}}R_{\mathrm{TH}}A = 0 \tag{3.5}$$

$$J_{\mathrm{th}} = \frac{T_0}{VR_{\mathrm{th}}A}. \tag{3.6}$$

Inserting Eqn. 3.6 into Eqn. 3.4 gives

$$\begin{aligned} T_{\mathrm{H,max}} =& T_0 \ln\left(\frac{T_0}{J_0 V R_{\mathrm{TH}} A}\right) - T_0 \\ =& T_0 \left[\ln\left(\frac{T_0}{J_0 V R_{\mathrm{TH}} A}\right) - 1\right]. \end{aligned} \tag{3.7}$$

Inspecting Eqn. 3.7 it can be seen that in order to achieve a high value of $T_{\mathrm{H,max}}$, a large value of T_0 and a small value of R_{th} are necessary.

As already shown in Eqn. 1.22, the threshold current density can be expressed as

$$J_{\text{th}} = \frac{\alpha_m + \alpha_{wg}}{g\Gamma}. \tag{3.8}$$

Inserting this into Eqn. 3.1 and replacing V by FN_pL_p, where F is the applied electric field, N_p is the number of periods and L_p is the length of one period gives an expression for the active region temperature[1]

$$T_{\text{AR}} = T_{\text{sink}} + \frac{R_{\text{TH}}AFN_pL_p(\alpha_m + \alpha_{wg})}{g\Gamma}. \tag{3.9}$$

For the case of a set heat sink temperature, it is clear from the above analysis the device active region temperature can be reduced in a number of ways:

- **By reducing the input electrical power**. This can be done through the use of pulsed mode operation at low duty cycles. Typical pulse widths are of the order of 100 ns with pulse repetition frequencies in the range 1–10 kHz. Although QCLs operating in pulsed mode have higher maximum operating temperatures, cw operation is particularly useful for gas-sensing applications in the MIR while in the THz range, cw QCLs could form local oscillators in heterodyne receiver systems used in radio astronomy. The required input power can also be reduced by shrinking the dimensions of the active region. If the number of periods N_p is reduced then the value of electric field F that is required to bring the subbands into correct alignment can be achieved with a smaller voltage. The electrical current can be reduced by decreasing the area of the ridge although doing this by decreasing the length of the cavity will result in smaller gain and increased mirror losses (Eqn. 2.7). Reducing the active region dimensions results in a smaller emitting volume and therefore lower output powers and so care must be made to achieve a balance between temperature and power performance.

- **By improving the waveguide design** to increase the overlap factor Γ and decrease the total losses α_{W} and α_{M}.

[1]It should be noted that this simplified expression ignores the output photon energy and therefore overestimates the dissipated electrical power. However, this does not alter the effect of each parameter on the device heating.

- **By optimising the active region design to increase** g. As shown in Equation 1.12 the gain coefficient is proportional to the population inversion. As mentioned before, at high temperatures electron leakage and thermal backfilling act to reduce the population inversion. Electron leakage can be reduced by using material systems with large conduction band offsets and thermal backfilling reduced by increasing the energy gap between the lower laser level and the injector states. This can be achieved through use of a double-LO phonon resonance design as was discussed in Sec. 1.3.2.

- **By using advanced thermal management techniques to reduce** $R_{\mathbf{th}}$**.** These include:

  - **Epilayer-down mounting**[2]. This technique involves bonding a planarised structure 'upside–down' directly onto the heat sink. This distance between the heat-generating active region and the heat sink is reduced, thus increasing the efficiency of heat diffusion from the device active region.

  - **Buried Heterostructures (BH)** [3]. In typical ridge waveguides, there is no lateral heat channel for heat to escape from the active region. Laterally overgrowing a ridge waveguide with i-InP opens up a heat escape channel and increases the efficiency of heat removal from the active region. This approach combined with epilayer-down bonding allowed the first demonstration of room-temperature cw QCL emission [4].

  - **Gold plating** around the laser ridge [5] to act as a pseudo-heat sink. Thick layers (5–20 μm) of gold are electroplated on top of and to the side of the laser ridge to help remove the waste heat. This technique is similar in principle to epilayer-down mounting but requires less complicated processing. Despite this, above room-temperature cw emission has been achieved using this technique [6].

  - **A combination of two or more of the above thermal management techniques**

This chapter presents the development of a QCL thermal model which is used to

investigate the thermal properties of different QCL structures under a range of operating conditions in both pulsed- and continuous-wave mode.

3.2 The heat equation

The thermal model is based upon Fourier's law of heat conduction

$$\mathbf{q} = -\kappa \nabla T \tag{3.10}$$

where $\mathbf{q}$ is the heat flux vector, κ is the thermal conductivity of the material and ∇T is the temperature gradient. The negative sign indicates heat flows from a region of higher temperature to a region of lower temperature. The conservation of energy gives

$$\nabla \cdot \mathbf{q} = Q - \frac{\partial E}{\partial t} \tag{3.11}$$

where $\nabla \cdot \mathbf{q}$ the net heat conducted out of the material, Q is the internally generated power per unit volume and $\partial E/\partial t$ is the change in stored internal energy density in the material. The change in stored internal energy desnity can also be expressed as

$$\frac{\partial E}{\partial t} = \rho c \frac{\partial T}{\partial t} \tag{3.12}$$

where ρ is the material density and c is the specific heat capacity of the material. By eliminating $\mathbf{q}$ between Eqns. 3.10 and 3.11 and inserting the above expression for the change in internal energy one arrives at the well known heat equation

$$\rho c \frac{\partial T}{\partial t} = \nabla \cdot [\kappa \nabla T] + Q. \tag{3.13}$$

which must be solved in order to calculate the temperature distribution inside a QCL structure.

3.3 Material properties

3.3.1 Thermal conductivity

In order to obtain accurate results from the solution of the heat equation, it is important to include the effects of temperature on the material parameters, particularly the thermal conductivity.

Semiconductors

The lattice thermal conductivity of semiconductors results from interactions between phonons and from scattering of phonons at defects in the semiconductor crystal lattice. At absolute zero the thermal conductivity is zero and rises almost exponentially to a maximum around 10 K before decreasing until the melting point.

The electronic contribution (from free electrons) to the thermal conductivity was estimated using the Weidmann-Franz law and found to be negligible compared to the lattice thermal conductivity. It is therefore ignored in this work.

Table 3.1 lists the temperature dependent thermal conductivities for the important III-V (undoped) semiconductors.

Material	Thermal conductivity [W m^{-1} K^{-1}]	
GaAs	$74500T^{-1.30}$	[7]
AlAs	$225270T^{-1.37}$	[8]
InP	$289000T^{-1.45}$	[9]
InGaAs	$23 - 9.30 \times 10^{-2}T + 1.06 \times 10^{-4}T^2$	[2]
InAlAs	$20.5 - 8.40 \times 10^{-2}T + 0.95 \times 10^{-4}T^2$	[10]

Table 3.1: Temperature-dependent semiconductor thermal conductivities.

For the case of $Al_xGa_{1-x}As$, Abele's interpolation method (Appendix C) is used in order to obtain the thermal conductivity from the thermal conductivities of the corresponding binaries (the bowing parameter C_{AB} = 3.33 W/m K [7]). It is known that each decade of doping reduces κ by ~8% starting from 10^{15} cm^{-3} due to the influence of the ionised impurities on the phonon transport [9] and the values of thermal conductivity in Table 3.1 are scaled accordingly.

Anisotropic thermal conductivity

Eqn. 3.13 is valid for isotropic materials. In the case of the multi-layered superlattice-like QCL active regions, the thermal conductivity is anisotropic. Therefore κ is re-

placed in Eqn. 3.13 with a thermal conductivity tensor i.e. for the case of a 3D-problem

$$\rho c \frac{\partial T}{\partial t} = \nabla \cdot \left(\begin{bmatrix} \kappa_x & 0 & 0 \\ 0 & \kappa_y & 0 \\ 0 & 0 & \kappa_z \end{bmatrix} \cdot \nabla T \right) + Q \tag{3.14}$$

Due to its superlattice-like nature, the thermal conductivity of the QCL active region is strongly-anisotropic and as a result, both the in-plane ($\kappa_{\parallel}$) and cross-plane ($\kappa_{\perp}$) thermal conductivities are significantly reduced compared to the bulk values of the constituent materials. Since the layer widths are comparable to or less than the phonon mean free path, the phonon scattering rate at the interfaces between layers increases, hindering the phonon transport [11, 12]. The partially diffuse scattering of phonons at the interfaces can explain the reduction in $\kappa_{\parallel}$ [13], while the stronger reduction in $\kappa_{\perp}$ is caused by the multiple reflections of phonons at the many interfaces [12]. Furthermore, THz QCLs particularly suffer compared to MIR devices since they generally contain more active region periods resulting in a larger number of interfaces and a higher value of thermal resistance (R_{TH}). It has been found that the interface contribution to the overall thermal resistivity of the THz QCLs can be as high as 97% [14].

The reduction in $\kappa_{\perp}$ has been measured experimentally in SiGe/Si and GaAs /AlAs superlattices [12, 15]. However, no experimental measurements of the thermal conductivity of QCL active regions have been published to date, but values of the cross-plane conductivity have been inferred indirectly by fitting the results of theoretical thermal models to experimentally measured temperature profiles and found to be over an order of magnitude smaller than the corresponding bulk alloy (see for example Refs. [16] and [17] and Chapter 5). It has been estimated that $\kappa_{\parallel}$ is roughly equal to 75 % of the value of its bulk constituents and this is included in this work [16].

Insulators and metals

Temperature dependent thermal conductivities of relevant non-semiconductor materials are listed in Table 3.2.

Material	Thermal conductivity [W m^{-1} K^{-1}]	
Copper	$349 + 14710/T$	[16]
Gold	$337 - T/15.15$	[16]
Indium	$93.9 - 6.96 \times 10^{-2}T + 9.86 \times 10^{-5}T^2$	[16]
SiO_2	$0.0974 + 5.38 \times 10^{-3}T - 4.69 \times 10^{-6}T^2$	[18]
Diamond	2000	[19]

Table 3.2: Temperature-dependent thermal conductivities of the relevant metals and insulators.

3.3.2 Specific heat capacity

The semiconductor specific heat capacities are calculated using the Debye specific heat equation

$$c = 9N_{AV}k_B\left[\frac{T}{\Theta_D}\right]^3\int_0^{\Theta_D/T}\frac{x^4e^x}{(e^x-1)^2}dx \tag{3.15}$$

where N_{AV} is Avogadro's number, k_B is the Boltzmann constant and Θ_D is the Debye temperature.

Material	Θ_D [K]	
InP	425	[20]
InGaAs	330	[20]

Table 3.3: Debye temperatures of the relevant semiconductors

Due to a lack of experimental data, the specific heat capacities of the other materials are taken to be constant and room-temperature values are used. These are listed in Table 3.4

3.3.3 Density

Over the temperature range of interest, the material densities remain largely unchanged with temperature and are therefore taken to be constant. Table 3.5 lists the room temperature densities of the relevant materials.

Material	c [J kg^{-1} K^{-1}]	
Copper	385	[20]
Gold	128	[20]
Indium	233	[20]
SiO_2	160	[20]
Diamond	520	[19]

Table 3.4: Material specific heat capacities (300 K).

Material	ρ [kg m^{-3}]	
InP	4480	[20]
InGaAs	5520	[20]
Copper	8960	[20]
Gold	19300	[20]
Indium	7310	[20]
SiO_2	3180	[20]
Diamond	35150	[19]

Table 3.5: Material densities (300 K).

3.4 Solution of the heat equation

The complex geometry of a QCL makes a numerical solution of the heat equation the most favourable option and in this work, finite-difference methods are used due to their relative simplicity compared to more complex finite-element methods.

3.4.1 Finite-difference approximation to the heat equation

In order to solve the heat equation using finite-difference methods[2], the time domain is discretised into finite steps and the spatial domain where the solution is to be found is split into smaller regular-sized subdomains (i.e. squares/rectangles in 2D, cuboids

[2] more information on finite-differences is given in Appendix D.

in 3D) which are commonly known as cells or elements. The collection of the cells is known as the computational mesh or grid. The discretised heat equation is then solved inside each of these cells with appropriate continuity of the solution across the interfaces and subject to relevant boundary conditions at the edges of the grid.

To solve the heat equation (for example in 2D), at each of the grid nodes a *five-point stencil* is used which connects the node with each of its four 'nearest neighbours' in the grid[3]. Fig. 3.1 shows the five-point stencil that is used to solve the heat equation.

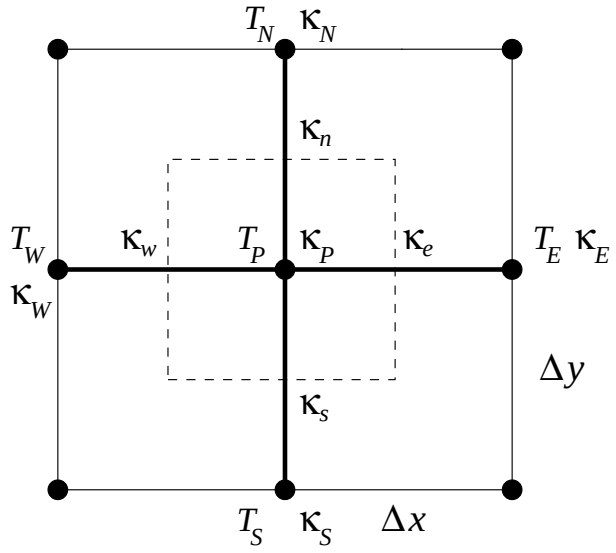

Figure 3.1: Five-point stencil used in the model. Interface values of κ are denoted by the lower-case subscripts while nodal values have upper-case subscripts.

Expanding Eqn. 3.13 and including the anisotropic thermal conductivity gives

$$\rho c \frac{\partial T}{\partial t} = \frac{\partial}{\partial x}\left(\kappa_x \frac{\partial T}{\partial x}\right) + \frac{\partial}{\partial y}\left(\kappa_y \frac{\partial T}{\partial y}\right) + Q. \tag{3.16}$$

The time derivative is replaced using a forward finite-difference approximation and the space derivatives are replaced with central finite-difference approximations (this

[3]It is simple to extend this concept to 3D and a seven-point stencil is used to connect the node to its six nearest neighbours.

is known as 'forward time central space' - FTCS).

$$\begin{aligned}\rho_{i,j}c_{i,j}\left(\frac{T_{i,j}^{m+1}-T_{i,j}^{m}}{\Delta t}\right) &= \frac{\kappa_{i+\frac{1}{2},j}(T_{i+1,j}^{m}-T_{i,j}^{m})}{\Delta x^2} - \frac{\kappa_{i-\frac{1}{2},j}(T_{i,j}^{m}-T_{i-1,j}^{m})}{\Delta x^2} \\ &+ \frac{\kappa_{i,j+\frac{1}{2}}(T_{i,j+1}^{m}-T_{i,j}^{m})}{\Delta y^2} - \frac{\kappa_{i,j-\frac{1}{2}}(T_{i,j}^{m}-T_{i,j-1}^{m})}{\Delta y^2} \\ &+ Q_{i,j}^{m}.\end{aligned} \tag{3.17}$$

In order to make the notation easier to follow, it is common to replace the co-ordinates in terms of i, j, k with N, S, E, W, F, B, P to represent the nodes to the north, south, east, west, in front and behind the current node P

$$\begin{aligned}\rho_P c_P\left(\frac{T_P^{m+1}-T_P^{m}}{\Delta t}\right) &= \frac{\kappa_e(T_E^{m}-T_P^{m})}{\Delta x^2} - \frac{\kappa_w(T_P^{m}-T_W^{m})}{\Delta x^2} \\ &+ \frac{\kappa_n(T_N^{m}-T_P^{m})}{\Delta y^2} - \frac{\kappa_s(T_P^{m}-T_S^{m})}{\Delta y^2} \\ &+ Q_P^{m}.\end{aligned} \tag{3.18}$$

Interface values of k

From Eqn. 3.17 it can be seen that the values of κ are taken at the boundary between the nodes. Instead of using a simple mean value, a harmonic mean is used for the interface values such that the heat flux is continuous at the boundaries and gives the correct value if κ tends to zero. For the situation depicted in Fig. 3.1, continuity of the flux requires

$$\kappa_e \frac{\partial T}{\partial x}\Big|_{x_e} = \kappa_P \frac{\partial T}{\partial x}\Big|_{x_P} = \kappa_E \frac{\partial T}{\partial x}\Big|_{x_E}. \tag{3.19}$$

Applying finite difference approximations to the above derivatives gives

$$\kappa_e \frac{T_E - T_P}{\Delta x} = \kappa_P \frac{T_e - T_P}{\Delta x/2} \tag{3.20}$$

$$\kappa_e \frac{T_E - T_P}{\Delta x} = \kappa_E \frac{T_E - T_e}{\Delta x/2} \tag{3.21}$$

where T_e is the temperature at the interface. From the above equations

$$T_e - T_P = \kappa_e \frac{T_E - T_P}{2\kappa_P} \tag{3.22}$$

$$T_E - T_e = \kappa_e \frac{T_E - T_P}{2\kappa_E}. \tag{3.23}$$

Adding the two equations above gives

$$T_E - T_P = \kappa_e \frac{T_E - T_P}{2\kappa_P} + \kappa_e \frac{T_E - T_P}{2\kappa_E} \tag{3.24}$$

which can be rearranged to give the value of k at the boundary which ensures a continuous heat flux across the interface

$$\kappa_e = 2\frac{\kappa_P \kappa_E}{\kappa_E + \kappa_P}. \tag{3.25}$$

The same argument can be used to derive (or write through direct analogy) similar expressions for κ_w,κ_n and κ_s.

Boundary conditions

There are several types of boundary condition that can be applied to the heat equation

$$\text{Isothermal (Dirichlet) :} \qquad T = f_i(x, y, t) \tag{3.26}$$

$$\text{Insulated/Symmetrical (Neumann) :} \qquad \frac{\partial T}{\partial n_i} = 0 \tag{3.27}$$

$$\text{Convective (Robin) :} \qquad k\frac{\partial T}{\partial n_i} = h_i(T - T_a) \tag{3.28}$$

where f_i is an arbitrary function, n_i is the outward direction normal to the surface in direction i, h_i is the heat transfer coefficient and T_a is the ambient temperature. A Dirichlet boundary condition is applied to the surface of the device which is held in contact with the heat sink and kept at a fixed temperature. In most cases, Neumann boundary conditions are appropriate for the other surfaces of the device since QCLs are commonly measured under vacuum conditions and is hence the heat transfer process is adiabatic (i.e. no heat flow out of the device).

The Neumann boundary condition is also very useful as it can be applied to any plane of symmetry in the structure to reduce the size of the computational grid (i.e. number of nodes) by a factor of two and hence make dramatic savings on the CPU run time and memory requirements.

The above equations define the full set of tools required in order to solve the heat equation using finite-differences. However, there are different approaches to solve the finite-difference heat equation depending on whether the solution is to be found in the time-domain (i.e. the QCL under pulsed operating conditions) or in steady-state (continuous-wave).

3.4.2 Steady-state thermal analysis

In steady-state the left-hand side of Eqn. 3.18 is equal to zero and as the solution is independent of time, hence the superscripts m can be dropped.

$$\frac{\kappa_e(T_E - T_P)}{\Delta x^2} - \frac{\kappa_w(T_P - T_W)}{\Delta x^2} + \frac{\kappa_n(T_N - T_P)}{\Delta y^2} - \frac{\kappa_s(T_P - T_S)}{\Delta y^2} = -Q_P. \tag{3.29}$$

Re-arranging to make T_P the subject gives

$$T_P = W_x(\kappa_w T_W + \kappa_e T_E) + W_y(\kappa_n T_N + \kappa_s T_S) + W_q Q_p \tag{3.30}$$

where

$$W_x = \frac{\Delta y^2}{(\kappa_w + \kappa_e)\Delta x^2 + (\kappa_n + \kappa_s)\Delta y^2} \tag{3.31}$$

$$W_y = \frac{\Delta x^2}{(\kappa_w + \kappa_e)\Delta x^2 + (\kappa_n + \kappa_s)\Delta y^2} \tag{3.32}$$

$$W_q = \frac{\Delta x^2 \Delta y^2}{(\kappa_w + \kappa_e)\Delta x^2 + (\kappa_n + \kappa_s)\Delta y^2} \tag{3.33}$$

are the weighting functions. Inspecting Eqn. 3.30 it can be seen that the nodal temperature is the weighted average of its four nearest neighbours temperatures (with the weights dependent upon the distance to its neighbours and the thermal conductivity of the points in the five point stencil) plus a contribution to its temperature from any heat source at the node. It is worth noting that in the absence of a heat source ($Q_P = 0$) in a homogeneous material (constant k) on a square grid ($\Delta x = \Delta y$) that the equation reduces to

$$T_P = \frac{T_N + T_S + T_E + T_W}{4} \tag{3.34}$$

and T_P is simply equal to the mean temperature of its nearest neighbours. These properties of the system make it very easy to solve using a simple iterative technique.

The relaxation method

Once the computational grid has been set up, each nodal temperature in the structure is initialised to some arbitrary value (usually the heat sink temperature - the actual value does not influence the final solution but it does affect the speed of the convergence). The nodes are stepped through one by one and at each node, Eqn. 3.30 is applied so that the finite differences at that point are satisfied. However, once a nodal

temperature has been updated, its neighbours values will change once the sweep reaches those points and the finite-differences will no longer be satisfied. In order to reach a solution the above procedure must be repeated many times and gradually after each iteration, the nodal temperatures will converge to values that simultaneously satisfy the finite-differences at all the grid points and the grid is said to be *relaxed*.

In order to include the effect of a temperature dependent thermal conductivity, after each iteration when the nodal temperatures have been updated, the thermal conductivities are also updated according to the updated temperatures.

In order to speed convergence and reduce the number of iterations required a successive over-relaxation (SOR) technique can be implemented. In this scheme, instead of applying the updated temperature T'_P at each node determined by Eqn. 3.30, an over-corrected value T''_P is applied instead.

$$T''_P = \omega T'_P + (1 - \omega) T_P \tag{3.35}$$

where ω is the relaxation factor and can be in the range $1 \leq \omega < 2$. It is very difficult to calculate an optimum value of ω to speed converge without causing instability and is best chosen through experience[4].

In order to determine when the system of equations are relaxed and a solution has been reached the residual at each point is calculated using

$$R = T'_P - T_P. \tag{3.36}$$

In order to measure the level of convergence independently of the magnitude of the nodal temperatures, R is normalised by T'_P

$$R^N = \frac{T'_P - T_P}{T'_P} = 1 - \frac{T_P}{T'_P}. \tag{3.37}$$

The iterative process is repeated until the maximum normalised residual (R^N_{max}) during the current iteration is less than a set tolerance level (which in this work is 10^{-6}).

[4]During this work, a value between 1.7–1.9 has been found to give acceptable levels of convergence

3.4.3 Time-domain solution

In order to find the solution in the time-domain, Eqn. 3.18 is rearranged to make T_P^{m+1} the subject.

$$T_P^{m+1} = T_P^m + \frac{\Delta T}{\rho_P c_P} \frac{\Delta t}{\Delta x^2 \Delta y^2} \tag{3.38}$$

where

$$\begin{aligned} \Delta T = {} & \kappa_e (T_E^m - T_P^m)\Delta y^2 + \kappa_w (T_W^m - T_P^m)\Delta y^2 \\ & + \kappa_n (T_N^m - T_P^m)\Delta x^2 + \kappa_s (T_S^m - T_P^m)\Delta x^2 \\ & + Q_P^m \Delta x^2 \Delta y^2. \end{aligned} \tag{3.39}$$

The above equation can be solved using a simple explicit time-marching algorithm. It can be seen from the above equation that the temperature at node P in the current time step $(m+1)$ is determined by the temperature of nodes P, N, S, E and W in the previous (m) time step together with Q_P also in the previous time step. It is therefore straight forward to initialise the nodal temperatures (again to the heat sink temperature) at $t = 0$ and then increment t by Δt, update each nodal temperatures according to Eqn. 3.38 (and also the material properties). This process can then be repeated until the required time duration is complete.

Stability issues

As is the case with many explicit numerical solutions of partial differential equations, in order to achieve convergence, the Courant–Friedrichs–Levy (CFL) condition must be obeyed. This convergence criteria sets certain constraints on the maximum allowed time step dependent upon the grid size. For instance, if a simple wave equation was being solved, the maximum time step must be less than the time it would take for the wave to travel to the next grid point. For the case of the two-dimensional heat equation, this means that the time step is limited to

$$\Delta t \leq \frac{\rho c}{2k} \left(\frac{\Delta x^2 \Delta y^2}{\Delta x^2 + \Delta y^2} \right). \tag{3.40}$$

It can be seen from the above equation that the smaller the step in the $x-$ and $y-$axis, the smaller the time step must be. This can be problematic in the fact that for small values of Δx and Δy, Δt can become extremely small and hence increase

the number of time steps required in order to simulate a given time period. In fact, if Δx and Δy are halved, Δt must be reduced by a factor of four to maintain stability. Halving the mesh sizes will also increase the number of mesh points (and therefore RAM requirements) by a factor of four. This means that the total number of required calculations (i.e. CPU runtime) for a given duration of time will increase by a factor of $2^4 = 16$.

3.5 Conclusions

It has been shown how knowledge of the active region temperature of a QCL is very important if device performance is going to be improved. At high temperatures, thermal backfilling and electron leakage combine to severely reduce the population inversion and hence the maximum device operating temperatures. Methods of reducing the active region temperature, such as active region optimisation and the incorporation of advanced thermal management techniques to reduce the thermal resistance have been discussed.

In order to help to understand the thermal dynamics of QCLs further, the development of a thermal model based upon Fourier's law of heat diffusion has been presented. The model takes into account the anisotropic thermal conductivity of the QCL active region caused by its supperlattice-like nature and temperature- and doping-dependent material parameters. The heat equation has been solved used finite-differences in both the steady-state and the time-domain, meaning QCLs can be simulated under both cw and pulsed operating conditions.

References

[1] C. Faugeras, S. Forget, E. Boer-Duchemin, H. Page, J. Bengloan, O. Parillaud, M. Calligaro, C. Sirtori, M. Giovannini, and J. Faist, "High-power room temperature emission quantum cascade lasers at $\lambda = 9\mu$m," *IEEE J. Quantum. Electron*, vol. 41, pp. 1430–1438, 2005.

[2] C. Gmachl, A. M. Sergent, A. Tredicucci, F. Capasso, A. L. Hutchinson, D. L. Sivco, J. N. Baillargeon, S. G. Chu, and A. Y. Cho, "Improved CW operation of quantum cascade lasers with epitaxial-side heat-sinking," *Photon. Technol. Lett.*, vol. 11, 1999.

[3] M. Beck, J. Faist, U. Oesterle, M. Ilegems, E. Gini, and H. Melchior, "Buried heterostructure quantum cacade lasers with a large optical cavity waveguide," *Photon. Technol. Lett.*, vol. 12, pp. 1450–1452, 2000.

[4] M. Beck, D. Hofstetter, T. Aellen, J. Faist, U. Oesterle, M. Ilegems, E. Gini, and H. Melchior, "Continuous wave operation of a mid-infrared semiconductor laser at room temperature," *Science*, vol. 295, p. 301, 2002.

[5] A. Evans, J. S. Yu, S. Slivken, and M. Razeghi, "Continuous-wave operation of $\lambda \sim 4.8\mu$m quantum-cascade lasers at room temperature," *Appl. Phys. Lett.*, vol. 85, no. 12, p. 2166, 2004.

[6] A. Evans, J. S. Yu, J. David, K. Mi, S. Slivken, and M. Razeghi, "High-temperature, high-power, continuous-wave operation of buried heterostructure quantum-cascade lasers," *Appl. Phys. Lett.*, vol. 84, no. 3, p. 314, 2004.

[7] S. Adachi, *GaAs and Related Materials: Bulk Semiconducting and Superlattice Properties*. World Scientific, 1994.

[8] S. Adachi, *Properties of Aluminium Gallium Arsenide*. EMIS Datareviews Series No. 7, INSPEC, London, 1993.

[9] J. C. Brice, *Properties of Indium Phosphide*. EMIS Datareviews Series No. 6, INSPEC, London, 1991.

[10] C. LaBounty. PhD thesis, University of California, Berkeley, 1999.

[11] G. Chen, "Thermal conductivity and ballistic-phonon transport in the cross-plane direction of superlattices," *Phys. Rev. B*, vol. 57, pp. 14958–14973, 1998.

[12] W. S. Capinski, H. J. Maris, T. Ruf, M. Cardona, K. Ploog, and D. S. Katzer, "Thermal-conductivity measurements of GaAs/AlAs superlattices using a picosecond optical pump and probe technique," *Phys. Rev. B*, vol. 59, pp. 8105–8113, 1999.

[13] G. Chen and M. Neagu, "Thermal conductivity and heat transfer in superlattices," *Appl. Phys. Lett.*, vol. 71, pp. 2761–2763, 1997.

[14] G. Scamarcio, M. S. Vitiello, V. Spagnolo, S. Kumar, B. S. Williams, and Q. Hu, "Nanoscale heat transfer in quantum cascade lasers." accepted for publication in Physica E.

[15] S. T. Huxtable, A. R. Abramson, C. Tien, A. Majumdar, C. LaBounty, X. Fan, G. Zeng, J. E. Bowers, A. Shakouri, and E. T. Croke, "Thermal conductivity of Si/SiGe and SiGe/SiGe superlattices," *Appl. Phys. Lett.*, vol. 80, no. 10, p. 1737, 2002.

[16] A. Lops, V. Spagnolo, and G. Scamarcio, "Thermal modeling of GaInAs/AlInAs quantum cascade lasers," *J. Appl. Phys.*, vol. 100, no. 043109, pp. 1–5, 2006.

[17] A. J. Borak, C. C. Phillips, and C. Sirtori, "Temperature transients and thermal properties of GaAs/AlGaAs quantum-cascade lasers," *Appl. Phys. Lett.*, vol. 82, no. 23, p. 4020, 2003.

[18] D. G. Cahill and R. O. Pohl, "Thermal conductivity of amorphous solids above the plateau," *Phys. Rev. B*, vol. 35, pp. 4067–4073, 1987.

[19] "NSM Archive - Ioffe Physico-Technical Institute - Physical properties of semiconductors." online. http://www.ioffe.ru/SVA/NSM/Semicond/.

[20] Y. G. Zhang, Y. J. He, and A. I. Li, "Transient thermal analysis of InAlAs /InGaAs /InP mid-infrared quantum cascade lasers," *Chin. Phys. Lett.*, vol. 20, pp. 678–681, 2002.

Chapter 4

Transient thermal analysis of quantum cascade lasers

4.1 Introduction

As described in the previous chapter, when a QCL is operated in pulsed mode significantly less active region heating occurs than when in cw and therefore higher heat sink temperatures can be reached. For instance, one of the highest operating temperature THz QCLs lases up to 167 K in pulsed mode and 117 K in cw [1]. Although cw operation is desirable for certain applications, the higher temperatures that can be reached in pulsed mode can be the most important factor under certain circumstances. It is therefore important to understand the effect of different driving conditions on the active region temperature.

In this chapter, the thermal dynamics of a QCL operating in pulsed mode are investigated using the transient thermal model described in Sec. 3.4.3. The benchmark QCL at the centre of the work is a $\lambda \sim 3\mu$m InGaAs/AlAsSb QCL which is the focus of Chapter 6 and is discussed in much detail there. The various heat management techniques outlined in Sec. 3.1 are compared and the effect of various operating conditions on the active region temperature is investigated.

The work presented in this chapter was published in IEEE Journal of Quantum Electronics, 'Investigation of thermal effects in quantum cascade lasers', Volume 42, pp. 859–867 (2006).

4.2 Device structure and theoretical framework

The benchmark QCL is based upon the device described in Ref. [2], an InP-based QCL with an InGaAs/AlAsSb active region. The substrate is taken to be 100 μm thick and the InP upper waveguide cladding layers are taken as 2.5 μm in total. The active region is composed of 30 periods giving a total active region thickness of 1.5 μm. The laser ridge is assumed to be 10 μm wide and the cavity 2 mm long. The ridge is assumed to be coated in 500 nm of SiO_2 insulation with a 4 μm window on top of the ridge for the top contact. The whole device is then assumed to be coated in 1 μm of gold acting as the top contact. A schematic of the device is shown in Fig. 4.1a.

The active region of the device is taken to be the same as the one described in Chapter 6. From electron transport calculations[1] as described in Chapter 6, the electric field–current density curves were calculated at a variety of lattice temperatures and are shown in Fig. 4.2. By extracting the current density as a function of lattice temperature at the operating bias point of 135 kV/cm, a 'quantum source term' can be extracted which gives the electrical power density dissipated in the active region which is generated in the active region through quantum mechanical effects. The temperature dependent electrical power density $Q(T)$ is given by $FJ(T)$ and by fitting the data in Fig. 4.2 is found to be $Q = 1 \times 10^{15} \exp(T/1023)$ W/m^3. This source term is entered directly into the thermal model. Using the active region dimensions given earlier in the section, the equivalent electrical power dissipated in the active region is $P = 30 \exp(T/1023)$ W. Resistive heating in the cladding layers is ignored.

The device is found to generate enough gain for laser action to be possible up to a lattice temperature of 300 K (again, this will be explained in more detail in Chapter 6 but for now just the result is important).

As discussed in Sec. 3.4.3, the time step of the simulations is determined by the mesh size and in this work a mesh size of $\Delta x = \Delta y = 500$ nm is used. This gives an acceptable mesh density while allowing a large enough time step (of the order of ns) to make the simulation run-times feasible.

[1] At this point, the method of calculating the $I - V$ curves and gain are not important, just the final results. The method is explained in great depth in Chapter 6

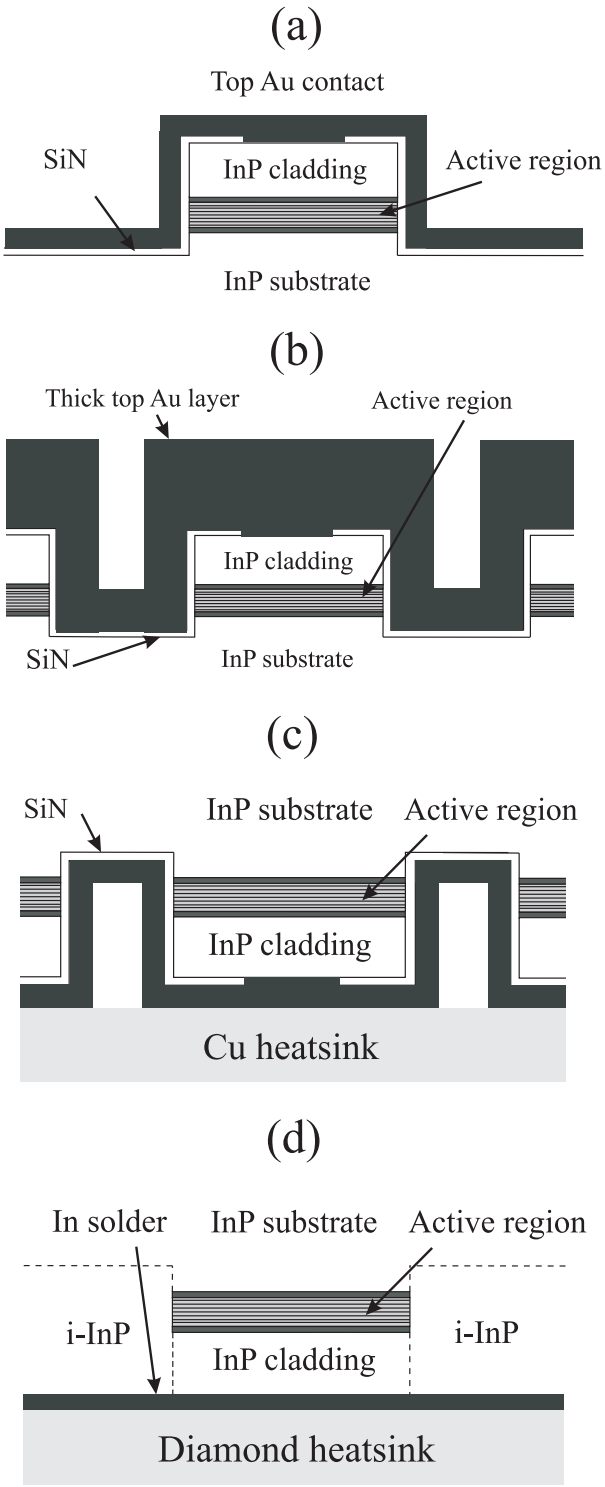

Figure 4.1: Schematic diagrams of the device structures used in the simulations (a) standard ridge waveguide (b) double channel ridge with electroplated gold (c) epilayer-down mounted device and (d) a buried heterostructure.

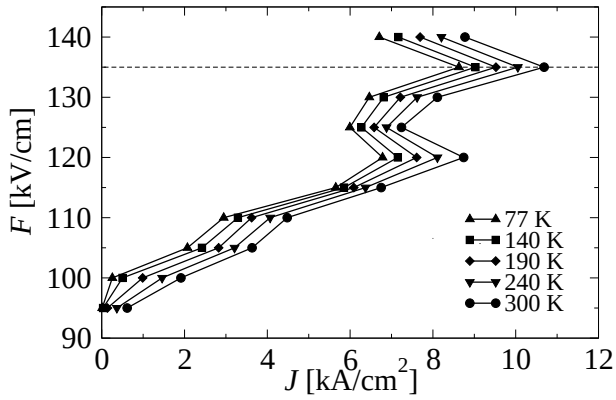

Figure 4.2: Electric field versus current density characteristics for a range of lattice temperatures. The operating bias point (135 kV/cm) is denoted by the dotted line.

At the time of this work, little was known about the thermal conductivity of QCL active regions apart from the fact that the cross-plane thermal conductivity $\kappa_\perp$ was considerably less than bulk. There was also found to be little knowledge in the literature of the thermal properties of AlAsSb and so the approach of Ref. [3] was followed; the in-plane thermal conductivity of the active region $\kappa_\parallel$ is taken to be that of bulk InGaAs and $\kappa_\perp$ is taken to be one order of magnitude smaller. Therefore, the work in this chapter is equally applicable for InGaAs/InAlAs QCLs based on InP substrates assuming that the heat generated in the active region is the same for each case.

4.3 Influence of operating conditions

In this section, the operating conditions of the benchmark laser are varied to see the effect on the calculated device performance. When operated in pulsed mode, the device heats up during the pulse and this heat then dissipates in the period before the next pulse arrives. Depending upon the pulse width and repetition frequency, the active region may not have recovered the heat sink temperature by the time the next pulse arrives. This means that during the next pulse the maximum temperature will be higher and this process carries on for several periods until the system settles to a steady-state. This is highlighted in Fig. 4.3 which shows the temperature–time profile at a heat sink temperature of 200 K with 100 ns pulses and a 500 kHz repetition frequency (5 % duty cycle).

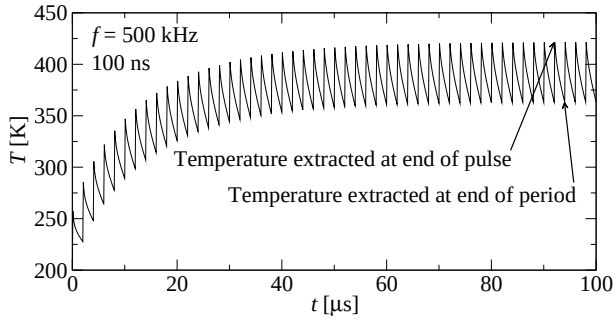

Figure 4.3: Temperature–time profile for a standard ridge waveguide showing the average active region temperature as a function of time.

In this work, the temperatures are extracted once this steady-state has been reached.

4.3.1 Heat sink temperature

Fig. 4.4 shows the effect of varying the heat sink temperature on both the minimum and maximum value of the active region temperature for 100 ns pulses at 100 kHz (1 % d.c.). The temperatures are extracted at the end of the pulse. It can be seen

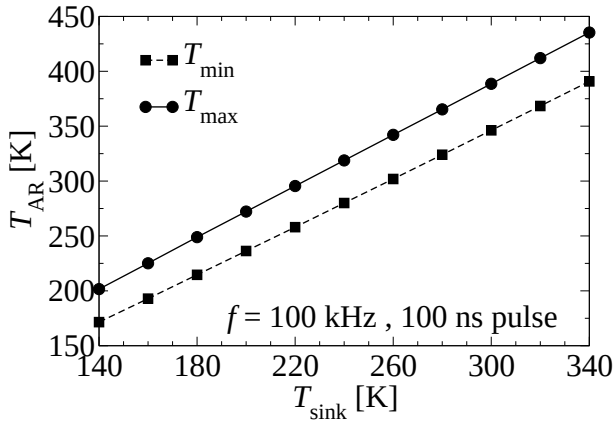

Figure 4.4: Spatial minimum and maximum values of T_{AR} for different values of T_{H} at 100 kHz with 100 ns pulse widths.

from the figure that T_{AR} increases linearly with T_{H}. The relationship is of the form $T_{\mathrm{AR}} = T_1 + \alpha_{\mathrm{s\text{–}AR}} T_{\mathrm{H}}$, where $\alpha_{\mathrm{s\text{–}AR}}$ is a coupling constant between the heat sink and active region and is extracted from straight line fits to the data. For the case of $T_{\mathrm{AR}}^{\mathrm{max}}$, $\alpha_{\mathrm{s\text{–}AR}} = 1.167$, while for $T_{\mathrm{AR}}^{\mathrm{min}}$ it is equal to 1.097. Hence as $\alpha_{\mathrm{s\text{–}AR}}^{\mathrm{max}} > \alpha_{\mathrm{s\text{–}AR}}^{\mathrm{min}}$, the temper-

ature range inside the active region increases with increasing T_{H} which could cause damaging thermal stress effects at high sink temperatures. The cause of the temperature range increase is due to the thermal conductivity of the materials in the devices decreasing with temperature. The hotter areas of the active region have a lower thermal conductivity than the cooler areas and are less able to dissipate heat leading to an increase in temperature, while the cooler areas are better able to dissipate heat and hence the temperature rise is not as great.

For the case of the InGaAs/AlAsSb QCL in question being driven under these conditions (100 ns, 100 kHz) at T_{H} = 220 K, the entirety of the active region is less than 300 K, meaning laser action would be expected. With T_{H} = 240 K, the active region has a temperature range of ∼260–325 K, meaning that only the active region periods at $T < 300$ K would contribute to lasing resulting in a decrease in output power. Even at T_{H} = 255 K, some of the active region is still less than 300 K and so laser action may still be present at this temperature.

The fact that the temperature gradient inside the active region increases with heat sink temperature could help to explain the abrupt decrease in slope efficiency at higher temperatures which has been measured experimentally [4]. When the device is being operated at close to its maximum temperature, not all of the active region periods may be contributing to laser action. As the heat sink temperature is increased, the temperature gradient is increased further and less periods will contribute to laser action. This process will cause the output power to decrease further (and hence the slope efficiency) until eventually all of the active region periods will cease lasing and the device reaches cut-off. In addition, if each of the active region periods are at a slightly different temperature, the amount of red shift in the emission wavelength will vary, leading to a broadening of the linewidth.

It is possible to define a thermal resistance for the device using Eqn. 3.1. The dissipated power is calculated using the quantum source term mentioned previously. The upper and lower limits of the pulsed mode device thermal resistance are plotted in Fig. 4.5 for the different heat sink temperatures. These values of R_{TH} are very small compared to conventional values for InP-based MIR device (see Chapter 5) due to

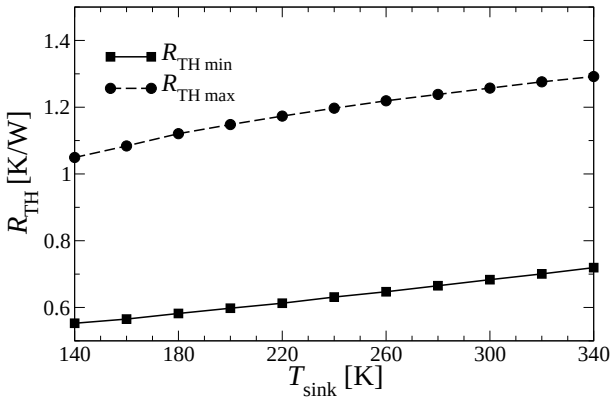

Figure 4.5: Upper and lower bounds of the pulsed mode thermal resistance as a function of heat sink temperature.

the fact that the device is operated in pulsed mode. The temperature rise (and hence R_{TH}) is limited by the pulse width and so the thermal resistance will be different for different duty cycles. The figure shows the thermal resistance increasing with heat sink temperature which is a direct consequence of the thermal conductivities being reduced at higher lattice temperatures.

4.3.2 Pulse repetition rate

The duty cycle can be increased by increasing either the pulse repetition frequency or the pulse width (or a combination of both). The same device as described in the previous sections was simulated with T_{H} = 200 K and a pulse width of 100 ns at different repetition rates and the results are shown in Fig. 4.6a. For frequencies of less than 50 kHz, the temperature range of the active region is independent of the pulse frequency. This is due to the relatively long time period between pulses, which gives the active region enough time to entirely dissipate the heat accumulated during the pulse and recover the heat sink temperature. For these cases, the only factors which affect the active region temperature range are the heat sink temperature (which determines the thermal conductivities of the materials and the source power density) and the pulse width (determines how much the active region heats up). These are constant in this simulation and hence the temperature profiles in Fig. 4.6a are flat for frequencies below 50 kHz. Above this value of frequency the active region temperatures start to rise

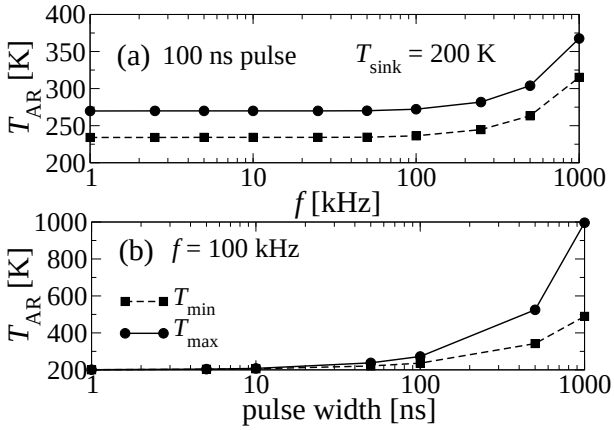

Figure 4.6: (a) T_{AR} for different pulse frequencies with a pulse width of 100 ns. (b) T_{AR} for different pulse widths with $f = 100$ kHz. In both cases T_H = 200 K.

rapidly due to heat accumulation effects. This heat accumulation effect is outlined in Fig. 4.7 which shows the device cross section temperature profile (taken along the line of symmetry in Fig. 4.1a) evolving with time at a frequency of 500 kHz (period length 2 μs). It can clearly be seen how the heat in the device builds up during each successive pulse. For the InGaAs/AlAsSb QCL in question, with 100 ns pulses and T_H

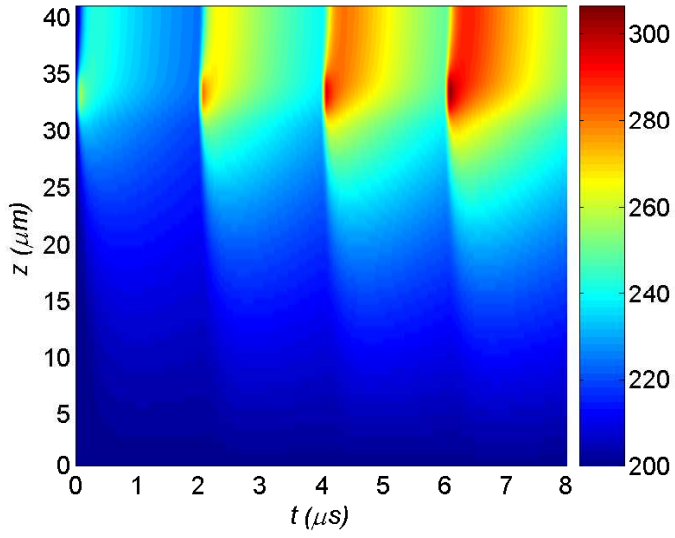

Figure 4.7: Time evolution of the QCL cross-sectional temperature profile. T_H = 200 K and the time period between the 100 ns pulses is 2 μs (500 kHz).

= 200 K, a repetition frequency of ~600 kHz (6 % duty cycle) is possible without the

entire active region being above 300 K and hence laser action could occur. An advantage of intersubband devices over interband devices is the ultrafast carrier lifetimes (on the order of picoseconds) meaning extremely high modulation frequencies in the GHz should be possible [5]. Figs. 4.6 and 4.7 highlight the fact that to achieve high frequency modulation (and indeed cw operation) in QCLs, careful thermal management is required to improve the heat dissipation away from the active region and reduce the heat accumulation effects.

4.3.3 Pulse width

The effect of increasing the duty cycle by increasing the pulse width on T_{AR} is shown in Fig. 4.6b. For pulse widths of less than 10 ns, very little active region heating occurs. Above this value there is a considerable increase in active region temperature with pulse width. This is due in principal to the same heat accumulation effects that are outlined in Fig. 4.6a but on a more pronounced scale. In Fig. 4.6a for a 100 ns pulse, 1000 kHz corresponds to a 10 % duty cycle and the maximum active region temperature is $\sim$370 K. In the case of Fig. 4.6b, a 10 % duty cycle is equivalent to a 1000 ns pulse and the maximum active region temperature is $\sim$ 1000 K. This is caused by the rate of temperature increase during the pulse being far greater than the rate of temperature decrease during cooling phase. Therefore it is better to increase the duty cycle by increasing the pulse repetition frequency rather than increasing the pulse width. In terms of the InGaAs/AlAsSb QCL, for a 100 kHz repetition frequency at a 200 K heat sink temperature, a maximum pulse width of $\sim$ 200 ns (2 % duty cycle) is possible without the entire active region temperature rising above 300 K.

4.3.4 Ridge width

The previous sections have investigated the effects of the QCL driving conditions on the active region heating with a 10 μm wide ridge. In this section the effect of increasing the ridge width is investigated and the results are shown in Fig. 4.8. It should be noted that the electrical power density is kept constant in the simulations to make the comparison more meaningful. If the electrical power was kept constant, the density

would be less for the larger ridge widths (larger volume) and so less heating would occur. It can be seen from the figure that both the active region temperature and the

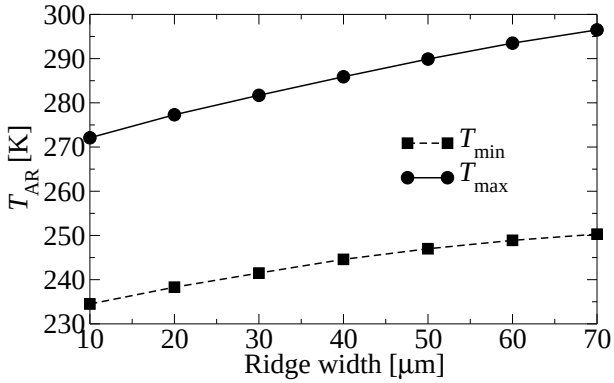

Figure 4.8: Spatial minimum and maximum values of T_{AR} for different ridge widths. T_H = 200 K and the pulse width is 100 ns with a 100 kHz.

temperature range inside the active region increase with the ridge width, agreeing with experiment [6]. This is explained by a wider laser ridge having a greater active region volume meaning higher power and therefore more heating. Narrow ridges would therefore be advantageous at high temperatures from a thermal viewpoint although decreasing the ridge width would also decrease the maximum power due to the smaller emitting volume.

4.4 Comparison of thermal management techniques

In the previous sections, the investigations have been carried out on a standard ridge waveguide mounted substrate side down. In this configuration (which is shown schematically in Fig. 4.1a), heat must escape from the active region through the substrate to the heat sink. Efficient heat transfer in this direction is prevented by the small $\kappa_\perp$ and consequently substantial active region heating occurs. Alternative device geometries which were discussed in Sec. 3.1 are possible which improve the heat dissipation from the active region and the schematic cross-sections of these are shown in Fig. 4.1. For the case of the double-channel ridge waveguide (Fig. 4.1b), a thick (5 μm) gold layer is electroplated (EP) on top of the laser ridge to efficiently spread the current and heat on the laser surface and the device is mounted substrate side down [7].

The epilayer-down mounted device (Fig. 4.1c) is a double-channel ridge waveguide which has then been soldered epilayer-down onto the copper heat sink. In the following simulations, it is assumed that the indium solder between the heat sink and the top contact is pressed out during mounting, as described in [3]. Fig. 4.1d shows a buried heterostructure (BH) device in which the active region is completely surrounded by i-InP allowing heat to escape in all directions. In order to further improve the performance of the devices, BH QCLs have been used in conjunction with epilayer-down bonding on diamond heat sinks. This configuration led to the first demonstration of a QCL operating in cw at room-temperature [8].

In order to compare the different device configurations, the temperature–time profiles and device cross-section temperature profiles were calculated for each. The average active region temperatures as a function of time for the different configurations are shown in Fig. 4.9.

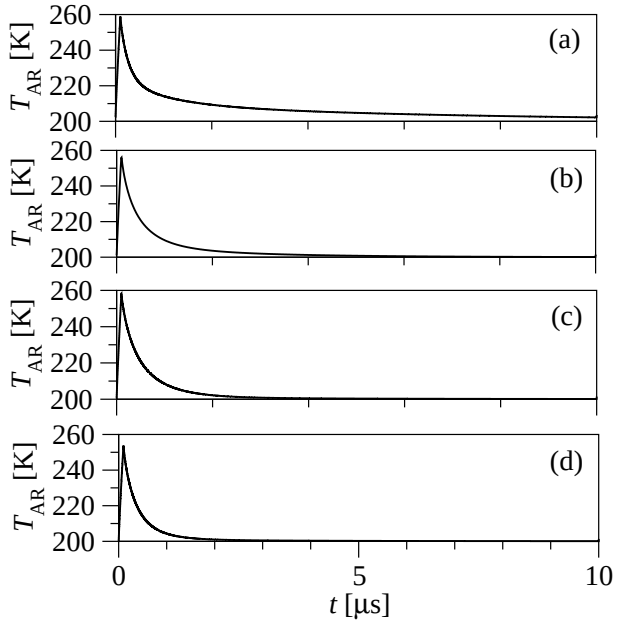

Figure 4.9: Temperature–time profiles (average T_{AR}) for (a) a standard ridge waveguide (b) a double channel waveguide mounted substrate side down with electroplated gold (c) epilayer-down mounted ridge waveguide on a copper heat sink and (d) a buried heterostructure mounted epilayer-down on a diamond heat sink. All simulations are at $T_H = 200$ K, with 100 ns pulses at a repetition rate of 100 kHz.

For the benchmark ridge waveguide (A), the average T_{AR} at the end of the pulse

is 262 K. Both the double-channel ridge waveguide mounted epilayer-down (B) and the gold covered double-channel ridge waveguide mounted substrate side down (C) have the same T_{AR} of ~ 258 K at the end of the pulse. For the case of the BH device (D), this is reduced slightly to ~ 252 K. In this instance, due to the small pulse width, the effect of the different configurations on the maximum active region temperature is relatively small, however it does play a large part in the ability of the device to dissipate heat away from the active region. In order to characterise the heat dissipation ability, the cooling phase of the temperature–time profiles were fitted using a second-order exponential decay function [9]. Table 4.1 shows the fitted equations for each structure. It can be seen that for the case of the devices mounted substrate side down,

Table 4.1: Results of fitting the cooling phases of each structure (Fig. 4.9) to a second-order exponential decay function

$T_{\mathrm{AR}} = a_0 + a_1 \mathrm{e}^{-t/\tau_1} + a_2 \mathrm{e}^{-t/\tau_2} \quad (t > 100 \text{ ns})$

Device	a_0	a_1	$\tau_1(\mu\mathrm{s})$	a_2	$\tau_2(\mu\mathrm{s})$
A	203.0	47.5	0.19	32.1	2.67
B	203.1	75.5	0.17	13.7	1.98
C	200.1	32.4	0.14	52.3	0.47
D	200.1	43.7	0.12	45.3	0.33

A and B, a_0 is slightly higher than T_{H} due to the slight heat accumulation effects in these configurations. However, for the epilayer down mounted devices, no heat accumulation effects occur and so a_0 is very close to T_{H}. The second-order exponential fit indicates that there are two distinct cooling stages (denoted by the two thermal time constants τ_1 and τ_2). τ_1 represents the heat initially escaping from the active region into the waveguide cladding and insulation layers primarily in the vertical direction. The substrate side mounted devices are similar in this respect and hence the values

of τ_1 for these devices are relatively similar. Although device C, the double-channel ridge waveguide mounted epilayer down, has a similar structure to devices A and B), the upper cladding layer is in closer proximity to the heat sink and hence its value of τ_1 is smaller. In the case of device D, the BH device, heat diffusion can take place in both the vertical and lateral directions and in combination with the epilayer down mounting causes the buried heterostructure to have the smallest value of τ_1.

The time constant τ_2 represents the second stage of cooling in which the heat diffuses towards the heat sink through the substrate and cladding regions. It appears from the data that this mechanism dominates the cooling process and is the major difference between the different device mountings. τ_2 is much longer in devices A and B, compared to devices C and D, since they are mounted substrate side down and so the heat generated in the active region has to diffuse through the substrate to reach the heat sink. τ_2 is smaller in device B compared to device A since heat can spread into the thick gold layer on top of the laser ridge as well as into the substrate which is the only heat escape channel in device A. Devices C and D have values of τ_2 several times smaller than devices A and B due to the epilayer down mounting and hence the active region being in closer proximity to the heat sink. τ_2 is smaller in the BH device and this is likely due to both the effect of heat escaping both vertically and laterally, and the fact that diamond has a higher thermal conductivity than copper. Fig. 4.10 shows the cross section temperature profiles for each of the devices at $t = 1$ μs.

Devices A and B have similar temperature profiles, with heat primarily escaping through the substrate, although the thick gold layer causes a reduction in the average active region temperature at t = 1 μs from 225 K in the standard ridge to 210 K in the gold covered device. Fig. 4.10d shows the heat escaping from the active region of the BH device in all directions compared to the primarily vertical heat channel in the epilayer-down mounted double-channel ridge waveguide (Fig. 4.10c), leading to a lower average active region temperature.

Table 4.1 and Fig. 4.10 highlight the fact that a BH device is up to now one of the best solutions in terms of thermal management of QCLs, especially in conjunction with epilayer down mounting. As well as the reduced active region temperature,

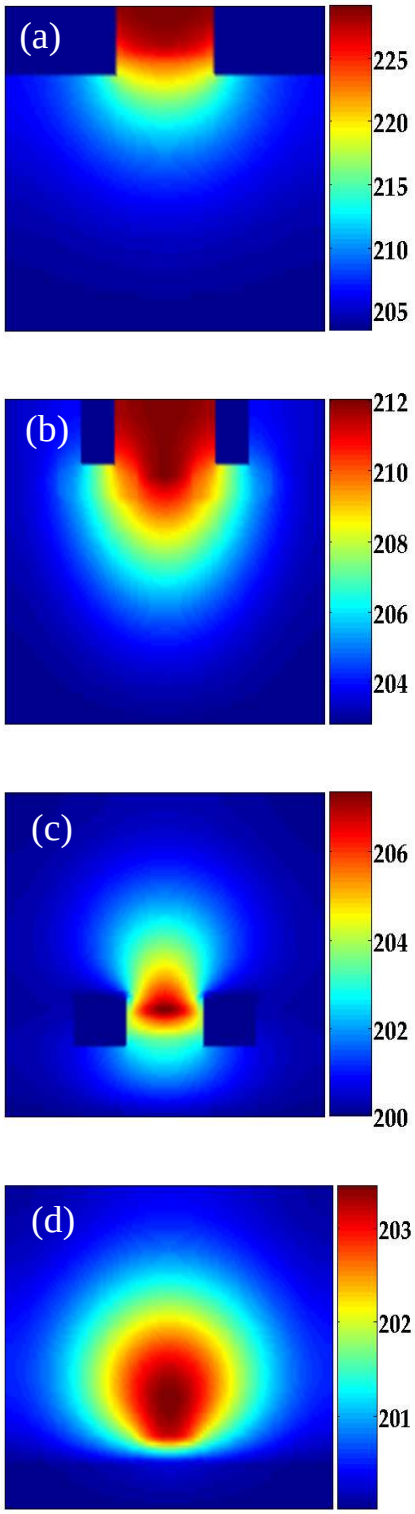

Figure 4.10: Cross sectional temperature profiles for each of the devices in Fig. 4.9, 1 μs into the period (0.99 μs into the cooling stage). Note the different temperature scales.

the temperature profile inside the active region is much more uniform and so the majority of the periods will be at the same temperature. Despite this improvement, the increased performance must be balanced against the much more complicated processing techniques required.

4.5 Conclusions

Thermal analysis of an InGaAs/AlAsSb QCL has been carried out under a range of operating conditions. Electron transport calculations (which will be discussed in more depth in Chapter 6) have been performed in order to find the temperature dependent power density generated in the device active region. Sufficient gain was estimated up to a lattice temperature of 300 K.

As the heat sink temperature is increased, it has been seen that the temperature range inside the active region increases, which could cause detrimental thermal stress problems at high heat sink temperatures. Since each period of the QCL active region has a different temperature, close to cut-off, some periods may not be contributing to lasing and is a probable cause of the output power roll-off observed experimentally.

It has been found that the device is much more sensitive to an increase in duty-cycle through using a longer pulse rather than a higher repetition rate. This is due to the rate of temperature rise in the active region during the pulse being considerably large than the rate of temperature decrease in between pulses. Larger ridge widths have been shown to cause a larger temperature rise (for a given power density), simply due to the larger emitting volume. This means a trade-off must be made between power and temperature performance (since a smaller emitting volume means a lower output power).

Different thermal management techniques (a epilayer-down mounted device, a EP gold-covered device and a buried heterostructure) have been compared to the benchmark ridge structure. The buried heterostructure is found to be the best solution in terms of thermal management due to heat being able to dissipate from the active region in all directions, leading to thermal time constants several times smaller than those found in standard ridge waveguides.

References

[1] B. S. Williams, S. Kumar, Q. Hu, and J. L. Reno, "Operation of terahertz quantum-cascade lasers at 164 K in pulsed mode and at 117 K in continuous-wave mode," *Opt. Express*, vol. 13, no. 9, p. 3331, 2005.

[2] C. A. Evans, V. D. Jovanović, D. Indjin, Z. Ikonić, and P. Harrison, "Investigation of thermal effects in quantum-cascade lasers," *IEEE J. Quantum. Electron*, vol. 42, pp. 859–867, 2006.

[3] Q. Yang, C. Manz, W. Bronner, R. Moritz, C. Mann, G. Kaufel, K. Köhler, and J. Wagner, "Continuous-wave operation of GaInAs/AlGaAsSb quantum-cascade lasers," *Photon. Technol. Lett.*, vol. 17, no. 11, p. 2283, 2005.

[4] J. S. Yu, A. Evans, S. Slivken, S. R. Darvish, and M. Razeghi, "Short wavelength ($\lambda \sim 4.3\mu m$) high-performance continuous-wave quantum-cascade lasers," *Photon. Technol. Lett.*, vol. 17, no. 6, p. 1154, 2005.

[5] F. Capasso, R. Paiella, R. Martini, R. Colombelli, C. Gmachl, T. L. Myers, M. S. Taubman, R. M. Williams, C. G. Bethea, K. Unterrainer, H. Y. Hwang, D. L. Sivco, A. Y. Cho, A. M. Sergent, H. C. Liu, and E. A. Whittaker, "Quantum cascade lasers: ultrahigh-speed operation,optical wireless communication, narrow linewidth, and far-infrared emission," *IEEE J. Quantum. Electron*, vol. 38, no. 6, pp. 511–532, 2002.

[6] S. Slivken, J. S. Yu, A. Evans, J. David, L. Doris, and M. Razeghi, "Ridge-width dependence on high-temperature continuous-wave quantum-cascade laser operation," *Photon. Technol. Lett.*, vol. 16, no. 3, p. 744, 2004.

[7] J. S. Yu, S. Slivken, S. R. Darvish, A. Evans, B. Gokden, and M. Razeghi,

"High-power, room-temperature, and continuous-wave operation of distributed-feedback quantum-cascade lasers at $\lambda \sim 4.8\mu$m," *Appl. Phys. Lett.*, vol. 87, no. 041104, p. 1, 2005.

[8] M. Beck, D. Hofstetter, T. Aellen, J. Faist, U. Oesterle, M. Ilegems, E. Gini, and H. Melchior, "Continuous wave operation of a mid-infrared semiconductor laser at room temperature," *Science*, vol. 295, p. 301, 2002.

[9] C. Zhu, Y. G. Zhang, A. Z. Li, and Y. L. Zheng, "Comparison of thermal characteristics of antimonide and phosphide MQW lasers," *Semicond. Sci. Technol.*, vol. 20, p. 563, 2005.

Chapter 5

Steady-state thermal analysis of quantum cascade lasers

5.1 Introduction

In this chapter, both MIR and THz QCLs are investigated whilst under cw operation which is highly desirable for applications such as trace gas sensing. As mentioned in previous chapters, in cw mode, significant amounts of electrical power are dissipated in device active regions causing large temperature rises compared to the heat sink which are detrimental to device performance.

5.2 Thermal analysis of THz QCL optical waveguides

This work was carried out in collaboration with the group of Prof. Scamarcio at the CNR INFM Regional Laboratory LIT^3 in the Dipartimento Interateneo di Fisica "M.Merlin" at the Universitá degli Studi di Bari, Italy, who are a leading experimental group who specialise in determining the lattice temperature of QCLs using a micro-probe photoluminescence (PL) technique [1, 2].

The work has been submitted to IEEE Journal of Quantum Electronics, 'Thermal modeling of terahertz quantum-cascade lasers: comparison of optical waveguides', Craig A. Evans, Dragan Indjin, Zoran Ikonić, Paul Harrison, Miriam S. Vitiello, Vincenzo Spagnolo, and Gaetano Scamarcio.

5.2.1 Introduction

THz QCLs have shown a considerable increase in performance since their first demonstration [3], covering the frequency range 1.2 [4] to 4.9 THz [5] (and down to 0.83 THz with the assistance of a magnetic field [6]) with maximum operating temperatures of 117 K in cw [7] and 178 K in pulsed-mode [8]. Improving the maximum operating temperatures of THz QCLs still further is highly attractive for a range of technological applications. This is made inherently more difficult in the THz frequency range than in the MIR due to the smaller photon energy (typically less than 20 meV). At higher lattice temperatures (and hence higher electron temperatures) it becomes more difficult to achieve selective injection and depopulation of the upper and lower laser levels. Additionally, since the photon energy is less than the LO phonon energy (36 meV in GaAs) in the THz frequency range, at sufficiently high electron temperatures, thermally activated LO phonon emission from the upper laser level can significantly reduce the population inversion.

In order to reduce the electron temperature and improve the temperature performance, the lattice temperature itself must be reduced through careful thermal management. Furthermore, THz QCLs particularly suffer compared to MIR devices since they generally contain more active region periods resulting in a larger number of interfaces and a higher value of thermal resistance. It has been found that the interface contribution to the overall thermal resistivity of the THz QCLs can be as high as 97% [9].

The configuration of the optical waveguide also plays an important role in determining the thermal performance of the device and to date, as discussed in Chapter 2, two types of THz optical waveguides have been implemented: semi-insulating surface-plasmon (SISP) and metal-metal (MM) waveguides. THz QCLs with MM waveguides have proven to have to highest operating temperatures thus far [7].

It is clear that in order to understand the internal thermal dynamics of QCLs with the aim of improving temperature performance, knowledge of the temperature dependence of the active region thermal conductivity and the effect of the optical waveguide on the device thermal properties is crucial. In this section, a study of the local

lattice temperature of a surface-emitting distributed-feedback (DFB) THz QCL [10], measured using a microprobe PL technique [1, 2], is presented.

5.2.2 Experimental procedure and results

A microprobe band-to-band PL technique was used to measure the local lattice temperature (T_{L}) of the surface-emitting THz QCL[1]. By measuring the energy of the main PL peak and comparing the shift to calibration curves obtained when probing the device at zero current while varying the heat sink temperature T_{H} it is possible to extract T_{L}. Whereas in previous works the facet temperatures of various THz and MIR devices have been measured [1, 2, 11–13], the use of a surface-emitting device allows T_{L} to be measured on top of the device active region through the apertures in the second-order DFB grating [9]. The investigated sample has an active region thickness of $d = 10$ μm, a ridge width of 45 μm and a cavity length of 1.14 mm. The optical confinement is provided by a MM waveguide fabricated with Cu-Cu bonding. The second-order DFB grating is composed of $i = 1$ to 30 apertures, each 6 μm wide with a grating period of $\Lambda = 30$ μm. Fig. 5.1 shows a schematic picture of the device.

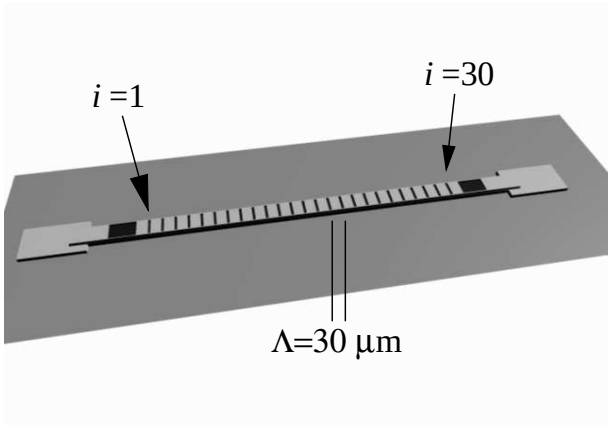

Figure 5.1: Schematic diagram of the surface-emitting DFB THz QCL. The diagram shows the location of the $i = 1$ and $i = 30$ apertures together with the grating period of $\Lambda = 30$ μm. Thanks to Zachary Coldrick for generating the figure.

Fig. 5.2 shows T_{L} measured in the centre of the central ($i = 15$) aperture as a

[1]The experimental measurements were carried out by the group of Prof. Scamarcio at the University of Bari.

function of electrical power P at a heat sink temperature $T_{\mathrm{H}} = 75$ K.

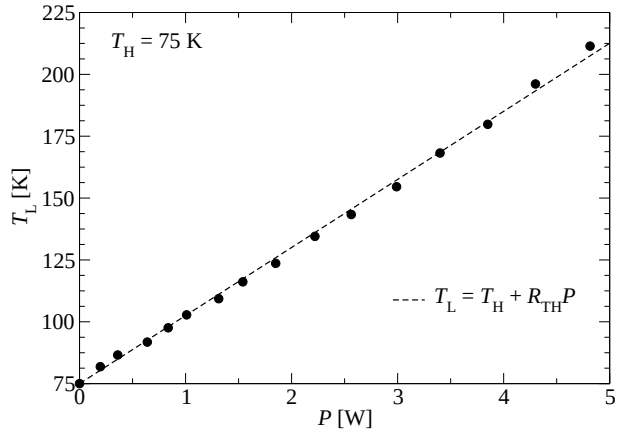

Figure 5.2: Local lattice temperature (T_{L}) measured in the central aperture of the surface-emitting THz QCL as a function of electrical power (P)[Data from Ref. [9]]. The dashed line shows a linear fit to the data according to the relation ($T_{\mathrm{L}} = T_{\mathrm{H}} + R_{\mathrm{TH}}P$) from which a device thermal resistance of $R_{\mathrm{TH}} = 27.8 \pm 0.2$K/W is extracted. All measurements were performed at $T_{\mathrm{H}} = 75$ K.

From the experimental data of Fig. 5.2 the device thermal resistance R_{TH} can be extracted using Eqn. 3.1 and is found to be $R_{\mathrm{TH}} = 27.8$ K/W. It is worth noting that since T_{L} has been measured on top of the laser ridge, which is the hottest region of the device, this value of R_{TH} is an upper bound, if the measurement had been performed on a cooler area of the device the corresponding temperature rise and hence thermal resistance would be smaller.

5.2.3 Extraction of the cross-plane thermal conductivity

In order to fully understand the thermal dynamics of QCLs and improve their temperature performance, knowledge of $\kappa_{\perp}$ and its dependence on temperature is crucial. In this section, the steady-state model described in Sec. 3.4 is employed in conjunction with the experimental data of Sec. 5.2.2 to extract $\kappa_{\perp}$ and its temperature dependence. A two-dimensional cross-section of the device taken from the centre of the laser cavity was simulated for each of the electrical powers in Fig. 5.2 at $T_{\mathrm{H}} = 75$ K with $\kappa_{\perp}$ the only fitting parameter. By matching the value of $\kappa_{\perp}$ in the simulations that causes the same temperature rise as measured for each power in Fig. 5.2, it is possible to extract

$\kappa_\perp$ as a function of temperature and the results are shown in Fig. 5.3.

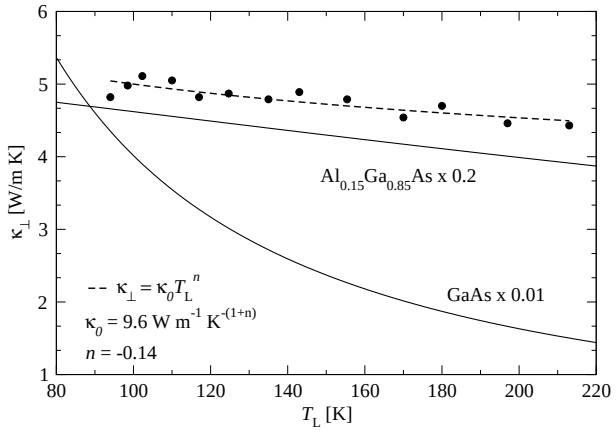

Figure 5.3: Cross-plane thermal conductivity ($\kappa_\perp$) of the active region as a function of temperature extracted from fitting the results of the two-dimensional thermal model to the experimental data presented in Fig. 5.2. The dashed line is a power law fit to the data, $9.6T^{-0.14}$ W m^{-1} K^{-1}. For comparison, the solid lines shows the thermal conductivities of bulk GaAs and $Al_{0.15}Ga_{0.85}As$.

The same power law ($\kappa = \kappa_0 T^n$) that is often used for bulk semiconductors is used to fit the data and values of $\kappa_0 = 9.6$ W m^{-1} K$^{-(1+n)}$ and $n = -0.14$ were extracted. The results show that $\kappa_\perp$ is a decreasing function of temperature with a much weaker temperature dependence than III-V bulk semiconductors, where n is found to be typically in the range $-1.55 \leq n \leq -1.20$ [14]. The values of $\kappa_\perp$ extracted here are in good agreement with experimentally measured values of the cross-plane thermal conductivity of standard edge-emitting THz QCLs ($\kappa_0 = 10.6$ W m^{-1} K$^{-(1+n)}$, $n = -0.16$ [15]) and GaAs/AlAs superlattices [16]. Also shown in Fig. 5.3 for comparison are the thermal conductivities of bulk GaAs and $Al_{0.15}Ga_{0.85}As$ which are much larger than $\kappa_\perp$, a trend which has previously been observed in the GaAs/AlGaAs [17], GaInAs/AlInAs [2, 18] and Si/SiGe [19] material systems.

It is worth noting that as opposed to the decrease of $\kappa_\perp$ with temperature that is found in GaAs-based superlattices, in the GaInAs/AlInAs and Si/SiGe material systems, $\kappa_\perp$ is found to increase with temperature [2, 18, 19].

5.2.4 Thermal properties of THz QCL optical waveguides

The optical waveguide is an integral component of a THz QCL and in order to increase the maximum operating temperature it is important to understand the effect of the waveguide on the thermal properties of the QCL. A Similar study has recently been carried out on InP-based MIR devices [20]. This section presents a comparison between the thermal properties of MM and SISP optical waveguides and the effect on device performance.

In the following simulations, the MM optical waveguide is taken to be the same as the one in Sec. 5.2.2 (45-μm-wide laser ridge and a 1.14-mm-long cavity) with $d = 10$ μm and a 160-μm-thick substrate. In order to make the comparison more meaningful, the SISP waveguide is taken to be similar to the one in [21] (150-μm-wide laser ridge and a 2-mm-long cavity) but with the same active region and substrate thicknesses as the MM waveguide. In the case of the SISP waveguide, the substrate is semi-insulating while the MM waveguide substrate is n^+ doped at 2×10^{18} cm^{-3}. In both cases, the $\kappa_\perp$ values extracted in Sec. 5.2.3 are used together with the temperature-dependent thermal conductivity values given in Sec. 3.3.1, correctly adjusted for the doping level.

When comparing the thermal resistances of MM and SISP waveguides, it is important to take into account the variation of the device dimensions. Due to the strong optical confinement in MM waveguides, the laser ridge can be sub-wavelength in width as opposed to SISP waveguides and in order to take this into account, the thermal resistances of the two waveguides have been normalised according to $R^*_{\mathrm{TH}} = R_{\mathrm{TH}} \times A/d$ where A is the area of the laser ridge. Simulations were performed over a range of electrical powers at various values of T_{H} and R_{TH} extracted according to Eqn. 3.1. The results are plotted in Fig. 5.4 as a function of T_{H}. The results shows that at low heat sink temperatures, the normalised thermal resistance of the MM waveguide is higher than that of the SISP waveguide and above $T_{\mathrm{H}} \sim 35$ K the normalised thermal resistance of the SISP waveguide becomes much higher than that of the MM waveguide and the difference between the two continues to increase as T_{H} increases. This behaviour is explained by the different substrates and bottom contact layers in each of the waveguides.

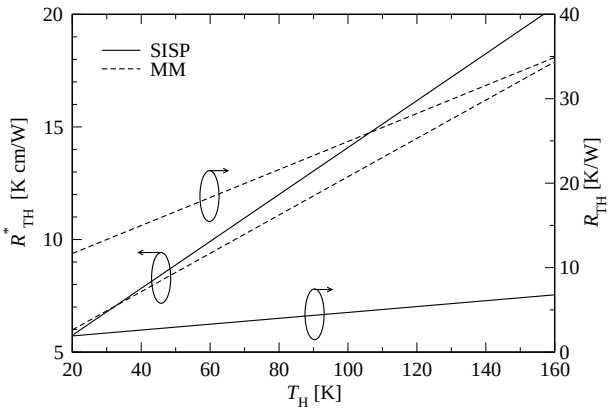

Figure 5.4: Normalised calculated thermal resistance R^*_{TH} as a function of T_{H} for both the SISP and MM optical waveguide. The unnormalised thermal resistance R_{TH} is also shown for comparison.

Below this threshold temperature, the total thermal resistance of the SI substrate and n^+ bottom contact layer in the SISP waveguide is less than that of the n^+ substrate and the Cu bottom contact layer in the MM waveguide. The n^+ substrate in the MM waveguide is the major contributor to this behaviour. Beyond the critical temperature, the reduced thermal conductivity of the n^+ bottom contact layer in the SISP waveguide compared to the Cu bottom contact layer in the MM waveguide becomes the major contributor and the normalised thermal resistance of the MM waveguide is therefore lower than that of the SISP waveguide. Since one of the major goals of research into THz QCLs is to increase the temperature performance (at least up to temperatures accessible by thermo-electric coolers), these results confirm that MM waveguides offer the best route for achieving this goal. The results also suggest that by using a substrate with a lower thermal resistivity (such as InP or even diamond), the total device thermal resistance will decrease causing a corresponding increase in temperature performance, although care must be taken to try and keep the thermally induced stresses (caused by thermal expansion coefficient mismatches) under control.

5.2.5 Investigation of the longitudinal temperature distribution

In order to investigate the temperature distribution along the length of the laser ridge in the surface-emitting THz QCL, fully three-dimensional simulations have been per-

formed using the thermal model outlined in Sec. 3.4. The longitudinal temperature distribution is extracted from the top of the active region along the centre of the laser ridge, where the measurements in Sec. 5.2.2 were taken. Fig. 5.5 shows the simulated longitudinal temperature distribution at the centre of the ridge along one half of the cavity length at $T_{\mathrm{H}} = 75$ K for $P = 2.1$ and 4 W.

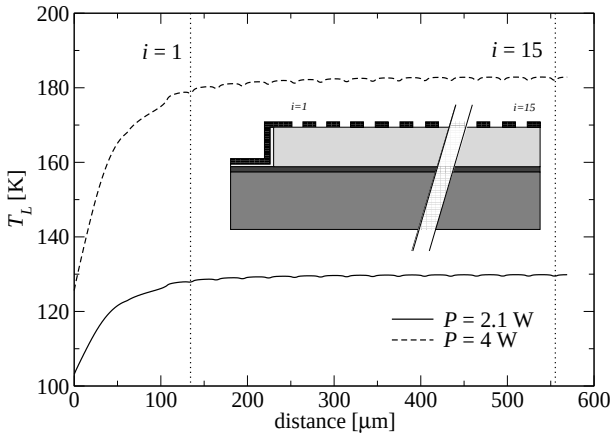

Figure 5.5: Simulated longitudinal temperature distribution at the centre of the ridge along the laser cavity of the surface-emitting THz QCL at $T_{\mathrm{H}} = 75$ K for P = 2.1 W (solid line) and 4 W (dashed line). The dotted lines show the locations of the first ($i = 1$) and central ($i = 15$) apertures in the DFB grating. Close to the ends of the laser cavity, T_{L} is reduced due to longitudinal heat escape channels formed by the insulator/metallic coating on the laser facets. The inset shows a schematic cross section along the length of the surface-emitting THz QCL (not to scale).

The results show that along the length of the laser cavity where the apertures exist, T_{L} remains approximately constant, with the temperature in the central ($i = 15$) aperture being slightly higher (~ 3 K) than the temperature in the aperture at the end of the cavity ($i = 1$). These results are in excellent agreement with experimentally measured values on the same device [9]. In the surface-emitting THz QCL, bond pads are fabricated at the ends of the cavity that also cover the electrically insulated ends of the cavity while the sidewalls are left uncoated [10]. This configuration opens up longitudinal heat escape channels which take advantage of the fact $\kappa_{\parallel} > \kappa_{\perp}$ and hence T_{L} decreases near to the ends of the laser cavity. This effect is particular to this type of device as in standard edge-emitting QCLs, the laser facets at the ends of the cavity are

uncoated and hence no longitudinal heat channels will exist and the temperature can be expected to be constant along the length of the laser cavity.

5.3 Thermal analysis of InP-based MIR QCLs

In the following section, the thermal properties of InP-based MIR QCLs are investigated and is similar in principle to Sec. 4.4 in that various thermal management techniques are compared to a benchmark ridge waveguide structure.

5.3.1 Introduction

MIR QCLs have shown a large improvement in performance since their first demonstration [22] and high-power, above room-temperature (RT) cw operation is nowadays readily achieveable in InP-based devices [23–27]. In order to understand the internal thermal dynamics of the devices with the aim of improving the temperature performance further still, in this section a standard ridge waveguide is used as a benchmark and compared to a buried heterostructure (BH) device and a ridge waveguide with a thick electroplated (EP) gold top contact layer. The devices are simulated using the steady-state thermal model and material parameters outlined in Chapter 3 over a range of operating powers and temperature-dependent thermal resistances are extracted together with the power outflows from the device active regions. These parameters allow the thermal properties of each device to be quantified in order to understand the internal thermal dynamics.

The cross-plane thermal conductivity of the active region is fixed at 2 W m^{-1} K^{-1} [18].

5.3.2 Comparison of device thermal properties

Device structures

In this work we investigate the thermal properties of three types of InP-based devices: a benchmark standard ridge waveguide (A), a BH (B) and a ridge waveguide with a thick EP gold top contact layer (C). In order to make comparisons between the devices

more meaningful they have been kept as similar as possible and are based upon the device in Ref. [27]. The active region is assumed to be 1.5 μm thick with the well material (InGaAs) assumed to account for 63% of the total thickness. The upper cladding layer is formed by 3.5 μm of InP and the InP substrate is assumed to be 100 μm-thick. The laser ridge is assumed to have been etched to the bottom of the active region. A 250 μm-thick copper heat sink and 10 μm of indium solder are also included in the simulation. In all cases, the laser ridge is taken as being 12 μm-wide and 3 mm-long. Device A is assumed to be covered in 300 nm of SiO_2 with an 8 μm window for the 300 nm-thick gold top contact layer. The ridge in device B is assumed to be surrounded on both sides by i-InP and then covered in 300 nm of SiO_2 and 300 nm of gold (also with an 8 μm window on top of the ridge). Device C is taken to be the same as A, apart from an additional 5μm of gold on top of the top contact layer.

5.3.3 Thermal resistance extraction

By running simulations for a range of electrical powers, T_{L} can be extracted as a function of P for each of the three devices. T_{L} is defined as the temperature in the centre of the QCL active region. The thermal resistance is then defined by the slope $R_{\mathrm{TH}} = dT_{\mathrm{L}}/dP$. Fig. 5.6a shows the temperature rise ($\Delta T = T_{\mathrm{L}} - T_{\mathrm{H}}$) as a function of P for all three devices at $T_{\mathrm{H}} = 300$ K.

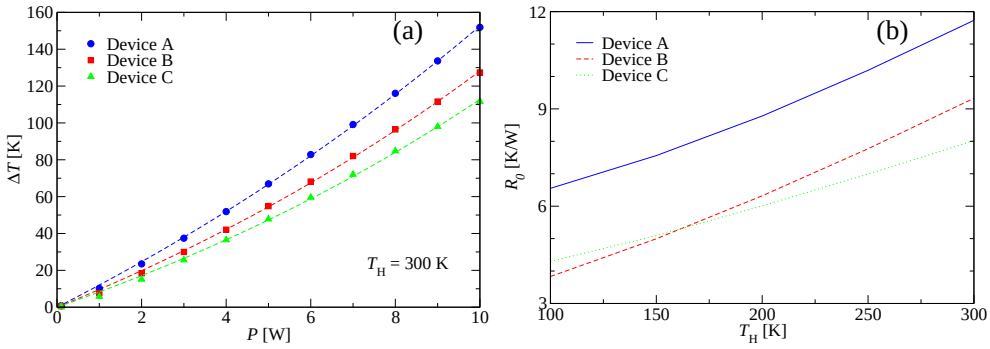

Figure 5.6: (a) Temperature rise ΔT as a function of electrical power P for: device A - standard ridge waveguide, device B - buried heterostructure and device C - standard ridge covered in thick electroplated gold. Dashed lines are fits to Eqn. 5.1. (b) Intrinsic thermal resistance R_0 as a function of T_{H} for each device.

It can be seen that for all three devices, the temperature rise has a quasi-linear dependency for low powers and begins to deviate at higher powers. The following empirical function is found to be an excellent fit to the data in the figure with correlation coefficients in excess of 0.999

$$\Delta T = T_0[\exp(P/P_0) - 1]. \tag{5.1}$$

Differentiating the above equation with respect to P gives an expression for the thermal resistance as a function of P

$$R_{\mathrm{TH}} = (T_0/P_0)\exp(P/P_0) = R_0\exp(P/P_0) \tag{5.2}$$

where R_0 is defined as the intrinsic thermal resistance of the device. Fig. 5.6b shows a plot of intrinsic thermal resistance (R_0) as a function of T_{H} for each of the three devices. It can be seen from that figure that device A has the highest intrinsic thermal resistance for all values of T_{H}. At heat sink temperatures below 165 K device B has the lowest R_0 value while above this value, device C has the lowest.

By replacing the exponential function in Eqn. 5.1 with its Taylor series and neglecting the higher-order terms it can be seen that in the low power regime, Eqn. 5.1 recovers the form of Eqn. 3.1. In this form the thermal resistance is constant irrespective of the change in the lattice temperature, whereas by combining Eqns. 5.1 and 5.2 we obtain a temperature dependent thermal resistance

$$R_{\mathrm{TH}} = R_0\left(\frac{\Delta T}{T_0} + 1\right) \tag{5.3}$$

which takes into account the temperature-dependent thermal conductivities of the materials in the device. For values of P where $\Delta T << T_0$, then the R_{TH} can be well approximated by R_0 justifying the use of Eqn. 3.1, however for higher values of P when ΔT becomes comparable to T_0, the quasi-linear relationship breaks down and a temperature-dependent R_{TH} must be used. A plot of R_{TH} as a function of P at T_{H} = 300 K for all three devices is shown in Fig. 5.7.

At this value of T_{H}, device A has the highest thermal resistance and device C the lowest, regardless of the value of P. It can be seen from the figure that as P increases, R_{TH} begins to significantly deviate from R_0, questioning the validity of Eqn. 3.1 at higher powers.

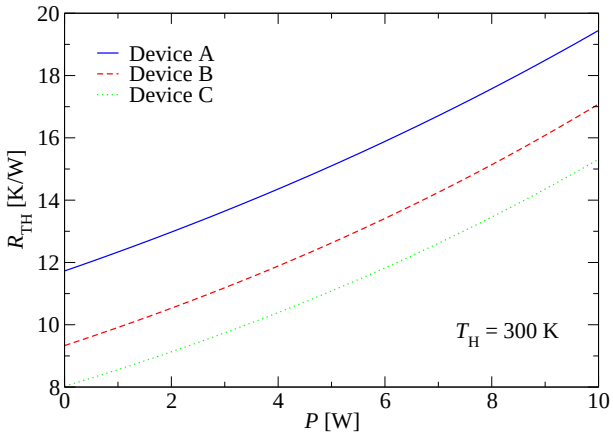

Figure 5.7: Device thermal resistances as a function of electrical power at $T_{\mathrm{H}} = 300$ K.

5.3.4 Heat-flow analysis

In order to understand the internal thermal dynamics of the devices, it is useful to know how the heat is evacuated from the active region. In this device the active region is cuboid in shape and the power which flows through each surface of the cuboid can be calculated as

$$P_f = \int -k(\mathbf{r})\nabla T(\mathbf{r})\mathrm{d}\mathbf{S} \tag{5.4}$$

where in the steady-state the total power which flows through each surface is equal to the input electrical power P dissipated in the active region volume. Here the power flow through the front and back facets of the active region has been neglected. The power outflow through each surface of the active region (out of the top through the upper cladding, laterally, and through the bottom into the substrate) for $P = 5$ W at $T_{\mathrm{H}} = 300$ K for each device is shown in Table 5.1.

Table 5.1: Total amount of heat flowing through each surface as a percentage of the total input electrical power (5 W) at T_{H} = 300 K for each device.

Flow direction	Device A	Device B	Device C
$\uparrow$	26.9 %	41.4 %	45.6 %
$\longleftrightarrow$	5.3 %	8.5 %	5.3 %
$\downarrow$	67.8 %	50.1 %	49.1 %

It can be seen from the table that with respect to device A, the majority (68%) of the heat dissipated in the active region escapes through the substrate. The extra 5 μm of gold in the case of device C compared to device A increases the amount of heat escaping through the top of the active region by $\sim$ 70%, causing a subsequent reduction in the amount escaping through the substrate to $\sim$ 50% of the total. In device B (the BH), the lateral heat channels are enhanced by $\sim$ 60% compared the device A, taking advantage of the higher in-plane thermal conductivity of the active region compared to the severely reduced cross-plane conductivity. Although increasing the lateral heat escape channels reduces the active region temperature, there is a limit on how much these channels can be enhanced which is determined by the aspect ratio of the active region. In this particular case, the active region has an aspect ratio of 8:1, meaning that vertical heat transport will always dominate over lateral heat transport. Reducing the laser ridge width will reduce the aspect ratio and increase the effect of the lateral heat channels on the active region temperature.

Fig. 5.8 shows a plot of the power outflow through each surface of device B as a function of T_{H} for $P = 5$ W.

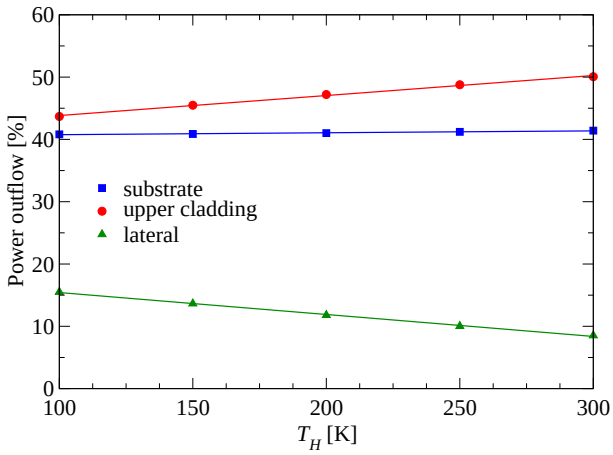

Figure 5.8: Power outflow for device B as a function of T_{H} at $P = 5$ W showing the percentage of heat escaping through each surface of the active region.

It can be seen from the figure that as T_{H} is increased, there is a suppression of the lateral heat escape channels caused by the reduction of the in-plane thermal conductivity of the active region with temperature which explains the crossover of the curves

for devices B and C in Fig. 5.6b. As the fraction of heat that escapes through the substrate remains approximately constant, the suppression of the lateral heat escape channels is compensated by an increase in the amount of heat that escapes through the upper cladding layer. This heat that evacuates the active region via the upper cladding layer then streams towards the heat sink through the i-InP surrounding the laser ridge.

The effect of varying the thickness of the gold layer of device C on the lattice temperature and the heat outflow components is shown in Fig. 5.9 for $P = 5$ W at $T_{\mathrm{H}} = 300$ K.

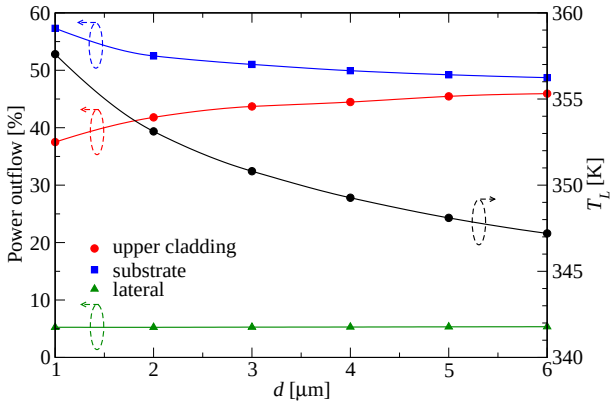

Figure 5.9: Power outflow for device C as a function of gold thickness d for $P = 5$ W at $T_{\mathrm{H}} = 300$ K showing the percentage of heat escaping through each surface of the active region. Also shown is the lattice temperature T_{L} as a function of d.

As the thickness of the gold layer increases, the lattice temperature steadily drops. By comparing the data for device B in Fig. 5.6 with the above figure, it can be seen that at $T_{\mathrm{H}} = 300$ K, the critical thickness of the gold layer is $\sim$1.5 μm. For thicknesses above this value, the rise in temperature is less in device C than for device B. It should be stressed that this critical thickness is not universal, it can be expected to change with T_{H} and the ridge aspect ratio.

Fig. 5.9 also shows that the amount of heat that escapes laterally is almost independent of the thickness of the gold layer. Instead, as the gold layer thickness increases, the fraction of heat that escapes through the upper cladding increases and offsets the decrease in the fraction of heat that escapes through the substrate. As the layer be-

comes even thicker, the fractions of heat escaping through the vertical channels begin to balance, indicating that the high thermal conductivity gold layer begins to act as a pseudo heat sink.

5.4 Conclusions

The cw thermal properties of both InP-based MIR and GaAs-based THz QCLs have been studied using the thermal model presented in Chapter 3. For the case of the THz QCL, the work was carried out in collaboration with the University of Bari who provided experimental data. By fitting the results of the thermal model to the experimental measurements, values of the temperature-dependent cross-plane thermal conductivity of the active region have been extracted. The thermal conductivity is found to be a decreasing function of temperature in good agreement with experimentally measured values for GaAs/AlAs superlattices. The temperature dependence is found to be much weaker than that of bulk semiconductors.

The thermal properties of THz MM and SISP waveguides have been compared. Above a heat sink temperature of ~ 35 K, MM waveguides are found to have the lowest thermal resistance due to the higher thermal conductivity of the metallic bonding layer. Three-dimensional calculations have been performed in order to calculate the longitudinal temperature distribution and the results are in excellent agreement with experimentally measured values.

The thermal properties of InP-based MIR QCLs with different thermal management techniques have been compared to a benchmark ridge waveguide. It has been found that at higher values of dissipated electrical power, the standard linear relation between power and temperature rise (Eqn. 3.1) which results in a constant thermal resistance breaks down. An alternative exponential function has been suggested which fits the simulation results very well and results in a temperature-dependent thermal resistance. This is expected due to the temperature-dependent material thermal conductivities.

For the particular device structure investigated here, a QCL with a thick EP gold layer is found to have a lower thermal resistance than a BH device. However, this

can be expected to change depending on the aspect ratio of the active region. For a smaller aspect ratio, the lateral heat escape channels will start to compete more with the dominant heat escape channel through the substrate. Heat flows from the active region have been calculated in each device and a larger lateral heat flow in the BH is found compared to the benchmark ridge and EP gold covered device. For larger thicknesses of gold in the EP devices, the thick gold layer acts as a pseudo-heat sink. The results have shown, especially for larger aspect ratios, that EP gold devices offer comparable, if not better, thermal performance than BH devices with the added benefit of much simpler processing.

References

[1] V. Spagnolo, M. Troccoli, G. Scamarcio, C. Gmachl, F. Capasso, A. Tredicucci, A. M. Sergent, A. L. Hutchinson, D. L. Sivco, and A. Y. Cho, "Temperature profile of GaInAs / AlInAs / InP quantum cascade laser facets measured by microprobe photoluminescence," *Appl. Phys. Lett.*, vol. 78, no. 15, p. 2095, 2001.

[2] V. Spagnolo, G. Scamarcio, D. Marano, M. Troccoli, F. Capasso, C. Gmachl, A. M. Sergent, A. L. Hutchinson, D. L. Sivco, A. Y. Cho, H. Page, C. Becker, and C. Sirtori, "Thermal characteristics of quantum cascade lasers by micro probe optical spectroscopy," *IEE Proc. Opto.*, vol. 150, no. 4, p. 298, 2003.

[3] R. Köhler, A. Tredicucci, F. Beltram, H. E. Beere, E. H. Linfield, A. G. Davies, D. A. Ritchie, R. C. Iotti, and F. Rossi, "Terahertz semiconductor heterostructure laser," *Nature*, vol. 417, no. 156, pp. 156–159, 2002.

[4] C. Walther, M. Fischer, G. Scalari, R. Terazzi, N. Hoyler, and J. Faist, "Quantum cascade lasers operating from 1.2 to 1.6 THz," *Appl. Phys. Lett.*, vol. 91, no. 131122, pp. 1–3, 2007.

[5] A. W. M. Lee, Q. Qin, S. Kumar, B. S. Williams, Q. Hu, and J. L. Reno, "Real-time terahertz imaging over a standoff distance (>25 meters)," *Appl. Phys. Lett.*, vol. 89, no. 141125, pp. 1–3, 2006.

[6] G. Scalari, C. Walther, J. Faist, H. E. Beere, and D. A. Ritchie, "Laser emission at 830 and 960 GHz from quantum cascade structures." presented at ITQW2007, Ambleside, U.K., Sept 10–14, 2007.

[7] B. S. Williams, S. Kumar, Q. Hu, and J. L. Reno, "Operation of terahertz quantum-

cascade lasers at 164 K in pulsed mode and at 117 K in continuous-wave mode," *Opt. Express*, vol. 13, no. 9, p. 3331, 2005.

[8] S. P. Khanna, M. A. Belkin, J. A. Fan, S. Harmoz, M. Lachab, F. Capasso, A. G. Davies, and E. H. Linfield, "Terahertz quantum cascade lasers operating up to 178 K with copper metal-metal waveguides." accepted for publication in Optics Express.

[9] G. Scamarcio, M. S. Vitiello, V. Spagnolo, S. Kumar, B. S. Williams, and Q. Hu, "Nanoscale heat transfer in quantum cascade lasers." accepted for publication in Physica E.

[10] S. Kumar, B. S. Williams, Q. Qin, A. W. M. Lee, Q. Hu, and J. L. Reno, "Surface-emitting distributed feedback terahertz quantum-cascade lasers in metal-metal waveguides," *Opt. Express*, vol. 15, no. 1, p. 113, 2007.

[11] M. S. Vitiello, G. Scamarcio, V. Spagnolo, A. Lops, Q. Yang, C. Manz, and J. Wagner, "Experimental investigation of the lattice and electronic temperatures in $Ga_{0.47}In_{0.53}As$ / $Al_{0.62}Ga_{0.38}As_{1-x}Sb_x$ quantum cascade lasers," *Appl. Phys. Lett.*, vol. 90, no. 121109, pp. 1–3, 2007.

[12] M. S. Vitiello, V. Spagnolo, G. Scamarcio, J. Alton, S. Barbieri, C. Worrall, H. E. Beere, D. A. Ritchie, and C. Sirtori, "Thermal properties of THz quantum cascade lasers based on different optical waveguide configurations," *Appl. Phys. Lett.*, vol. 89, no. 021111, pp. 1–3, 2006.

[13] M. S. Vitiello, G. Scamarcio, V. Spagnolo, B. S. Williams, S. Kumar, Q. Hu, and J. L. Reno, "Measurement of subband electronic temperatures and population inversion in thz quantum-cascade lasers," *Appl. Phys. Lett.*, vol. 86, no. 111115, 2005.

[14] S. Adachi, *GaAs and Related Materials: Bulk Semiconducting and Superlattice Properties*. World Scientific, 1994.

[15] M. S. Vitiello, V. Spagnolo, and G. Scamarcio, "Temperature dependence of ther-

mal conductivity and boundary resistance in THz quantum cascade lasers." accepted for publication in IEEE J. Sel. Topics Quantum Electron.

[16] W. S. Capinski, H. J. Maris, T. Ruf, M. Cardona, K. Ploog, and D. S. Katzer, "Thermal-conductivity measurements of GaAs/AlAs superlattices using a picosecond optical pump and probe technique," *Phys. Rev. B*, vol. 59, pp. 8105–8113, 1999.

[17] C. Pflügl, M. Litzenberger, W. Schrenk, D. Pogany, E. Gornik, and G. Strasser, "Inferometric study of thermal dynamics in GaAs-based quantum-cascade lasers," *Appl. Phys. Lett.*, vol. 82, no. 11, p. 1664, 2003.

[18] A. Lops, V. Spagnolo, and G. Scamarcio, "Thermal modeling of GaInAs/AlInAs quantum cascade lasers," *J. Appl. Phys.*, vol. 100, no. 043109, pp. 1–5, 2006.

[19] S. T. Huxtable, A. R. Abramson, C. Tien, A. Majumdar, C. LaBounty, X. Fan, G. Zeng, J. E. Bowers, A. Shakouri, and E. T. Croke, "Thermal conductivity of Si/SiGe and SiGe/SiGe superlattices," *Appl. Phys. Lett.*, vol. 80, no. 10, p. 1737, 2002.

[20] S. S. Howard, Z. Liu, D. Wasserman, A. J. Hoffman, T. S. Ko, and C. Gmachl, "High-performance quantum cascade lasers: optimized design through waveguide and thermal modeling," *IEEE J. Sel. Topics Quantum Electron.*, vol. 13, no. 5, pp. 1054–1064, 2007.

[21] M. S. Vitiello, G. Scamarcio, V. Spagnolo, S. S. Dhillon, and C. Sirtori, "Terahertz quantum cascade lasers with large wall-plug efficiency," *Appl. Phys. Lett.*, vol. 90, no. 191115, pp. 1–3, 2007.

[22] J. Faist, F. Capasso, D. L. Sivco, C. Sirtori, A. L. Hutchinson, and A. Y. Cho, "Quantum cascade laser," *Science*, vol. 264, p. 553, 1994.

[23] M. Beck, D. Hofstetter, T. Aellen, J. Faist, U. Oesterle, M. Ilegems, E. Gini, and H. Melchior, "Continuous wave operation of a mid-infrared semiconductor laser at room temperature," *Science*, vol. 295, p. 301, 2002.

[24] A. Evans, J. S. Yu, J. David, K. Mi, S. Slivken, and M. Razeghi, "High-temperature, high-power, continuous-wave operation of buried heterostructure quantum-cascade lasers," *Appl. Phys. Lett.*, vol. 84, no. 3, p. 314, 2004.

[25] A. Evans, J. S. Yu, S. Slivken, and M. Razeghi, "Continuous-wave operation of $\lambda \sim 4.8\mu$m quantum-cascade lasers at room temperature," *Appl. Phys. Lett.*, vol. 85, no. 12, p. 2166, 2004.

[26] J. S. Yu, S. Slivken, S. R. Darvish, A. Evans, B. Gokden, and M. Razeghi, "High-power, room-temperature, and continuous-wave operation of distributed-feedback quantum-cascade lasers at $\lambda \sim 4.8\mu$m," *Appl. Phys. Lett.*, vol. 87, no. 041104, p. 1, 2005.

[27] A. Evans, J. Nguyen, S. Slivken, J. S. Yu, S. R. Darvish, and M. Razeghi, "Quantum-cascade lasers operating in continuous-wave mode above 90 °c at $\lambda \sim 5.25\mu$m," *Appl. Phys. Lett.*, vol. 88, no. 051105, pp. 1–3, 2006.

Chapter 6

Design and simulation of InGaAs/AlAsSb quantum cascade lasers

6.1 Introduction

As mentioned briefly in Chapter 1 replacing the $In_{0.52}Al_{0.48}As$ barriers in InP-based QCL active regions with $AlAs_{0.56}Sb_{0.44}$ increases ΔE_c from 0.52 to 1.6 eV, whilst still maintaining a lattice match to an InP substrate. The increased conduction band offset and compatibility with well-established InP-based waveguides makes the InGaAs/AlAsSb material system one of the prime candidates for realising high-performance QCLs with short emission wavelengths. Devices emitting in the $\lambda \sim 3$–5μm atmospheric transmission window are of interest due to the potential applications of high-speed free-space optical communication links. Since the first observation of $\lambda \sim 4.3$ μm laser emission from these devices [1] there has been rapid progress with wavelengths covering the range $\lambda \sim 3.05$ – 4.5 μm [2–4]. Due to the large conduction band offset, these devices are intrinsically less sensitive to the temperature than traditional InP- and GaAs-based devices and have been reported operating up to 400 K in pulsed mode [2]. However, because of the large electric fields that are required to bias these structures (due to the large photon energy) and the relatively large threshold

current densities (~ 10 kA/cm^2 at 300 K [2, 3]), cw emission has been limited to 94 K using thick EP-gold covered waveguides mounted epilayer-down [5].

For InGaAs/AlAsSb with wavelengths approaching 3 μm, the upper laser level in the Γ-valley can lie above the X-valley which is around 520 meV above the bottom of the InGaAs quantum wells [4]. It was suggested that laser emission from InGaAs/AlAsSb QCLs with wavelengths smaller than $\lambda \sim 3.7$ μm may not be possible due to the difficulty in achieving population inversion because of intervalley scattering [4]. However these fears were allayed by the report of an InGaAs/AlAsSb QCL with an emission wavelength of $\lambda \sim 3.05$ μm, albeit with a maximum operating temperature of only 110 K in pulsed mode [3].

In this chapter, simulations of the electronic transport and electron heating in short-wavelength $In_{0.53}Ga_{0.47}As/Al_{0.56}As_{0.44}Sb$ QC structures are undertaken in order to shed light on the carrier dynamics in these structures.

The work presented in this chapter was published in Applied Physics Letters, 'Design and simulation of InGaAs/AlAsSb quantum cascade lasers for short wavelength emission', Volume 87, no. 141109 pp. 1–3 (2005).

6.2 Theoretical framework

The carrier dynamics of the investigated structure were calculated using the self-consistent scattering rate model which has been developed in Leeds [6–9] and is briefly outlined in this section.

6.2.1 Electronic structure

In order to calculate the electronic structure of the QCL, the one-dimensional (1D) Schrödinger equation is solved within the envelope function approximation

$$\frac{-\hbar^2}{2}\frac{d}{dz}\frac{1}{m^*(z)}\frac{d}{dz}\psi_i(z) + V(z)\psi_i(z) = E_i\psi_i(z) \tag{6.1}$$

where $m^*(z)$ is the effective mass function of the semiconductor layers in the QCL, $\psi_i(z)$ is the wavefunction of the i^{th} subband, $V(z)$ is the conduction band potential profile of the structure (which varies according to the applied field) and E_i is energy

of the i^{th} subband. Non-parabolicity is taken into account via an energy-dependent effective mass as described in Appendix C.

In order to solve the Schrödinger equation, a finite-difference method is used [7]. The equation is discretised onto a one-dimensional grid with N_z points and the derivatives are represented by central finite-differences (see Appendix D). After discretisation, the Schrödinger equation becomes

$$-\frac{\hbar^2}{2(\Delta z)^2}\left\{\frac{1}{m^*_{n+\frac{1}{2}}}\psi_{n+1}-\left[\frac{1}{m^*_{n+\frac{1}{2}}}+\frac{1}{m^*_{n-\frac{1}{2}}}\right]\psi_n+\frac{1}{m^*_{n-\frac{1}{2}}}\psi_{n-1}\right\}+V_n\psi_n=E\psi_n \quad (6.2)$$

where Δz is the mesh size and $m^*_{n+\frac{1}{2}}$ is obtained through interpolating m^*_n and m^*_{n+1}. Eqn. 6.2 reduces to a matrix eigenvalue problem with a tridiagonal Hamiltonian matrix

$$[H(E)]=-\frac{\hbar^2}{2(\Delta z)^2}\left[\frac{1}{m(E)}\right]+[V(z)] \quad (6.3)$$

where

$$\left[\frac{1}{m(E)}\right]=\begin{bmatrix} -(\frac{1}{m^*_{\frac{3}{2}}}+\frac{1}{m^*_{\frac{1}{2}}}) & \frac{1}{m^*_{\frac{3}{2}}} & 0 & 0 & \cdots \\ \frac{1}{m^*_{\frac{3}{2}}} & -(\frac{1}{m^*_{\frac{5}{2}}}+\frac{1}{m^*_{\frac{3}{2}}}) & \frac{1}{m^*_{\frac{5}{2}}} & 0 & \cdots \\ 0 & \ddots & \ddots & \ddots & \cdots \\ \vdots & 0 & 0 & \frac{1}{m^*_{n-\frac{1}{2}}} & -(\frac{1}{m^*_{n+\frac{1}{2}}}+\frac{1}{m^*_{n-\frac{1}{2}}}) \end{bmatrix}$$

and

$$[V(z)]=\begin{bmatrix} V_1 & 0 & 0 & 0 & \cdots \\ 0 & V_2 & 0 & 0 & \cdots \\ \vdots & 0 & \ddots & 0 & \cdots \\ \vdots & 0 & 0 & V_{n-1} & 0 \\ \vdots & 0 & 0 & 0 & V_n \end{bmatrix}.$$

Since the effective mass is energy-dependent (via the non-parabolicity), the eigenvalue problem is nonlinear

$$[H(E)]\psi=E\psi \quad (6.4)$$

and cannot be solved using conventional diagonalisation routines that handle linear eigenvalue problems. In order to solve the nonlinear problem, the eigenvalues of Eqn. 6.4 are found using

$$|H(E_i)]-E_i[I]|=0 \quad (6.5)$$

where E_i are the eigenvalues (i.e. energies of the electronic states) and $[I]$ is the N_z by N_z unity matrix. The eigenvectors (i.e. electron wavefunctions) are found by recasting Eqn. 6.4 in the form of a fictitious linear eigenproblem [7]

$$([H(E_i)] - E_i[I])\psi_i = \lambda\psi_i. \tag{6.6}$$

One of the eigenvalues λ of the above equation will be almost equal to zero (due to round-off errors) and the corresponding eigenvector is the actual eigenvector of Eqn. 6.4 corresponding to the eigenenergy E_i. The eigenvector is then calculated using a standard diagonalisation routine[1].

Transport within the structure is described within a tight-binding picture where each state within the structure is assigned to some specific period based upon its localisation properties. Due to the periodic nature of the structure, if $\psi(z)$ is a solution of the Schrödinger equation at energy E, then $\psi(z - L_p)$ is also a solution at energy $E - \Delta V$ where L_p is the length of the period and ΔV is the potential energy drop across one period. Therefore, in order to obtain the wavefunctions in two periods of the structure, which are required for the transport calculations, the N states that are assigned to one period of the structure are each translated in space and energy to the next period of the cascade.

6.2.2 Carrier scattering

Once the electronic structure of the cascade has been obtained, it is possible to calculate the carrier dynamics of the system. The rate (W_{if}) of an electron in an initial state $|i\rangle$ scattering into a final state $|f\rangle$ after experiencing a time-dependent perturbation is given by Fermi's golden rule as [6]

$$W_{if} = \frac{1}{\tau_{if}} = \frac{2\pi}{\hbar}\left|\langle f|\mathcal{H}|i\rangle\right|^2 \tag{6.7}$$

where τ_{if} is the lifetime of the transition and $\mathcal{H}$ is Hamiltonian of the perturbation. In this work, electron–LO phonon (e–LO) and electron–electron (e–e) scattering mechanisms are taken into account.

[1]The open source LAPACK routine DSTEBZ is used in this case

For a bulk phonon of angular frequency ω and wave vector $\mathbf{K}$ at position $\mathbf{r}$, the perturbation Hamiltonian is given by

$$\mathcal{H}_{\text{e–LO}} = e\left(\frac{\hbar\omega P}{2|\mathbf{K}|^2}\right)^{\frac{1}{2}} \frac{e^{-i\mathbf{K}\,.\,\mathbf{r}}}{V^{\frac{1}{2}}} \tag{6.8}$$

where

$$P = \frac{1}{\epsilon_\infty} - \frac{1}{\epsilon_s} \tag{6.9}$$

and V is the volume of the bulk crystal.

For the case of e–e scattering, the perturbation that appears in Fermi's golden rule is the Coulombic interaction

$$\mathcal{H}_{\text{e–e}} = \frac{e^2}{4\pi\epsilon_0\epsilon_r d} \tag{6.10}$$

where ϵ_r is the relative dielectric constant of the material and d is the separation between the electrons. The mean scattering rate of a carrier making the transition i to f is then calculated assuming a thermalised Fermi-Dirac distribution in each of the subbands.

For a more in depth discussion of the carrier scattering rates, including full derivations of expressions for both e–LO and e–e scattering rates see Refs [6] and [7]. In this work Γ–X scattering is ignored but in order to gain more understanding of the factors that limit the performance of these devices, it should be included in any future work.

6.2.3 Rate equations

Once the scattering rates for each of the transitions within the two period structure have been calculated, rate equations for each of the i subbands are formed [10]. The rate of change of population of the i^{th} subband is given by the expression

$$\frac{dn_i}{dt} = \sum_{f\neq i} n_f W_{fi} - \sum_{i\neq f} n_i W_{if} \tag{6.11}$$

where i and f are run over all states in both periods, and n_i and n_f are the initial and final subband populations. In equilibrium, $dn_i/dt = 0$ and

$$\sum_{f\neq i} n_f W_{fi} - \sum_{i\neq f} n_i W_{if} = 0. \tag{6.12}$$

The above equation, together with $\sum_i n_i = N_s$, where N_s is the total sheet doping density, gives a system of equations that can be solved for the subband populations

n_i. However, since the scattering rates themselves are also dependent upon the subband populations, the system of equations must be solved self-consistently until convergence is reached.

In addition to the above rate equations, an energy balance condition is also included in the model [11]. In equilibrium, the rate at which the electron distributions gain kinetic energy relative to the subband minimum through scattering processes balances the rate at which they lose kinetic energy to the lattice. For each particular scattering mechanism, the energy balance is given by

$$\Delta = \sum_{i,f} n_i W_{if}(E_i - E_f + \delta E) = 0 \tag{6.13}$$

where $\delta E = -E_{\mathrm{LO}}$ for phonon emission, $+E_{\mathrm{LO}}$ for phonon absorption and zero for e–e scattering. In the case of GaAs, $E_{\mathrm{LO}} = 36$ meV. The above energy balance equation is included as an additional self-consistent loop in the calculation. The scattering rates are dependent upon the electron temperature (which is assumed to be the same for each subband) and this is varied until the energy balance equation is satisfied.

6.2.4 Output parameters

After solving the rate equations self-consistently and obtaining the subband populations, it is possible to extract the output parameters of the QCL[2]. The current density is calculated by considering the flow of electrons across the plane separating the two periods (i.e. across the injection barrier of the second period)

$$J = e\left(\sum_{i=1}^{N}\sum_{j=1}^{N} n_i[W_{i,j+N} - W_{i+N,j}]\right). \tag{6.14}$$

The first term represents the contribution to the current from electrons travelling from the first to the second period while the second term represents the current flowing from the second to the first period i.e. back-scattering. By repeating the simulation at various values of applied electric field, the current–voltage characteristics of the laser are obtained.

[2]It should be noted that these output parameters take into account transitions between all states in both periods of the device and therefore give a much more detailed description of the device performance compared to the simple three-level scheme outlined in Chapter 1

The modal gain of the laser is calculated at each bias point using Eqn. 1.11. By plotting the value of modal gain at each bias point as a function of the current density at that point, the gain coefficient g can be obtained from the slope of the graph (Eqn. 1.19). The threshold current density (J_{th}) can then be estimated by observing at which current density the modal gain exceeds the total waveguide loss (which is determined using the methods outlind in Chapter 2).

6.3 Design optimisation and results

In this work, the device presented in Ref. [12] is used as a benchmark structure. The device is an InGaAs/AlAsSb QC structure (structure A) from which electroluminescence was observed at $\lambda \sim 3.1\mu$m up to 240 K. At the time of publication (2004), 3.1μm was the shortest observed intersubband emission wavelength from any material system and served to prove InGaAs/AlAsSb as a prime candidate for achieving short wavelength emission from QC structures. A schematic conduction-band diagram of structure A showing two active regions separated by an injector region at the design field of 128 kV/cm is shown in Fig. 6.1. The moduli squared of the active region wavefunctions (probability densities) are shown in red, while the injector wavefunctions are shown in blue.

The structure was simulated using the self-consistent rate equation model at the design bias of 128 kV/cm at a lattice temperature of $T_L = 77$ K with a sheet doping density of $N_s = 2.4 \times 10^{11}$ cm^{-2}. The calculated emission wavelength is $\lambda \sim 2.8\mu$m. The discrepancy with experiment is likely due to the non-parabolicity model that is used which will affect the position of the high energy upper laser level. It should be noted that very thin layers are required in the design due to the large value of E_c and even a small variation in the grown layer thickness (of the order of monolayers) can shift the subband energies by several meV thus also contributing to the discrepancy between the calculated and measured values.

The calculated subband populations in structure A at $T_L = 77$ K are shown in Fig. 6.2 It can be seen from the figure that 53% of the carriers are trapped in the ground level of the active region. This 'bottleneck' arises as a direct consequence of

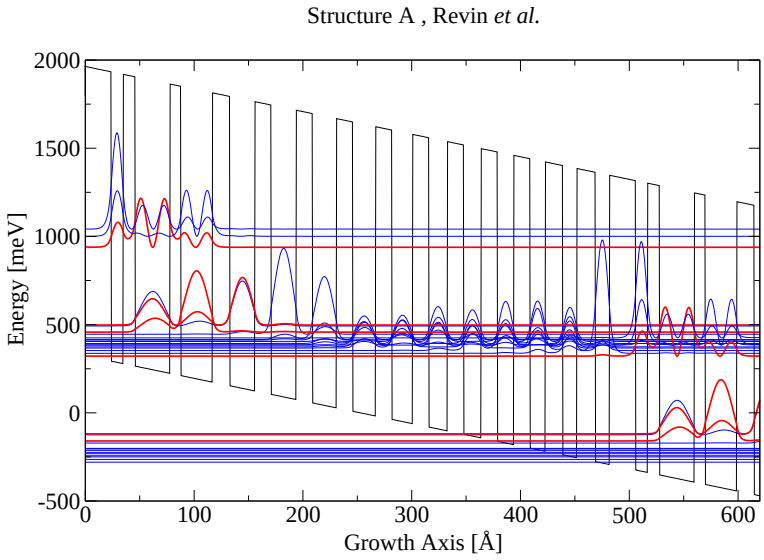

Figure 6.1: Schematic conduction-band diagram of structure A at the design field of 128 kV/cm. The layer sequence of one period of the structure (in Å) starting from the injection barrier is: **24**/11/**11**/32/**10**/29/**16**/23/**15**/23/**15**/22/**15** /21/**15**/19/**15**/17/**15**/16/**15**/15/**15**/14/**16**/13/**17**/13. The bold script denotes the $Al_{0.56}As_{0.44}Sb$ barriers, the normal script the $In_{0.53}Ga_{0.47}As$ wells. The underlined wells are doped with a sheet doping density of $N_s = 2.4 \times 10^{11}$ cm^{-2}.

the minimal overlap of the ground level with the injector states. The highest energy injector state is hybridised with the lower laser level at the design bias, causing it to be one LO phonon energy (32.7 meV in InGaAs) above the active region ground level thus preventing efficient electron extraction. The electron bottleneck limits the population inversion to only 2.6% of N_s and is the reason why lasing is not possible from the structure.

In order to improve the device performance and achieve enough gain for laser emission, the design was optimised (structure B). The main aim of the optimisation is to remove the electron bottleneck from the structure and hence increase the population inversion. This is achieved by thinning the extraction barrier (from 16 Å to 13 Å) allowing the active region ground level wavefunction to penetrate into the injector miniband, thus increasing the overlap with the injector states and therefore the scattering rate. As mentioned earlier, in structure A, the upper most injector level is one LO phonon energy above the active region ground level hindering the electron trans-

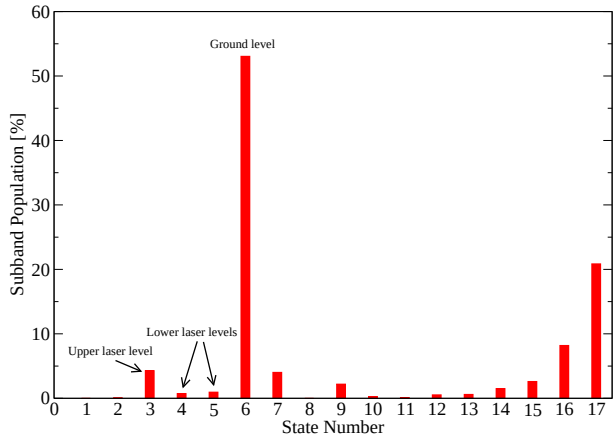

Figure 6.2: Calculated subband populations of structure A at the design field of 128 kV/cm at $T_L = 77$ K.

port. In order to improve the electron transport properties of the structure compared to structure A, the first injector well is widened (from 23 Å to 27 Å) in order to lower the upper most injector level and bring it into alignment with the active region ground level. The injection efficiency into the upper laser level from the lowest injector level is also improved by thinning the injection barrier from 24 Å to 21 Å. Transport through the injector is also improved by slightly thinning the barriers in order to increase the mixing between the miniband states. It is found that the radiative transition element z_{32} increases from 0.8 nm in structure A to 0.9 nm in structure B.

A schematic conduction-band diagram of structure B showing two active regions separated by an injector region at the design field of 130 kV/cm is shown in Fig. 6.3. The moduli squared of the active region wavefunctions (probability densities) are shown in red, while the injector wavefunctions are shown in blue.

Structure B was simulated following the same procedure as structure A keeping the same level of sheet doping density and lattice temperature. The calculated subband populations are given in Fig. 6.4. It can be seen from the figure that the electron bottleneck is no longer present and the electron transport is more efficient throughout the structure. The population inversion in structure B is 20 % of N_s compared to the 2.6 % in structure A. Fig. 6.5 shows an overview of the populations of the most important levels in each structure at 77 K.

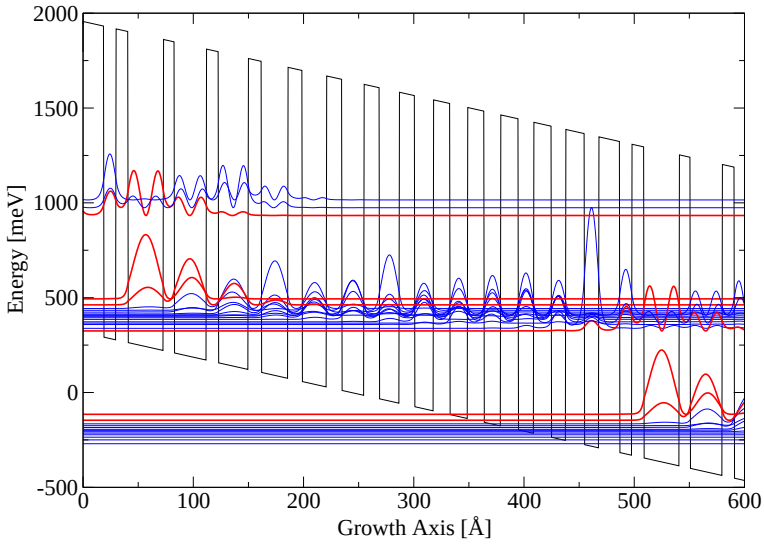

Figure 6.3: Schematic conduction-band diagram of structure B at the design field of 130 kV/cm. The layer sequence of one period of the structure (in Å) starting from the injection barrier is: **21**/11/**11**/32/**10**/29/**13**/27/**13**/24/**13**/22/**14**/20/**14**/18/**14**/17/**15**/16/**15**/15/**16**/14/**16**/13/**17**/13. The bold script denotes the $Al_{0.56}As_{0.44}Sb$ barriers, the normal script the $In_{0.53}Ga_{0.47}As$ wells. The underlined wells are doped with a sheet doping density of $N_s = 2.4 \times 10^{11}$ cm^{-2}.

By repeating the simulations over a range of bias points, electric field–current density (F–J) are obtained. The F–J curves for structures A and B at a lattice temperature of 77 K are shown in Fig. 6.6. The current density in structure A is limited to ~ 2.2 kA/cm^2 before the onset of negative differential resistance (NDR) due to the bottleneck effect. This value is in good agreement with the experimentally measured value [12]. Due to more efficient carrier transport in structure B, the maximum current density of the device increases to ~ 5.6 kA/cm^2 before the NDR occurs. This increase in the maximum current density occurs without significantly changing the applied bias, period length or sheet doping density and is down purely to the improved carrier transport.

The modal gain G_M of each device was calculated using Eqn. 1.8 with a FWHM of $2\gamma_{32} = 53$ meV [12]. The waveguide parameters were calculated using the methods presented in Chapter 2. For the InP-based waveguide described in Ref. [12], with 30 QCL periods sandwiched between 200 nm of low-doped InGaAs with a 2120 nm

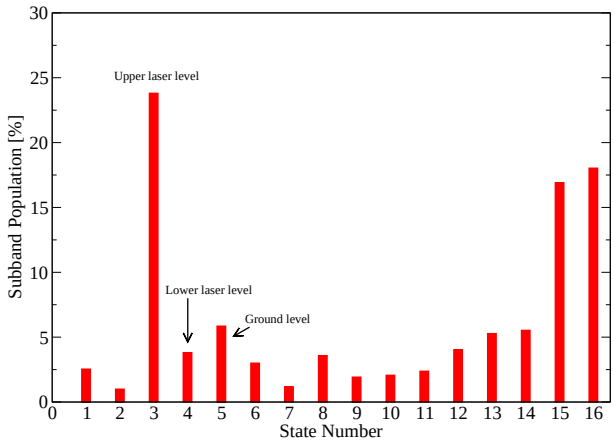

Figure 6.4: Calculated subband populations of structure B at the design field of 130 kV/cm at $T_L = 77$ K.

low-doped InAlAs upper cladding layer capped with a 150 nm highly-doped InAlAs confinement layer, the mode overlap is found to be $\Gamma = 0.41$ and the waveguide loss $\alpha_W = 3$ cm^{-1}. The mirror loss, calculated from Eqn. 2.7 is ~ 7 cm^{-1} giving total losses of ≈ 10 cm^{-1}. The modal gain as a function of current density for each structure at $T_L = 77$ K is shown below in Fig. 6.7. The total calculated waveguide losses of 10 cm^{-1} are represented by the dashed line. The threshold current density J_{th} can be obtained by extracting the value of J at which G_M exceeds the total losses. From the figure it is apparent that $J_{\text{th}} = 4$ kA/cm^2 for structure B at a lattice temperature of 77 K. Using Eqn. 1.19, the gain coefficient g can be extracted from the slope of the graph. Values of 4.4 and 5.1 cm/kA are extracted for structures A and B respectively. It can be seen that the improved carrier transport in structure B results in a $\sim 15\%$ increase in g compared to structure A. Since G_M is also a function of J as well as g, the increased current carrying capability of structure B means that the maximum value of G_M is more than double of that in structure A.

The simulation was repeated for structure B at higher values of lattice temperature and the maximum operating temperature was found to be 140 K.

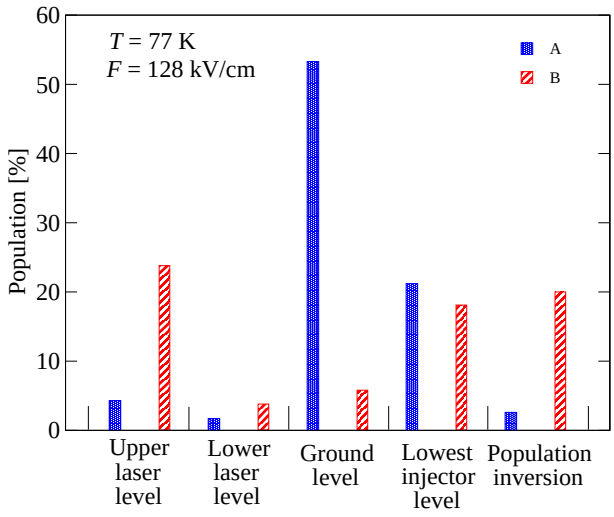

Figure 6.5: Overview of the subband populations of each structure at $T_L = 77$ K.

6.4 Increasing the maximum operating temperature

The maximum operating temperature can be increased by increasing the modal gain and this can be achieved in a number of ways. From Eqn. 1.19 we have

$$G_M(J) = g\Gamma J. \tag{6.15}$$

For a given active region, G_M can be increased through either increasing the mode overlap Γ of the optical waveguide or by increasing the current density J in the device.

6.4.1 Improved optical waveguide design

In order to increase Γ, a new plasmon-enhanced waveguide was designed, based upon the approach used by Yang *et al.* in their $\lambda \sim$4.5 μm InGaAs/AlAsSb QCL operating up to 400 K [2]. In this design, 30 periods of the active and injector regions of structure B are sandwiched between two 200 nm of $In_{0.53}Ga_{0.47}As$ confinement layers doped to 1×10^{17} cm^{-3}. The above layer sequence is surrounded on one side by an InP substrate and by three separate InP layers acting as waveguide cladding and contact layers on the other. Starting from the upper $In_{0.53}Ga_{0.47}As$ confinement layer, the InP layers doping densities and thicknesses are as follows: 5×10^{17} cm^{-3}, 20 nm; 2×10^{17} cm^{-3}, 1.3 μm; 7×10^{18} cm^{-3}, 1.3 μm. The mode confinement factor of the waveguide is calculated to be $\Gamma = 73\%$ with $\alpha_W = 0.73$ cm^{-1}. With this improved waveguide

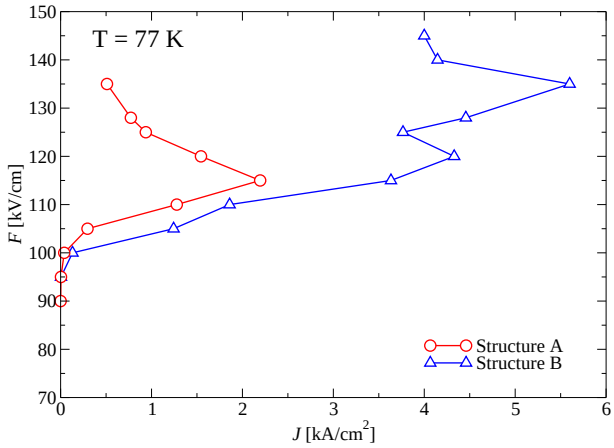

Figure 6.6: Electric field versus current density characteristics of structures A and B at a lattice temperature of 77 K.

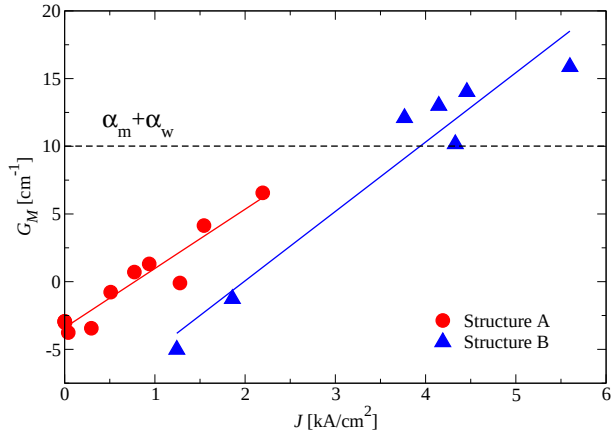

Figure 6.7: Modal gain of each structure as a function of current density. The dashed line indicates the total losses.

design, the maximum operating temperature of structure B was calculated to increase to 240 K.

6.4.2 Increasing the current density

The maximum current density through the device is proportional to the sheet doping density N_s. In order to further increase G_M and hence the maximum operating temperature, N_s was increased from 2.4×10^{11} cm^{-2} to 3.8×10^{11} cm^{-2} and laser emission was simulated up to a lattice temperature of 300 K. The relative subband populations at this higher doping are shown in Table 6.1 at 77 K and 300 K and are similar ($< 2\%$)

to the relative populations at lower doping level. However, as the gain is approximately proportional to the doping level (through the concomitant increase in current density), overall the gain increases by $\sim 50\%$.

Table 6.1: Calculated subband populations in the structures. ULL: upper laser level, LLL: lower laser level, GL: ground level, LIL: lowest injector level.

Structure	**A**	**B**	**B**	**B**	**B**
F [kV/cm]	128	130	130	130	130
T [K]	77	77	77	300	300
N_s [cm^{-2}]	2.4×10^{11}	2.4×10^{11}	3.8×10^{11}	2.4×10^{11}	3.8×10^{11}
State	**Populations [%]**				
ULL	4.3	23.8	22.1	12.2	12.4
LLL	1.7	3.8	4.1	3.8	4.2
GL	53.3	5.8	5.9	5.2	5.2
LIL	21.2	18.1	17.2	12.5	12.4

It is important to realise that the maximum operating temperature referred to here is the *lattice* temperature and, as discussed in Chapter 3, this in not necessarily equal to the heat sink temperature. The work presented in Chapter 4 investigates the relationship between the heat sink and lattice temperatures in structure B.

6.5 Threshold current density extraction

Structure B was simulated over a range of lattice temperatures at both sheet doping densities. By extracting the value of current density at which the modal gain is equal to the total waveguide loss, it is possible to extract the temperature dependence of the threshold current density which is shown in Fig. 6.8. The characteristic temperatures (T_0) are extracted by fitting the curves in Fig. 6.8 to the well known equation

$$J_{\text{th}} \approx J_{\text{th}}(0) \exp(T/T_0). \tag{6.16}$$

Values of 376 K and 348 K are extracted for the lower and higher values of N_s respectively.

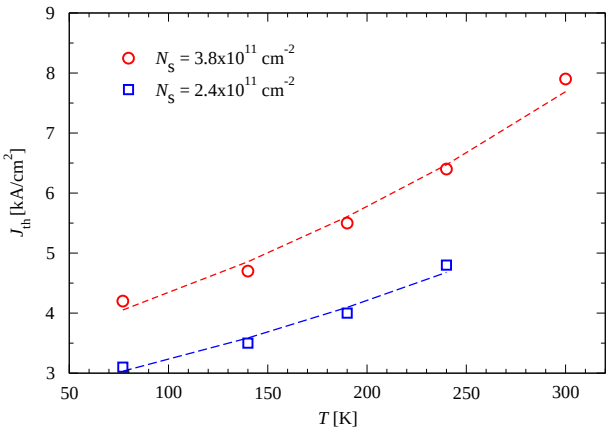

Figure 6.8: Calculated threshold current densities as a function of lattice temperature. The dashed lines show the exponential fits used to calculate the characteristic temperatures (T_0).

6.6 Investigation of electron heating

The electron temperature as a function of current density for structure B was calculated at both injector sheet doping densities and is shown in Fig. 6.9 at lattice temperatures of 77 and 300 K. At 77 K a linear dependence was obtained although at 300 K there is evidence of an exponential increase in electron temperature with current density but this can still be reasonably approximated as being quasi-linear. The electron–lattice coupling constants ($\alpha_{\text{e–l}}$) were deduced from straight line fits to the data [11]. At the lower sheet doping density ($N_s = 2.4\times10^{11}$ cm^{-2}) $\alpha_{\text{e–l}}$ was calculated to be equal to 49.1 and 58.5 K/kA cm^{-2} at 77 and 300 K respectively. These values are slightly lower than the calculated coupling constants of structure A (53.7, 61.5 K/kA cm^{-2} at 77, 300 K) indicating no degradation in electron heating. When the sheet doping density was increased to 3.8×10^{11} cm^{-2}, the coupling constants decreased to 28.9 K/kA cm^{-2} at 77 K and 38.16 K/kA cm^{-2} at 300 K.

A quasi-linear relationship was also found between the electron temperature and the electrical power density ($P_D = F \times J$), even at 300 K (see inset Fig. 6.9). The relationship is of the form $T_e = T_l + \beta_{\text{e–l}} P_D$ where T_l is the lattice temperature and the coupling constant $\beta_{\text{e–l}}$ is obtained from straight line fits to the data. At 77 K, $\beta_{\text{e–l}}$ has values of 0.36 and 0.21 K/MW cm^{-3} at the lower and higher sheet doping densities

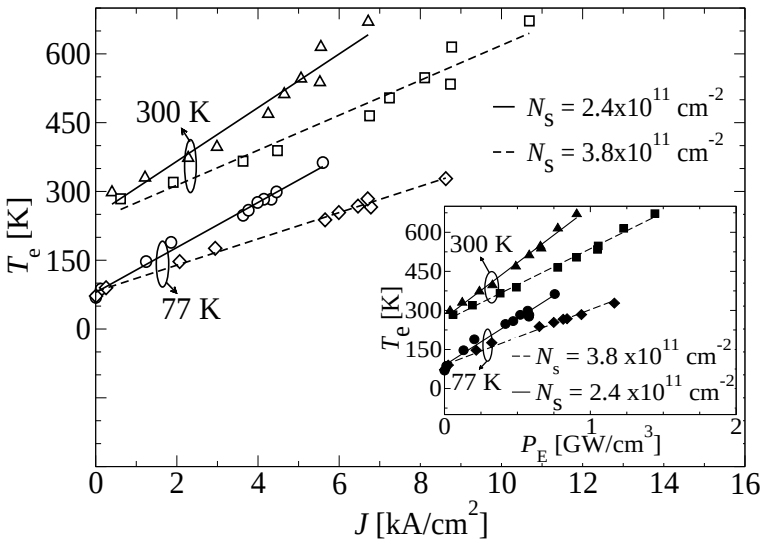

Figure 6.9: Electron temperature as a function of current density at both doping densities and at lattice temperatures of 77 and 300 K. The coupling constants $\alpha_{\text{e–l}}$ were calculated from straight line fits to the data. Inset: Electron temperature as a function of electrical power density ($F \times J$). The straight line fits were used to calculate the coupling constants $\beta_{\text{e–l}}$.

respectively. At 300 K the corresponding values of $\beta_{\text{e–l}}$ are 0.43 K/MW cm^{-3} and 0.28 K/MW cm^{-3}. The values of both $\alpha_{\text{e–l}}$ and $\beta_{\text{e–l}}$ decrease as the sheet doping density increases due to the higher number of electrons in the device. At a higher doping density, a smaller applied bias generates the same current density as a larger applied bias at a lower doping density. Hence for a given current density, the power input per electron is lower at the higher doping density and therefore less electron heating occurs. This was confirmed by calculating the ratio between the relative increase in electron temperature and the power of each individual electron $(T_e - T_l)/(P_E/N_s)$ which is equivalent to $\beta_{\text{e–l}}N_s$ and shows almost constant behaviour for both doping levels.

6.7 Conclusions

In conclusion, the simulation and design of InGaAs/AlAlSb QCLs has been reported using a fully self-consistent rate equation model. For the designed QCL a large population inversion is predicted, which in conjunction with the suggested improvements

in the waveguide design, yields sufficient gain for the possibility of laser action up to at least 300K. Considerable electron heating is anticipated, reflected by the large electron temperature–current density coupling constants of average value ~ 55 K/kA cm^{-2} which are twice as large as those found in mid-infrared GaAs-based QCLs [13]. The validity of the proposed QCL was proven by the later report of lasing at $\lambda \sim 3.05$ μm from a similar structure [3]. It has been suggested that in any future work, the role of Γ–X scattering should be investigated.

References

[1] D. G. Revin, L. R. Wilson, E. A. Zibnik, R. P. Green, and J. W. Cockburn, "InGaAs/AlAsSb quantum cascade lasers," *Appl. Phys. Lett.*, vol. 85, no. 18, p. 3992, 2004.

[2] Q. Yang, C. Manz, W. Bronner, C. Mann, L. Kirste, K. Köhler, and J. Wagner, "GaInAs/ AlAsSb quantum-cascade lasers operating up to 400 K," *Appl. Phys. Lett.*, vol. 86, no. 131107, 2005.

[3] D. G. Revin, J. W. Cockburn, M. J. Steer, R. J. Airey, M. Hopkinson, A. B. Krysa, L. R. Wilson, and S. Menzel, "InGaAs/AlAsSb/InP quantum cascade lasers operating at wavelengths close to 3 μm," *Appl. Phys. Lett.*, vol. 90, no. 021108, pp. 1–3, 2007.

[4] Q. Yang, C. Manz, W. Bronner, K. Köhler, and J. Wagner, "Room-temperature short-wavelength ($\lambda \sim 3.7$–3.9μm) GaInAs-AlAsSb quantum cascade lasers," *Appl. Phys. Lett.*, vol. 88, no. 121127, 2006.

[5] Q. Yang, C. Manz, W. Bronner, R. Moritz, C. Mann, G. Kaufel, K. Köhler, and J. Wagner, "Continuous-wave operation of GaInAs/AlGaAsSb quantum-cascade lasers," *Photon. Technol. Lett.*, vol. 17, no. 11, p. 2283, 2005.

[6] P. Harrison, *Quantum wells, wires and dots: theoretical and computational physics of semiconductor nanostructures*. John Wiley & Sons, Ltd., 2 ed., 2005.

[7] V. D. Jovanović, *Theory and design of GaAs and GaN-based quantum cascade lasers and quantum well infrared photodetectors*. PhD thesis, School of Electronic and Electrical Engineering, Univeristy of Leeds, 2005.

[8] D. Indjin, P. Harrison, R. W. Kelsall, and Z. Ikonić, "Self-consistent scattering model of carrier dynamics in GaAs-AlGaAs terahertz quantum-cascade lasers," *IEEE Photon. Technol. Lett.*, vol. 15, pp. 15–17, 2003.

[9] D. Indjin, P. Harrison, R. W. Kelsall, and Z. Ikonić, "Self-consistent scattering theory of transport and output characteristics of quantum-cascade lasers," *J. Appl. Phys.*, vol. 91, pp. 9019–9026, 2002.

[10] J. McTavish, D. Indjin, and P. Harrison, "Aspects of the internal physics of InGaAs/InAlAs quantum cascade lasers," *J. Appl. Phys.*, vol. 99, no. 114505, pp. 1–6, 2002.

[11] P. Harrison, D. Indjin, and R. W. Kelsall, "Electron temperature and mechanisms of hot carrier generation in quantum cascade lasers," *J. Appl. Phys.*, vol. 92, no. 11, p. 6921, 2002.

[12] D. G. Revin, M. J. Steer, L. R. Wilson, R. J. Airey, J. W. Cockburn, E. A. Zibnik, and R. P. Green, "InGaAs-AlAsSb quantum cascade structures emitting at 3.1 μm," *Electron. Lett.*, vol. 40, no. 14, p. 874, 2004.

[13] V. Spagnolo, G. Scamarcio, H. Page, and C. Walther, "Simultaneous measurement of the electronic and lattice temperatures in GaAs/AlGaAs quantum-cascade lasers: Influence on the optical performance," *Appl. Phys. Lett.*, vol. 84, p. 3690, 2004.

Chapter 7

Conclusions

The aim of this thesis was to investigate the optical and thermal properties of quantum cascade lasers through the development of comprehensive theoretical models. In depth knowledge of both of these important properties is paramount to understanding the factors that limit device performance and key to increasing maximum operating temperatures.

In Chapter 1, the quantum cascade (QC) principle was introduced through the adoption of a simplified three-level rate equation model. The model was then used to explain how optical gain is achieved in each of the QCL active region design schemes that have been used to date. Although the QC principle is, in theory, applicable to any material system, it has been most successful in InP-, GaAs-based and most recently in InAs/AlSb heterostructures. These material systems were discussed and current milestones outlined. Finally, the growth and potential applications of QCLs were outlined in order to give the reader a wider base from which to follow the rest of the thesis and appreciate the difficulties in experimentally realising these complex devices.

In addition to a gain medium, QCLs also require an optical waveguide in order to increase the photon density in the laser cavity and promote stimulated emission. Without sufficient photon densities, lasing would not be possible and hence the optical waveguide forms a critical component of a QCL. Chapter 2 presented an in-depth study of QCL optical waveguides. This was achieved by solving Maxwell's equations in one-dimension using a multi-layer transfer-matrix method. The one-dimensional approach is viable for ridge widths larger than the wavelength of radiation in the

waveguide; this is generally true in QCLs. The waveguide performance depends strongly on the optical properties of the materials used to engineer the waveguide layers. Generally the refractive index of the materials involved is complex and in this work, refractive indices were calculated using a Drude-Lorentz model. This model takes into account both plasma and phonon contributions to the semiconductor refractive indices. It was shown how the extinction coefficient is strongly dependent upon the electron mobility and a Caughey-Thomas-like mobility model was introduced and used to calculate the temperature dependence of the semiconductor optical properties. The developed model was then used to analyse the different types of waveguiding scheme that have been adopted for different wavelength ranges. In particular, it was shown that by including the temperature dependent material properties, better agreement with experimentally measured values of threshold current density can be achieved. Also, for the case of THz QCLs, it was shown that metal–metal optical waveguides offer the best performance as the emission wavelength increases and that the use of palladium as a plasmon-carrying layer could offer the possibility of lower waveguide losses.

In the author's own opinion, the most crucial aspect of a QCLs operation which determines its performance levels is the temperature of the active region. Due to the large amounts of electrical power dissipated in the active region, its temperature can be significantly higher than that of the heat sink. These higher temperatures cause several effects such as thermal backfilling and electron leakage which are detrimental to device performance. In addition, the various electron scattering mechanisms are strongly temperature dependent and the carrier dynamics are also affected. Since the active region temperature is not easily measured experimentally, theoretical models are required. In Chapter 3, the concept of the device thermal resistance was introduced and methods discussed of reducing the active region temperature with regards to the heat sink temperature. A thermal model was presented based upon the finite-difference solution of the heat equation. In order to fully account for the thermal behaviour of the devices, temperature dependent material parameters are used and these were presented. The model is capable of solving the heat equation in both the

time-domain (using a iterative time-marching algorithm) and in the steady-state (using a successive-over-relaxation technique).

The transient thermal model was used in Chapter 4 to investigate and compare the thermal properties of mid-infrared QCLs operating in pulsed mode. The carrier transport model presented in Chapter 6 was used to calculate the dissipated power in an InP-based InGaAs/AlAsSb QCL. For a benchmark ridge waveguide structure, it was found that the temperature range inside the active region increases for higher heat sink temperatures, meaning each period is at a different temperature and could be a limiting factor of device performance together with causing damaging thermal stress effects. It was found QCLs are much more sensitive to increases in duty-cycle through the use of longer pulses rather than increased repetition rates. Various heat management techniques were compared to the benchmark ridge in order to see which offered the best thermal performance. The cooling phase of each structure was fitted to a second-order exponential function in order to extract thermal time constants. Buried heterostructures were found to have the smallest time constants, several times smaller than the benchmark ridge waveguide.

In Chapter 5, the thermal properties of QCLs operating in continuous-wave mode were investigated. Using experimental data from the University of Bari, the temperature dependent cross-plane thermal conductivity of a GaAs-based THz QCL was deduced using the thermal model developed in this thesis. It was found to be a decreasing function of temperature as opposed to the increasing function that is found in InP-based active regions. This is in good agreement with experimentally measured values of GaAs-based superlattices. The thermal properties of metal–metal and semi-insulating surface-plasmon THz optical waveguides were compared and it was found that for higher temperature operation, metal–metal waveguides offer the best performance. A similar study to that performed in Chapter 4 was carried out on mid-infrared QCLs operating in continuous-wave mode. However in this case, a QCL with a thick electroplated top contact layer was found to have the lowest value of thermal resistance. After performing heat-flow analysis, it was found that this situation depends very strongly on the thickness of the gold layer. Below a critical thickness, the

buried heterostructure is the best option for reducing the active region temperature.

A self-consistent rate equation model of carrier transport in QCLs that has been developed in Leeds was presented in Chapter 6. It was modified and used to investigate the carrier dynamics of a short-wavelength InGaAs/AlAsSb QC structure presented in the literature that failed to lase. The results of the modelling revealed that an electron bottleneck in the ground state of the active region was trapping over half of the carriers and limiting the performance. The injector was redesigned using the modelling results as a guideline. The new design was predicted to have gain for laser emission up to 140 K. Through the re-design of the optical waveguide using the methods detailed in Chapter 2 and an increased sheet doping density, laser emission was predicted up to a lattice temperature of 300 K. The validity of the design was later verified by the report of lasing from a QCL with a very similar design.

7.1 Suggestions for further work

After reading this thesis, it should be apparent that it is far from a complete work. As is the case with scientific research, there is *always* scope for further investigation. The work presented in this thesis does not focus solely on one aspect of quantum cascade lasers in particular and instead covers a range of the most important aspects of QCLs; their thermal, optical and carrier transport properties. Therefore, it seems obvious that in order to increase the understanding of the processes that limit device performance, the aspects that are covered in this thesis should be combined in any future work.

Firstly, the optical waveguide analysis presented in Chapter 2 could be extended to two-dimensions. This would make the optical analysis compatible with the thermal model presented in Chapters 3 to 5. One of the ways to reduce the dissipated electrical power in QCLs is to reduce the laser ridge dimensions. However, reducing the ridge too much will 'squeeze' the optical mode out of the ridge, reducing the mode overlap and hence the laser gain. Therefore, a two-dimensional optical waveguide analysis would allow investigation of the impact of the lateral confinement on the mode overlap and waveguide loss, which when combined with the thermal model, would allow a balance between the optical and thermal performance of QCLs to be found.

Secondly, the combination of the presented thermal models with the carrier transport model of Chapter 6 would allow electro-thermal modelling of QCLs to take place. It is clear that the carrier dynamics in QCLs are heavily dependent upon the lattice (and electron) temperature and in turn determine the current density which flows in the device. This current density then determines the lattice temperature and creates a positive feedback loop. The self-self-consistent solution of the rate equations coupled with the heat equation would allow a more in-depth analysis of the carrier and thermal dynamics of QCLs than has been previously possible.

By using the self(-self)-consistent model to analyse THz QCLs in order to improve their performance through the optimisation of active region designs. In particular a reduction in electron leakage and thermal backfilling would reduce the current densities and in turn the lattice temperature, bringing the maximum operating temperatures of THz QCLs ever closer to those accessible by thermo-electric coolers.

Finally, the role of Γ-X scattering in short-wavelength ($\lambda \sim 3\mu$m) QCLs could be investigated. Although InGaAs/AlAsSb QCLs have been reported with the upper laser level above the X-point conduction band minima in InGaAs, their performance has not reached the same level as InGaAs/AlAsSb QCLs with emission wavelengths in the range of $\lambda \sim 4$–5μm. By including Γ-X scattering in the rate equation model, the role of the X-valleys on the carrier transport could be investigated and their influence reduced through optimised active region designs.

Appendix A

Optical gain in a quantum well system

The optical gain g per unit length of a quantum well system is given by [1]

$$G = \frac{\sigma_1}{\epsilon_0 c n} \tag{A.1}$$

where σ_1 is the real part of the optical conductivity and n is the real part of the material refractive index. For intersubband transitions in quantum wells, the real part of optical conductivity is given by [1]

$$\sigma_1(\omega) = \frac{\pi e^2}{2m^* L_p} \sum_{i,j} f_{ji} \Delta n_{ji} \delta(\omega - \omega_{ji}) \tag{A.2}$$

where m^* is the electron effective mass, L_p is the period length, Δn_{ji} is the difference in population between subbands j and i, δ is the Dirac delta function, ω_{ji} is the angular frequency of the transition and f_{ji} are the oscillator strengths of the transitions given by

$$f_{ji} = \frac{2m^*}{\hbar} \omega_{ji} |\langle j|z|i\rangle|^2. \tag{A.3}$$

Inserting (A.2) and (A.3) into (A.1) gives

$$G(\omega) = \frac{\pi e^2}{\epsilon_0 c n \hbar L_p} \sum_{i,j} \omega_{ji} \Delta n_{ji} |\langle j|z|i\rangle|^2 \delta(\omega - \omega_{ji}). \tag{A.4}$$

The above equation gives sharp δ-functions in the gain spectrum when $\omega = \omega_{ji}$ but in reality, the sharp peaks are broadened by the lifetime of the states involved and the

δ-functions can be replaced by a Lorentzian profile.

$$f(\omega;\omega_{ji},(2\gamma_{ji})) = \frac{(2\gamma_{ji})/2}{\pi}\frac{1}{(\omega-\omega_{ji})^2+([2\gamma_{ji}]/2)^2} \tag{A.5}$$

where $2\gamma_{ji}$ is the full-width at half-maximum (FWHM). The gain can then be expressed as

$$G(\omega) = \frac{\pi e^2}{\epsilon_0 cn\hbar L_p}\sum_{i,j}\omega_{ji}\Delta n_{ji}|\langle j|z|i\rangle|^2\frac{(2\gamma_{ji})/2}{\pi}\frac{1}{(\omega-\omega_{ji})^2+([2\gamma_{ji}]/2)^2}. \tag{A.6}$$

For a given $j \rightarrow i$ transition at $\omega = \omega_{ji}$, A.6 simplifies to

$$G_{ji} = \left[\frac{2e^2}{\epsilon_0 cn\hbar}\frac{\omega_{ji}|\langle j|z|i\rangle|^2}{2\gamma_{ji}L_p}\right]\Delta n_{ji} \tag{A.7}$$

which, after converting to wavelength gives

$$G_{ji} = \left[\frac{4\pi e^2}{\epsilon_0 n}\frac{|\langle j|z|i\rangle|^2}{2\gamma_{ji}L_p\lambda}\right]\Delta n_{ji} \tag{A.8}$$

References

[1] J. H. Davies, *The physics of low-dimensional semiconductors: an introduction*. Cambridge, 1998.

Appendix B

Derivation of the dielectric waveguide transfer matrix

For a transverse electric (TE) mode propagating in the $+z$ direction in the i^{th} layer ($x_{i-1} \leq x \leq x_i$) which has a constant refractive index n_i and permeability $\mu_r = 1$, the electric field is given by the product of a plane wave propagating in the $+z$ direction with a propagation constant γ ($\gamma = \beta + j\alpha$, where β and α are the phase and attenuation propagation constants respectively), modulated by an amplitude $E_{yi}(x)$.

$$\vec{\varepsilon_i} = \hat{y} E_{yi} \exp[j(\omega t - \gamma z)] \tag{B.1}$$

$E_{yi}(x)$ must satisfy the reduced wave equation

$$\frac{\partial^2 E_{yi}}{\partial x^2} - \kappa_i^2 E_{yi} = 0 \tag{B.2}$$

where $\kappa_i = \sqrt{\gamma^2 - k_0^2 n_i^2}$ are the complex transverse wavevectors, $k_0 = 2\pi/\lambda_0$ and λ_0 is the free-space wavelength. The general solution of Eqn. B.2 is given in Eqn. B.3 and can be thought of as a superposition of forward and backward propagating electric fields.

$$E_{yi}(x) = A_i \exp[-\kappa_i(x - x_{i-1})] + B_i \exp[\kappa_i(x - x_{i-1})] \tag{B.3}$$

A_i and B_i are complex coefficients relating to the forward and backward propagating fields respectively and x_{i-1} is the boundary between the i^{th} and $(i-1)^{th}$ layer. By matching the tangential field components of the displacement fields at each layer interface, the transfer matrices of each layer can be derived.

From Maxwell's equations

$$\frac{\partial}{\partial x}E_{yi}(x) = -\jmath\omega\mu_0 H_{zi}(x). \tag{B.4}$$

In layer i, the electric and magnetic fields are given by Eqns. B.5 and B.6 respectively.

$$E_{yi}(x) = A_i \exp[-\kappa_i(x - x_{i-1})] + B_i \exp[\kappa_i(x - x_{i-1})] \tag{B.5}$$

$$\mu_0\omega H_{zi}(x) = -\kappa_i \left(A_i \exp[-\kappa_i(x - x_{i-1})] + B_i \exp[\kappa_i(x - x_{i-1})]\right) \tag{B.6}$$

In layer $i + 1$, the electric field is given by

$$E_{yi+1}(x) = A_{i+1} \exp[-\kappa_{i+1}(x - x_i)] + B_{i+1} \exp[\kappa_{i+1}(x - x_i)] \tag{B.7}$$

and the magnetic field by

$$\mu_0\omega H_{zi+1}(x) = -\kappa_{i+1} \left(A_{i+1} \exp[-\kappa_{i+1}(x - x_i)] + B_{i+1} \exp[\kappa_{i+1}(x - x_i)]\right) \tag{B.8}$$

The displacement field in each layer is given by $\bar{D}_i = \epsilon_i \bar{E}_i$ (where ϵ_i is the dielectric constant of the i^{th} layer) and hence Eqns. B.5 and B.6 must be multiplied by ϵ_i and Eqns. B.7 and B.8 multiplied by ϵ_{i+1}. At $x = x_i$ (i.e. the boundary between the i^{th} and $(i + 1)^{th}$ layer) the tangential components of the displacement fields are continuous and by substituting $x = x_i$ in Eqns. B.5 and B.7, the following relation from the electric fields in each layer is given

$$\epsilon_i \left(A_i \exp[-\kappa_i d_i] + B_i \exp[\kappa_i d_i]\right) = \epsilon_{i+1} \left(A_{i+1} + B_{i+1}\right) \tag{B.9}$$

where d_i is the layer width given by $x_i - x_{i-1}$. By substituting $x = x_i$ in Eqns. B.6 and B.8, the following relation from the magnetic fields in each layer is given

$$-\kappa_i\epsilon_i \left(A_i \exp[-\kappa_i d_i] - B_i \exp[\kappa_i d_i]\right) = -\kappa_{i+1}\epsilon_{i+1}(A_{i+1} - B_{i+1}) \tag{B.10}$$

Eqn. B.9 can be re-arranged to give

$$A_{i+1} = \left[\frac{\epsilon_i}{\epsilon_{i+1}} \left(A_i \exp[-\kappa_i d_i] + B_i \exp[\kappa_i d_i]\right)\right] - B_{i+1} \tag{B.11}$$

Re-arranging Eqn. B.10 gives

$$B_{i+1} = A_{i+1} - \left[\frac{\epsilon_i}{\epsilon_{i+1}} \left(A_i \frac{\kappa_i}{\kappa_{i+1}} \exp[-\kappa_i d_i] - B_i \frac{\kappa_i}{\kappa_{i+1}} \exp[\kappa_i d_i]\right)\right] \tag{B.12}$$

Substituting Eqn. B.12 into Eqn. B.11 and collecting variables gives

$$A_{i+1} = \frac{\epsilon_i}{2\epsilon_{i+1}} \left[A_i \left(1 + \frac{\kappa_i}{\kappa_{i+1}} \exp[-\kappa_i d_i] \right) + B_i \left(1 - \frac{\kappa_i}{\kappa_{i+1}} \exp[\kappa_i d_i] \right) \right] \tag{B.13}$$

Substituting Eqn. B.11 into Eqn. B.12 and collecting variables together gives

$$B_{i+1} = \frac{\epsilon_i}{2\epsilon_{i+1}} \left[A_i \left(1 - \frac{\kappa_i}{\kappa_{i+1}} \exp[-\kappa_i d_i] \right) + B_i \left(1 + \frac{\kappa_i}{\kappa_{i+1}} \exp[\kappa_i d_i] \right) \right] \tag{B.14}$$

Eqns. B.13 and B.14 can be put into matrix form

$$\begin{pmatrix} A_{i+1} \\ B_{i+1} \end{pmatrix} = \mathcal{Q}_i \begin{pmatrix} A_i \\ B_i \end{pmatrix}$$

where the transfer matrix of the i^{th} layer, $\mathcal{Q}_i$, is given by

$$\mathcal{Q}_i = \frac{\epsilon_i}{2\epsilon_{i+1}} \begin{pmatrix} \left[1 + f_i \frac{\kappa_i}{\kappa_{i+1}} \right] \exp[-\kappa_i d_i] & \left[1 - f_i \frac{\kappa_i}{\kappa_{i+1}} \right] \exp[\kappa_i d_i] \\ \left[1 - f_i \frac{\kappa_i}{\kappa_{i+1}} \right] \exp[-\kappa_i d_i] & \left[1 + f_i \frac{\kappa_i}{\kappa_{i+1}} \right] \exp[\kappa_i d_i] \end{pmatrix}$$

For a TE mode, $f_i = 1$ and for a Transverse Magnetic (TM) $f_i = \epsilon_{i+1}/\epsilon_i$ [1].

References

[1] E. Anemogiannis, E. N. Glytsis, and T. K. Gaylord, "Determination of guided and leaky modes in lossless and lossy planar multilayer optical waveguides: Reflection pole method and wavevector density method," *IEEE J. Light. Technol.*, vol. 17, pp. 929–941, May 1999.

Appendix C

Material parameters

C.1 Abele's interpolation scheme

Abele's interpolation scheme enables the properties of a ternary semiconductor to be obtained from the properties of the corresponding binary semicnductors i.e.

$$A_xB_{1-x}C = xAC + (1-x)BC + x(1-x)C_{AB} \tag{C.1}$$

where C_{AB} is known as the bowing parameter.

C.2 Electron effective mass

The electron mass in a semiconductor is given by

$$m = m^* m_0 \tag{C.2}$$

where m^* is the electron effective mass and m_0 is the rest mass of an electron (9.10956×10^{-31} kg).

Table C.1 lists the effective mass of an electron in various semiconductors

C.2.1 Band nonparabolicity

Band nonparabolicity in the semiconductor quantum wells is taken into account following the method of Nelson *et al.* [1] which is based on a two-band (Kane) model. In this model the dispersion relation in a quantum well is given by

$$E = \frac{\hbar^2 k_w^2}{2m_i^*(E)} \qquad (i = w, b) \tag{C.3}$$

Material	m^*
GaAs	0.067
InAs	0.023
InP	0.079
$Al_xGa_{1-x}As$ ($x < 0.45$)	0.067+0.083x
$In_{0.53}Ga_{0.47}As$	0.042
$In_{0.52}Al_{0.48}As$	0.075
$AlAs_{0.52}Sb_{0.48}$	0.125

Table C.1: Electron effective masses

where w denotes well and b barrier. The energy-dependent effective masses are given by

$$m_i^*(E) = m_i^*[1 - (V - E)/E_i] \qquad (i = w, b) \tag{C.4}$$

where E_w and E_b are the energy gaps between the conduction and light-hole valence bands in the well and barrier material. The energy gaps are calculated by

$$E_i = \frac{\hbar^2}{2m_i^*\gamma_i} \qquad (i = w, b) \tag{C.5}$$

where γ_i is the nonparabolicity parameter. The nonparabolicity parameters in the well and barrier materials are related through

$$\frac{\gamma_w}{\gamma_b} = \left(\frac{m_b^*}{m_w^*}\right)^2 \tag{C.6}$$

which means that only one value of γ_i is required and the other can be inferred through the above relation providing the electron effective masses are known in the well and barrier materials.

Table C.2 lists the nonparabolicty parameters of the most common QCL well materials.

Material	$\gamma_w\ (m^2)$
GaAs	4.9×10^{-19} [1]
$In_{0.53}Ga_{0.47}As$	1.13×10^{-18} [2]

Table C.2: Nonparabolicity parameters

References

[1] D. F. Nelson, R. C. Miller, and D. A. Kleinman, "Band nonparabolicity effects in semiconductor quantum wells," *Phys. Rev. B*, vol. 35, no. 14, pp. 7770–7773, 1987.

[2] C. Sirtori, F. Capasso, J. Faist, and S. Scandolo, "Nonparabolicity and a sum rule associated with bound-to-bound and bound-to-continuum intersubband transitions in quantum wells," *Phys. Rev. B*, vol. 50, no. 12, pp. 8663–8674, 1994.

Appendix D

Introduction to finite-difference methods

There are three common types of finite difference approximations to differential equations, the *forward, backward* and *central difference* approximations. From Taylor's theorem we have

$$f(x+h) = f(x) + \frac{f'(x)h}{1!} + \frac{f''(x)h^2}{2!} + \frac{f'''(x)h^3}{3!} + ... + \frac{f^n(x)h^n}{n!} \tag{D.1}$$

and

$$f(x-h) = f(x) - \frac{f'(x)h}{1!} + \frac{f''(x)h^2}{2!} - \frac{f'''(x)h^3}{3!} + ...\frac{f^n(x)h^n}{n!} \tag{D.2}$$

Ignoring the higher order terms in Equation D.1 we obtain the forward difference approximation to $f'(x)$

$$f'(x) = \frac{f(x+h) - f(x)}{h} + \mathcal{O}(h) \tag{D.3}$$

Following the same approach with Equation D.2 we obtain the backward difference approximation to $f'(x)$

$$f'(x) = \frac{f(x) - f(x-h)}{h} + \mathcal{O}(h) \tag{D.4}$$

If we subtract Equation D.2 from D.1 we obtain the central difference approximation to $f'(x)$

$$f'(x) = \frac{f(x+h) - f(x-h)}{2h} + \mathcal{O}(h^2) \tag{D.5}$$

To obtain the central difference approximation to $f''(x)$, we add Equation's D.2 and D.1

$$f''(x) = \frac{f(x+h) - 2f(x) + f(x-h)}{h^2} + \mathcal{O}(h^2) \tag{D.6}$$

Both the forward and backward approximations introduce truncation errors of the order h to the finite-difference approximation of $f'(x)$, while the central difference approximation is more accurate and introduces truncation errors of the order of h^2.

Index